Stony Brook University

Modeling of Multiphase Flow with Solidification and Chemical Reaction in Materials Processing

A Dissertation Presented

by

Jiuan Wei

to

The Graduate School

in Partial fulfillment of the

Requirements

for the Degree of

Doctor of Philosophy

in

Mechanical Engineering

(Thermal Sciences and Fluid Mechanics)

Stony Brook University

May 2009

Stony Brook University

The Graduate School

Jiuan Wei

We, the dissertation committee for the above candidate for the

Doctor of Philosophy degree,

hereby recommend acceptance of this dissertation.

Lili Zheng, Dissertation Advisor
Professor, Department of Mechanical Engineering

Chad Korach, Chair
Professor, Department of Mechanical Engineering

Imin Kao, Committee Member
Professor, Department of Mechanical Engineering

Xiaolin Li, Outside Member
Professor, Department of Applied Mathematics and Statistics

This dissertation is accepted by the Graduate School

Lawrence Martin
Dean of the Graduate School

Abstract of the Dissertation

Modeling of Multiphase Flow with Solidification and Chemical Reaction in Materials Processing

by

Jiuan Wei

Doctor of Philosophy

in

Mechanical Engineering

(Thermal Sciences and Fluid Mechanics)

Stony Brook University

2009

Multiphase flow usually involves multi-scale, multi phases and multi component as well as multi physical processes. Multiphase flow occurs in many physical processes and industrial system. Understanding of multiphase flow and related heat transfer and chemical reactions are the keys to increase the productivity and efficiency in industrial processes. The objective of this thesis is to utilize the computational approaches to investigate the multiphase flow and its application in the materials processes, especially in the following two areas: directional solidification, and pyrolysis and synthesis.

Bridgman technique and directional solidification system (DSS) are the two major types to produce single crystal and multi-crystalline silicon by direction solidification. Bridgman crystal growth has been widely used to grow different kinds of crystals due to its simplicity. However, as the crystal size increases, it is difficult to control the flow pattern and the solutal transport in the melt. To reduce the melt convection, we can reduce either melt diameter or melt height. In the traditional Bridgman growth, a

large/high melt zone exists, which will cause a strong convection in the melt. The situation becomes worse to grow long and large diameter crystals. In this thesis, numerical simulations will be performed for crystal growth of several III-V and II-VI compounds. The effects of Prandtl and Grashof numbers on the axial temperature profile, the solidification interface shape, and melt flow are investigated. For the material with high Prandtl and Grashof numbers, temperature field and growth interface will be significantly influenced by melt flow, resulting in the complicated temperature distribution and curved interface shape, so it will encounter tremendous difficulty using a traditional Bridgman growth system. A new design is proposed to reduce the melt convection. The geometric configuration of top cold and bottom hot in the melt will dramatically reduce the melt convection. The new design has been employed to simulate the melt flow and heat transfer in crystal growth with large Prandtl and Grashof numbers and the design parameters have been adjusted.

Over 90% of commercial solar cells are made from silicon and directional solidification system is the one of the most important method to produce multi-crystalline silicon ingots due to its tolerance to feedstock impurities and lower manufacturing cost. A numerical model is developed to simulate the silicon ingot directional solidification process. Temperature distribution and solidification interface location are presented. Heat transfer and solidification analysis are performed to determine the energy efficiency of the silicon production furnace. Possible improvements are identified. The silicon growth process is controlled by adjusting heating power and moving the side insulation layer upward. It is possible to produce high quality crystal with a good combination of heating and cooling.

SiC based ceramic materials fabricated by polymer pyrolysis and synthesis becomes a promising candidate for nuclear applications. To obtain high uniformity of microstructure/concentration fuel without crack at high operating temperature, it is important to understand transport phenomena in material processing at different scale levels. In our prior work, a system level model based on reactive porous media theory was developed to account for the pyrolysis process in uranium-ceramic nuclear fabrication In this

thesis, a particle level mesoscopic model based on the Smoothed Particle Hydrodynamics (SPH) is developed for modeling the synthesis of filler U_3O_8 particles and SiC matrix. The system-level model provides the thermal boundary conditions needed in the particle level simulation. The evolution of particle concentration and structure as well as composition of composite produced will be investigated. Since the process temperature and heat flux play the important roles in material quality and uniformity, the effects of heating rate at different directions, filler particle size and distribution on uniformity and microstructure of the final product are investigated. Uncertainty issue is also discussed.

For the multiphase flow with directional solidification, a system level based on FVM is established. In this model, melt convection, temperature distribution, phase change and solidification interface can be investigated. For the multiphase flow with chemical reaction, a particle level model based on SPH method is developed to describe the pyrolysis and synthesis process of uranium-ceramic nuclear fuel. Due to its mesh-free nature, SPH can easily handle the problems with multi phases and components, large deformation, chemical reactions and even solidifications.

A multi-scale meso-macroscopic approach, which combine a mesoscopic model based on SPH method and macroscopic model based on FVM, FEM and FDM, can be applied to even more complicated system. In the mesoscopic model by SPH method, some fundamental mesoscopic phenomena, such as the microstructure evolution, interface morphology represented by high resolution, particle entrapment in solidification can be studied. In the macroscopic model, the heat transfer, fluid flow, species transport can be modeled, and the simulation results provided the velocity, temperature and species boundary condition necessary for the mesoscopic model. This part falls into the region of future work.

TABLE OF CONTENTS

LIST OF FIGURES

LIST OF TABLES

NOMENCLATURE

Bi	Biot number
C_D	Drag coefficient
C_l	Concentration of impurity in the liquid (mol/m^3)
C_s	Concentration of impurity in the solid (mol/m^3)
C_p	Specific heat at constant pressure (J/Kg·K)
D	Diffusion coefficient
D_i	Drag force on each particle (N)
d_p	Equivalent average particle diameter (m)
d	Particle diameter (m)
E_a	Activation energy (J/mol)
f	Volume fraction
f_g	External force acting on gas phase (N)
f_s	External force acting on solid phase (N)
ΔG	Free energy (J/mol)
Gr	Grashof number
ΔG_f	Thermodynamic driving force for solidification (J/mol)
G_l	Gibbs energy of liquid (J/mol)
G_s	Gibbs energy of solid (J/mol)
ΔH	Enthalpy (J/mol)
K	Permeability (m^2)
k	Thermal conductivity (W/m·K)
m	Mass (kg)
$\dot{M}$	Mass change rate (kg/s)
N	Total particle number
n	Ratio of diameter of large particles and small particles
P	Pressure (Pa)
Pr	Prandtl number

q'' Heat flux (W/m^2)

$\dot{R}$ Reaction rate

R Universal gas constant, 8.314 (J/mol·K)

Re Reynolds number

r Radial coordinate

ΔS Entropy (J/mol K)

Ste Stefan number

T Temperature (K)

T_{MP} Melting point (K)

t Time (s)

u Velocity vector

u_r Radial velocity (m/s)

V Volume (m^3)

W Smoothing function

Y Species mass fraction

Z Pre-exponential

z Axial coordinate

Greek symbols

σ Stefan-Boltzmann constant ($W/m^2 \cdot K^4$)

ε Porosity

τ Viscous stress tensor （Pa)

β Thermal expansion coefficient (/K)

Coefficient for the inter-phase momentum exchange term

μ Viscosity (kg/m·s)

ν Kinematic viscosity, μ/ρ (m^2/s)

ρ Density (kg/m^3)

Subscripts

∞	Surrounding
df	Driving force
eff	Effective
g	Gas
i	Particle number
j	Particle number
k	Particle number
l	Liquid
r	Radial direction
s	Solid

Chapter One

Introduction

1.1 Literature Review

1.1.1 Brief introduction of Multiphase Flow

Multiphase flow usually involves multi-scale (different time and length scale) and multi physical processes. For example, in the processes of metals reduction and refining, turbulent-component fluid dynamics with free surface is involved and chemical reactions among all the phases are present [1]. Moreover, there are different time and length scales involved in the processes: (i) chemical reactions can be regarded as instantaneous; (ii) the particle/droplet/bubble flow dynamics are of the order of sub-seconds; (iii) timescale for bath stirring is a few minutes; (iv) timescale for reduction/refining is several hours.

Multiphase flow occurs in many physical processes and industrial system involving more than one phase. Understanding of multiphase flow and related heat transfer are the keys to increase the productivity and efficiency in industrial processes, such as crystal growth, foundry casting, electronics cooling, fuel cells, petroleum refining, slurry and pneumatic transport, aircraft wing icing, deep-sea mining, aseptic food processing, foam production, aerosols, particulate erosion, etc. Since multiphase flow involves multi-components and multi-phases, which make multiphase flow difficult to study in the experiments, therefore computational modeling has been widely used to study the multiphase flow in recent decades.

Two general topologies of multiphase flow can be identified, namely disperse flow and separated flow [2]. In disperse flow, there is only one continuous phase and all other phases are in forms of particles, droplets and bubbles with much smaller sizes compared to the macroscopic length scale of the flow. On the other hand a separated flow contains more than one continuous phase separated by interface.

1.1.2 Modeling of Multiphase Flow with Solidification

Modeling of transport phenomena during solidification has received remarkable attention in the past decades. Numerical methods have been developed to handle the phase change and interface.

To predict the composition and structure in alloy solidification, a general approach namely micro-macroscopic method is applied for modeling the microstructure evolution during dendritic solidification [3]. It aims to incorporate descriptions of fundamental microscopic phenomena, such as nucleation, undercooling and grain growth into macroscopic heat transfer and fluid flow calculations. According to Tan [4], there are mainly two types of multiscale techniques for solidification: (i) performing analytic studies in the microscale model and providing the necessary information to the macroscale computations, (ii) resolving microscale details using adaptive mesh refinement or adaptive moving grids.

To perform analytic studies in the microscale, Wang and Beckermann [3] proposed a multiphase solute diffuse model for dendritic alloy solidification, accounting for the different microscopic length scale in a dendritic structure, such as the primary and secondary dendrite arm spacing, and the radius of a dendrite tip. However, in the previous work by Ni and Beckermann [5], a single-scale two-phase model is used, which cannot discriminate the properties of a phase associated with different microscopic length scales. Thus this single scale model does not provide sufficient resolution to capture dynamic behavior on several microscopic length scales. Later on, Wang and Beckermann extend their multiphase mutliscale model to take in account melt convection and solid transport [6].

Provatas et al [7] presented an efficient adaptive-grid algorithm to study microstructure formation in solidification by solving a set of governing equations based on phase-field method. This algorithm is robust by applying dynamic data structure and pointer variables to represent the evolving grids. A new numerical scheme, combining the adaptive mesh method and the semi-implicit Fourier spectral algorithm, is developed to solve phase-field equations for both two and three-dimensional Allen-Cahn (TDGL) problem [8].

The common approach to simulate multiphase flow with solidification is to establish one single set of equations for all the phases involved. The formulation accounts for the different materials properties in each phase and singular source terms are added at the phase boundaries to satisfy the conservation laws. A number of methods are used to capture the phase boundary, including front tracking, level set, and phase filed methods.

The advantages of front tracking method lies in that it can easily handle discontinuity in material properties between solid and liquid phases, topology changes and anisotropy of interfacial energy. The interface temperature is given by Gibbs-Thomson relation, and energy balance is satisfied in the interface by Stefan condition. Juric and Tryggvason [9] presented a front-tracking method to simulate transient two-dimensional dendritic solidification of pure substances. It is based on a finite difference approximation of the energy equation and the liquid-solid interface is explicitly tracked. Then the effect of melt flow on the dendrite growth by two and three-dimensional was investigated by Al-Rawahi and Tryggvason [10, 11]. The simulation results show that on the upstream side, melt flow can increase heat release, growth rate and more side branch formation, however, it also results in a reduction of the growth rate of the downstream arm. Zhao and Heinrich [12] developed a two-dimensional finite element method for interface tracking based on a fixed mesh, and it can achieve second-order convergence in the approximation of interface and the first-order for the interface velocity. However the complexity for handling interfaces in such conditions involving advancing/receding, merging/splitting hinders the application of front-tracking method to single solid phase system.

Phase field methods have been widely applied in modeling solidification processes. One of the distinguishing characteristics of the phase field method is that the interface between phases is diffuse, not a sharp one in other conventional methods. Therefore, it is not necessary to compute the interfacial geometric quantities such as interface curvature and outward normal vector. The phase field method reduces to the sharp interface in the limit where the interface thickness goes to zero. One drawback of phase field method is that a large number of parameters are involved in the solution resulting in the difficulty in application to real materials. Wheeler et al [13] presented a phase field model to describe isothermal phase transition in binary alloys and the classical sharp interface is recovered

when the interface thickness must be smaller than the capillary length for the solution to converge to the sharp interface limit. Lan et al [14] developed an adaptive finite volume method to solve the incompressible heat flow problems in solidification. This method is based on the adaptive mesh refinement and coarsening using dynamic data structure.

The level set method is an alternative numerical technique for tracking interfaces and shapes. In the level set method, interfacial geometric quantities such as interface curvature and outward normal vector can be easily calculated using the level set variable Φ, which is the signed distance from the interface. The advantage of this method is that one can perform numerical computations involving curves and surfaces on a fixed Cartesian grid without having to parameterize these objects. Moreover, the level set method makes it very easy to follow shapes that change topology, for example when a shape splits in two, develops holes, or the reverse of these operations. All these make the level set method a great tool for modeling solidification process. Kim et al [15] presented time-dependent solutions of dendritic solidification in two-dimensional by using a level set method. Results are compared with those obtained by phase field method and achieved good agreement with each other. Zheng and Zhang [16] developed a three dimensional adaptive level set method for deformable free surface problems with solidification. In their scheme, a level set method is used to capture the free surface deformation. Tan and Zabaras [4, 17, 18] developed a level set method, which combines features of front tracking method and fixed domain method, to model microstructure evolution in the solidification of multi-component alloys. This methodology circumvents the difficulty of parameter identification needed in other diffused interface models and can serve as an alternative approach to phase field method.

Besides the aforementioned approaches, the generalized enthalpy method is a single domain method which can describe heat and mass transfer without considering the phase distribution or phase boundaries. Gnauk et al. [19] performed macroscopic modeling of solidification and phase transformation by the generalized enthalpy method to calculate diffuse heat and solute transfer in multiphase system.

Metal matrix particulate composites (MMPCs) are an important type of materials exhibiting desirable properties such as low density, high strength or stiffness, better fatigue resistance, fire resistance and so on. MMPCs are made by dispersing a reinforcing

material into a metal matrix during melting and solidification process. The reinforcement surface can be coated to prevent a chemical reaction with the matrix. The denstiy, size and distribution of the reinforment paritlces are important to the properties of MMPCs. To achieve a disired particle distribution and composite properties, directional solidification of the metal and particle system have been investigated. The mechanism of particle pushing and engulfment has been investigated by experiment and modeling. Omenyi et al [20] observed in the experiment that the particles interact with the solidification front in various ways: continuously pushed way, instantaneously engulfed or pushed and subsequently engulfed. Uhlmann et al [21] proposed the critical velocity for the solidification front movement. Below the critical velocity, the particles are pushed away and particles are engulfed above it. Numerical simulations have been performed using different models to study the interaction between solid particles and solidification front. Generally, these numerical models can be divided into three categories: continuum model, particle model and Monte Carlo model. In the continuum model, for example Eulerian-Eulerian model, each phase is the system is treated as a continuum. The particle movement and entrapment is described as the species transport and segregation [22, 23]. In the particle model, one particle is considered and its tracking can be investigated in detail [24-26]. Xiong et al. [27] developed a macroscopic transport model for the melt and solid in Eulerian coordinates and the particle model in the Lagrangian coordinates. The particle model is composed of two parts: a model for the multi particle motion in the melt and the particle pushing and engulfment (PEP) model for the particle solidification. In the Monte Carlo model, particle movement and entrapment can be studied, but only for a small number of particles such as nano droplet solidification [28, 29].

1.1.3 Directional Solidification by Bridgman and DSS

Bridgman technique has been widely used to grow single crystals due to its simplicity and controllability. Single crystals of II-VI and III-V compounds, such as InAs, InSb, GaSe, CdTe, PbTe and GaP, have attracted much attention due to their applications in optoelectronics, sensors and X-Ray and radiation detectors. Such crystals are commonly grown by the Bridgman technique.

Much research has been conducted through experiments and numerical simulations to relate quality of grown crystals with temperature, melt convection, interface location and solute distribution in the growth system. Dupret et al. [30] performed the global calculation of heat transfer in a vertical Bridgman furnace. In the numerical model, various types of radiation heat transfer were taken into account with axisymmetric enclosures. The calculation of view factor in radiation heat transfer is computational expensive. However, for an axisymmetric geometry, which is typical for vertical Bridgman system, Durpet et al. [31] proposed an efficient method to calculate view factor, which is widely used now. Zhang et al. [32] studied the growth process of potassium bromide single crystal in a vertical rotational Bridgman furnace using an integrated model combing the global heat transfer model and elastic stress model. The effect of natural convection and rotational forced convection on the interface shape was also investigated. To capture the interface movement, Zhang et al. [33] developed multi-zone adaptive grid generation and curvilinear finite volume scheme.

Hashio and Tatsumi [34] investigated constitutional supercooling and segregation in directional solidification of $In_xGa_{1-x}As$. They found that solute transport is primarily diffusion and macroscopic fluctuation of the composition results in constitutional supercooling. Mitric [35] conducted the crystal growth of GaInSb concentrated alloys to study the effect of alternating magnetic field (AMF) on solidification process. It was revealed that for a magnetic field intensity of 3mT, the application of AMF can delay the interface destabilization and decrease the radial segregation. However for an intensity of 6mT, it can deepen the interface curvature and accelerate the destabilization. Stelian [36] performed numerical modeling on the Te-doped InSb crystal growth to analyze the baffle effect on the solute distribution. With the existence of baffle, reduction of interface curvature and radial segregation can be achieved. Hanjie Lee and Pearstein [37, 38] developed numerical model for vertical Bridgman growth of GaSe, takeing into account of heat transfer, buoyancy flow and interface deformation with anisotropic thermal conductivity. Their simulation results showed that thermal anisotropy is critical to accurate prediction of melt flow and interface shape. Kolesnikov etc [39] performed GaSe single crystal growth by high-pressure vertical zone melting scheme and attained almost perfect single crystal. Lun et al. [40] studied the effect of thermal gradient on the

interface shape for the CdZnTe growth and observed that the large furnace temperature gradient tends to flatten the solidification interface shape. They explained that by promoting a greater axial heat flux by larger temperature difference along the crystal, the axial flow of latent heat, thereby flattening the interface, can be more readily accommodated. Due to the particular thermal physical properties of CdTe, such as low thermal conductivity and low critical resolved shear stress, it is difficult to grow high quality and homogeneous single crystals with a very low dislocation. However, an effective approach proved helpful is to provide a Cd overpressure in the growth system [41]. For the CdTe single crystal growth, it is also found that the marked superheating (at least 20K, up to 110K higher than the melting point of CdTe) and long holding time (24 hours) is necessary and useful [42, 43]. Okano et al. [44] conducted the experimental and numerical studies on CdTe crystal growth by vertical gradient freezing technique. They designed a three zone furnace in which the middle portion has the highest temperature, much higher than melting point, so as to achieve a high temperature gradient near the growth interface for stable growth; meanwhile, melt temperature is reduced to slight higher than melting temperature at the upper portion of the furnace. However, they did not elaborate why they designed the temperature profile in such way.

If high Prandtl or Grashof numbers are present, the temperature field and growth interface will be strongly influenced by melt convection. A severely curved interface shape is usually formed and makes the growth difficult. To improve growth condition, many techniques were designed to control melt convection and solute segregation, including accelerated crucible rotation, ampoule tilting, submerged baffle, submerged heater, submerged vibrator, alternating magnetic fields, and dewetting, etc. In the submerged methods [45, 46] a disk-shaped heater or baffle is held approximately 1 cm above the solid-liquid interface in the vertical Bridgman system. The baffle acts as a partition, separating melt zone adjacent to the growth interface from bulk melt. The reduced melt zone near the growth interface by introducing submerged heater can significantly reduce natural convection and diffusion-controlled segregation may be reached [47]. Fedyushkin et al [48] studied the influence of vibration by positioning a submerged vibrator near the solidification interface. It was found that the thickness of the boundary layer near the solid-liquid interface was decreased, and the solidification front

was flattened due to the presence of the submerged vibrator. Muller et al [49] investigated the effect of a tilted ampoule on melt flow in semi-transparent crystal growth. They found that crucible tilting and non-constant gradient furnace in the melt zone could induce 3D flow in the growth system of semi-transparent material easier than of opaque one. Derby and co-workers [50, 51] found that tilting the axis of the ampoule strongly affected the structure and strength of melt convection, which in turn modified heat transfer and shape of the solidification interface. Both experimental observations and numerical simulations are reported by C.W. Lan etc. [52, 53] to investigate the effect of accelerated crucible rotation technique (ACRT) and angular vibration technique (AVT) on melt flow and solutal segregation. Their results show that both techniques are effective to control the interface morphology and solutal segregation. Dewetting or detachment is another crystal growth technique based on the Bridgman method. Due to the presence of a liquid meniscus, solid crystal grows without contact with the ampoule wall and therefore structure defects were decreased and ingot quality is improved. This method is widely used for InSb, GaSb and CdTe crystal growth. Duffar [54] investigated the dependence of meniscus shape on the pressure difference in the dewetting Bridgman process. They found that the pressure difference range for stable growth is much small, of the order of 100Pa. Mitric [55] studied the influence of AMF on the solute distribution and interface curvature for GaInSb growth. It is concluded that AMF can enhance the mixing of components and decrease the radial segregation and interface deflection. Currently, over 90% of commercial solar cells are made from silicon, which is in the form of single and polycrystalline crystals. Production volume of solar cells using multi-crystalline silicon (mc-Si) is higher than that using single crystal silicon due to the fact that the mc-Si can be made from cheaper raw materials while the cell made from it achieves similar efficiency as single crystal. Various techniques can produce mc-Si, such as Electromagnetic casting (EMC) and Edge-defined Film Feed (EFG) methods, directional solidification technique, etc. Among them, directional solidification technique is widely used owing to its wider tolerance to feedstock impurities and easier operation. Using this process to grow mc-Si has therefore received intensive attention recently from the aspect of experiments. For example, Kim et al. [56, 57] experimentally investigated the growth of mc-Si by the Heat Exchange Method (HEM) and conducted the

characterization of 240kg mc-Si ingot grown by GT-MX225 furnace. They observed structural defects in the ingot due to the cheaper raw materials, and that introducing gettering technology can reduce such harmful metal impurities. They also confirmed that the performance of the solar cell made from ingot grown by this technique is close to that of single crystalline silicon. Arafune et al. [58] developed the successive relaxation of supercooling (SRS) method based on the traditional traveling heater method (THM). It was revealed that small grains in the SRS ingot significantly decrease, as well as the lifetime, carbon concentration improved. Ganesh etc. [59] carried out growth rate estimation of mc-Si grown by unidirectional solidification using the growth-induced striation method. They observed the growth striation from the carbon concentration distribution using Fourier transform infrared spectrometer (FTIR) spectroscopy and estimated the growth rate between 0.34 and 0.4 mm per minute.

Due to the complexity of directional solidification process, numerical simulation becomes an important tool to assist experiments to reveal the transport phenomena, such as temperature and impurities distributions inside the grown crystal; besides it is also used to help improve the operating process. Recent work by Wu et al. [60] used numerical simulation to investigate temperature distribution in industrial directional solidification system (DSS) and heat exchange method (HEM) stations. Temperature field, stress distribution and interface shape were correlated to microstructure and defects of mc-Si ingots and the cause of difference in quality by HEM and DSS methods was discussed. In addition, possible solutions to improve the quality of grown crystals were proposed. To evaluate the candidacy of feedstock source on the grown crystals, a research-scale directional solidification furnace (Mini Caster) was constructed by Chandrasekaran et al. [61], and finite element based modeling was conducted to predict temperature distribution in an effort to optimize the furnace design and improve the operation conditions. Further, numerical simulation has helped the improvement of hot zone design. For example, a 3D global model developed by Duffar et al. [62] considers the relative movement of various parts in the furnace and it has been applied to study how the system geometry modification could improve the energy transport in the system. Since carbon and oxygen are the primary chemical impurities in mc-Si ingots, some work was performed to investigate impurity distribution in the ingot. Liu et al. [63] numerically

investigated SiC particle precipitation in the silicon melt during directional solidification. Their results indicated that SiC precipitation can be reduced through optimization of the process conditions. For example, a slow-cooling process could reduce SiC particle formation in the central region of the ingot and achieve better distribution of SiC particles. Xi et al. [64] also predicted oxygen distribution in mc-Si ingot by directional solidification, which is in good agreement with experimental data. Matsuo et al. [65] performed experimental observation and theoretical analysis of oxygen incorporation in mc-Si ingot grown by unidirectional solidification. They examined the oxygen concentration near the crucible wall using FTIR and confirmed that the oxygen was incorporated into the melt from the crucible through the Si_3N_4 coating.

The solid-liquid interface shape is important issue in unidirectional solidification since it has a great effect on thermal stress and content of impurities. The work by Chang and Wilcox [66] indicated that interface shape as well as its position can be adjusted by changing the heater and/or cooler temperature. Derby et al. [40] studied the effects of furnace gradients on interface shape during the growth of cadmium zinc telluride in eletrodynamic gradient (EDG) furnaces, and they found that higher temperature gradients employed to the crystal tend to flatten the interface. In the paper of Lan et al. [67], the effects of cycle patterns of ACRT on the flow and interface shape, as well as segregation in vertical Bridgman crystal growth were investigated. It was concluded that the proposed pulse scheme, which is a new scheme among ACRT, can minimize the interface deformation and also reduce solute segregation. Liu et al. [68] developed 2D and 3D global model for the directional solidification process with cylindrical or square crucible to predict the influence of crucible shape on melt-crystal interface shape. The simulation results showed that the shape and dimension of a crucible have important effect on the deformation of solidification interface.

1.1.4 Modeling of Multiphase Flow with Chemical Reaction

In the past decades, SiC based ceramic materials fabricated by polymer pyrolysis and synthesis becomes a promising candidate for nuclear applications [69]. This process involves in multi phases (gas/solid) and chemical reactions between different components. The source material changes phase and composition continuously during the

fabrication process. Chemical reactions and transport phenomena vary accordingly. The generated gas is released from the solid phase. Due to the density between source material and its product, shrinkage needs to be considered. The pyrolysis and synthesis technique allows the fabrication of various ceramic materials at a relative low temperature compared to the sintering technique. In addition, it allows fabricating net-shape components without suffering from size limitation in other processing [70]. Moreover, it provides better geometrical accuracy compared to conventional ceramics at significantly lower manufacturing temperature [71]. Among various advanced ceramics, silicon carbide has been proven to be a promising candidate for use in nuclear applications as inert-matrix material due to its characteristics in the following aspects. First, SiC displays a number of superior characteristics as a structural material, such as its thermal and mechanical properties, thermal sock resistance, chemical stability and low radioactivation. Second, irradiation effects on swelling and mechanical properties of high purity SiC have been evaluated, and excellent high temperature irradiation resistance was revealed by several researchers [72, 73]. Third, SiC matrix composites have been widely developed for use in advanced energy systems [74-76]. It has also been recognized that uranium carbide (UC) is an attractive fuel for certain generation IV reactors such as the gas-cooled fast reactor due to its high thermal conductivity and high melting point. Therefore, ceramic composite pellets consisting of UC particles in SiC matrix can be used as high-temperature refractory ceramic fuels due to the superior characteristics of UC and SiC.

To study binding mechanism and morphological changes in powder synthesis or sintering process, various numerical models have been developed. They can be generally categorized into two approaches, which are porous media based approach and particle based approach. Many models were developed based on porous media theory to describe macroscopic property evaluation during the synthesis or sintering process. Tarafdar and Bergman [6] developed a non-isothermal sintering model to investigate variations in local morphologies on effective transport properties. Moreover, experiments were conducted to validate the sintering model. It was found that the sintering penetration depth is strongly related to thermal penetration depth and boundary and initial temperatures. Xiao and Zhang [77] studied the melting of an alloy powder bed with shrinkage. It was concluded

that the increase of initial porosity of the powder bed can shorten the duration of preheating and also increase the surface temperature and interfacial velocities. He et al. [78] presented a general model to analyze the effects of particle convection, gas convection and radiation on the overall heat transfer. They concluded that the radiative heat transfer provided a significant contribution to the total heat transfer and particle diameter plays an important role in heat transfer. It is also concluded that particle and gas convective components show an opposite tendency to the total heat transfer.

Several particle-level models are also available, focusing on the local behaviors around the particles and study the evolution of structure and heat and mass transfer at the particle level. Jagota [79] and Derby [80] used finite element methods (FEM) to study the shape evolution of adjacent sintering particles. The effect of geometry of the microstructure on the sintering rate is also investigated. It was concluded that the assumption of spherical particle shape is reasonable to predict sintering dynamics for many different particle geometries. Gao et al. [81] presented a double particle-layer and porous medium model to simulate the gas flow and heat transfer near the surface of an immersed object in a fluidized bed. It is concluded that heat transfer rate is determined by gas velocity. Heat transfer is conduction dominated in the stifling region since gas is almost stagnant there. However in these applications, uniform particle size and zero shrinkage are usually assumed and no reaction between different components in the mixture is considered.

1.1.5 Smoothed Particle Hydrodynamics (SPH)

Smoothed particle hydrodynamics (SPH), as a mesh-free and particle method, was originally developed for modeling astrophysics [82, 83], and later widely extended for applications of problems of solid and fluid mechanics. As the major type of particle method, SPH possesses many advantages in solving some specific problems over the traditional computational methods, such as Finite Element Method (FEM) and Finite Difference Method (FDM). Based on the adaptive nature of SPH method, it can be employed to study the problems involving with free surface, moving interface and large deformation.

Being a particle method, SPH serves as a great tool to simulate multi-component, multi-physics and multiphase problems. Managhan [84, 85] first performed SPH

modeling of two-phase flow of a dust gas and exhibited the potential of SPH in simulating multiphase flow. Colagrossi and Landrini [86] addressed numerical simulation of interfacial flows by SPH. They modified the standard approximation form of spatial derivatives to diminish the effects of large density difference, i.e. small density ratio, across the interface and also revised the artificial viscosity form to improve simulation results. For multiphase macroscopic and mesoscopic flows, Hu and Adams [87] proposed an algorithm based on SPH method dealing with density discontinuity and viscosity discontinuity at phase interface, which satisfies mass conservation and ensure continuity of velocity and shear stress across the phase interface. Furthermore, this new algorithm can handle three immiscible phases, which circumvents the difficulties of calculating the normalized interface direction and curvature of the interface. In another paper by the authors [88], Hu and Adams proposed an incompressible multiphase SPH model, in which both the zero-density-variation condition and velocity-divergence-free condition are satisfied by a fractional time step integration algorithm. A new multiphase projection method is introduced to obtain non-smeared density and viscosity discontinuities.

Since multiphase flow in porous media is common in nature, and SPH is capable of simulating problem with complex geometry and large deformation, much research work is conducted on this aspect. Zhu and Fox [89] developed a pore-scale hydrodynamic dispersion model based on SPH and study Taylor dispersion and pure tracer convection. The mess-free nature of SPH and the straightforward physical interpretation of simulation results make SPH a suitable approach to study dispersion phenomena as a function of media properties and flow conditions. Due to the computational expense of SPH, Morris et al. [90] presented a suitable approach for parallelizaiton of SPH to simulate quasi-incompressible, two dimension flow through porous media. It was verified that when computational load balance was achieved, the speed of this method is proportional to the number of processors. Jiang et al. [91] conducted SPH simulation of fluid flow in isotropic porous media. Permeability was reproduced successfully from the simulated velocity field. It is confirmed that Darcy's law is valid only in the creeping flow region and SPH model is capable of capturing the key features of the fluid flow in porous media. Tartakovsky and Meakin [92] developed a SPH model to simulate immiscible and miscible fluid flow in porous media and investigated the effects of pore scale

heterogeneity and anisotropy on such flows. It was found that fluid flow is strongly influenced by the wetting properties of fluid in the presence of anisotropy.

In most numerical simulation for crystal growth process, the grid-based methods, such as finite volume method (FVM) and finite element method (FEM) are most likely used. In these methods, meshes adaptation is needed to accurately track the growth interface, which requires iterations at the interfacial boundaries between solid and liquid regions and is very computationally expensive. Rook and Dost [93] presented numerical modeling of Si_xGe_{1-x} crystal growth using SPH method. The comparison of simulation results by SPH with both experimental data and FVM simulation results showed that SPH has the strong potential for simulation of crystal growth process although it takes longer time computational time. Tartakovsky et al. [94] developed a numerical model based on SPH for reactive transport and mineral precipitation in fractural and porous materials. Growth form a nucleus in a supersaturated solution is performed by SPH model. It was discovered that initial perturbation of solid surface resulting from an irregular particle distribution could cause unstable growth. An increase in the reaction length could stablize the non-uniform surface growth. 3D reactive transport in a fracture aperture is also simulated by SPH method. It was demonstrated that SPH based model can successfully simulate complex coupled phenomena involving fluid flow, reactive transport and mineral precipitation in porous and fractured media. There is little literature of the application of SPH method in gas hydrate simulation. In a preliminary paper by Zheng et al. [95], the possibility of SPH used to study gas hydrate formation confined in pore spaces is discussed and the framework for mesoscopic pore-level model is established.

1.2 Research Objectives

The objective of this thesis is to utilize the computational approaches to investigate the multiphase flow and its application in the materials processes, especially in the following two areas: directional solidification, and pyrolysis and synthesis.

To investigate the mass transfer, convective heat transfer, phase change and melt/solid interface in directional solidification by Bridgman and DSS technique, a comprehensive computational model based on FVM will be developed. The effects of important dimensional parameters on temperature distribution and interface shape during

solidification process will be studied. To optimize the growth process, various designs including furnace geometry modification will be proposed.

SiC pyrolysis and synthesis involves continuous change of composition, microstructure, and material properties. In this thesis, a particle level mesoscopic model based on the Smoothed Particle Hydrodynamics (SPH) will be developed for modeling the synthesis of filler U_3O_8 particles and SiC matrix. The evolution of particle concentration and structure as well as composition of composite produced will be investigated. Since the process temperature and heat flux play the important roles in material quality and uniformity, the effects of heating rate at different directions, filler particle size and distribution on uniformity and microstructure of the final product will be also investigated. Uncertainty issue will be also discussed.

1.3 Outline of Present Work

The content of this thesis is organized as follows, in Chapter 1, the literature reviews on multiphase flow with solidification and chemical reaction, as well as the directional solidification by Bridgman technique and DSS is given; in Chapter 2, the fundamental issues on multiphase flow are described, including the basic concept on multiphase flow and governing equations; in Chapter 3, the fundamental knowledge on solidification is provided; in Chapter 4, the physical and mathematical models for synthesis of Uranium-ceramic nuclear fuel are presented; in Chapter 5, the numerical schemes used in the thesis are elaborated; in Chapter 6, the simulation results on multiphase flow with solidification by Bridgman technique are presented and discussed, followed by the simulation results by DSS in Chapter 7; in Chapter 8, the simulation of multiphase flow with chemical reaction in the application of synthesis of uranium-ceramic nuclear fuel is performed, and the results are summarized; in Chapter 9, conclusion and direction to future work are made.

Chapter 2

Physical and Mathematical Models for Multiphase Flow

2.1 Fundamental of Multiphase Flow

The term multiphase flow is defined as any fluid flow consisting of more than one phase or component. According to the state of the different phases or components, multiphase flow can be classified into gas/solid flow, liquid/solid flow, gas/particle flow, or bubbly flow and so on. Depending on the different specific applications, multiphase flow can also be divided into slurry flow, fluidized beds, debris flow and cavitating flow, etc. Two general topologies of multiphase flow can be identified, namely disperse flow and separated flow []. In disperse flow, there is only one continuous phase and all other phases are in forms of particles, droplets and bubbles with much smaller sizes compared to the macroscopic length scale of the flow. On the other hand separated flow contains more than one continuous phase separated by interface.

For disperse flow, two models are mostly used to simulate the multiphase flow, which are Eulerian-Lagrangian model and Eulerian-Eulerian model. In the Eulerian-Lagrangian model, which is also named trajectory model, the trajectory of the disperse phase is obtained by integrating the equation in the form of the Newton's second law. The details of the flow around the disperse phase are subsumed into assumed drag, lift and moment forces acting on and altering the trajectory of the disperse phase. The thermal condition of disperse phase can be also tracked.

In the Eulerian-Eulerian approach, which is also referred to two-fluid flow, both disperse and continuous phases are treated as the interpenetrating fluids. Ensemble-averaged mass and momentum conservations, sometimes including energy and species

conservation equations, are solved to describe the transient motion of each phase. Ensemble-averaged interactions between phases contain the drag and lifting forces and the effect of virtual mass, which is considered when a secondary phase accelerates relative to the primary phase. These interaction terms appear in the momentum balances in two phases [96].

Both approaches have their own advantages and disadvantages and the limited ranges of the applicability [96, 97]. In the Eulerian-Lagrangian approach, the interaction between different phases is modeled straightforwardly. The Euerlian-Lagrangian model is very helpful to study of fundamental physical processes [98, 99], however the computational load for tracking bubbles is high if many bubbles appear in the liquid phase. The Eulerian-Eulerian methodology is commonly adopted for interpenetrating media situations, including both highly particle loaded systems and gas-liquid mixtures. However, the Eulerian-Eulerian model neglects the discrete nature of the disperse phase and approximates its effects on the continuous phase. Inherently in this approach, averaging processes are necessary to characterize the properties of the disperse phase.

For the separated flow, there are fewer choices in methodology. Theoretically, governing equations for single phase in the two streams have to be solved, and coupled with the other phase through appropriate kinematic or dynamic conditions at the interface. Free streamline theory is an effective implementation based on such strategy.

2.2 Mathematical Model

The gas-solid flow is used as an example to illustrate the governing equation in Eulerian-Lagrangian approach and Eulerian- Eulerian approach.

2.2.1 Eulerian-Lagrangian approach

The governing equations for mass and momentum conservation for gas phase in Eulerian-Lagrangian approach can be expresses as

$$\frac{\partial}{\partial t}(\varepsilon_g \rho_g) + \nabla \cdot (\varepsilon_g \rho_g \vec{u}_g) = 0 \tag{2.1}$$

$$\frac{\partial}{\partial t}(\varepsilon_g \rho_g \vec{u}_g) + \nabla \cdot (\varepsilon_g \rho_g \vec{u}_g \vec{u}_g) = -\varepsilon_g \nabla p + \varepsilon_g \rho_g \vec{g} + \nabla \cdot (\varepsilon_g \overline{\overline{\tau}}_g) - S \tag{2.2}$$

where ε_g is the volume fraction of gas phase, ρ_g is the intrinsic gas density, $\vec{u}_g$ is the gas velocity, p is the pressure, $\overline{\overline{\tau}}_g$ is the viscous stress tensor, $\vec{g}$ is the gravitational acceleration, and S is the interaction drag force acted on the solid phase. The drag forces between gas phase and solid phase are expressed as

$$S = \frac{\sum_{i=1}^{N} D_i}{V} \tag{2.3}$$

where N denotes the total particle number in the control volume, V is the grid volume, D_i is the drag force of the gas phase acting on a single particle, which can be given as

$$D_i = \frac{1}{8} C_D \pi d_p^2 \left|\vec{u}_g - \vec{v}_i\right| (\vec{u}_g - \vec{v}_i) \tag{2.4}$$

where C_D is the drag coefficient, d_p is the particle diameter and $\vec{v}_i$ is the velocity of particle i. Drag coefficient can be written as [100]

$$C_D = \varepsilon_g^{-2.65} \begin{cases} \frac{24}{\mathrm{Re}}(1 + 0.15\,\mathrm{Re}^{0.687}) & \mathrm{Re} < 1000 \\ 0.44 & \mathrm{Re} \geq 1000 \end{cases} \tag{2.5}$$

where $\mathrm{Re} = \varepsilon_g \rho_g d_p \left|\vec{u}_g - \vec{v}_i\right| / \mu_g$.

The trajectory of the particles is modeled by applying Newton's second law of motion

$$m_i \frac{d\vec{v}_i}{dt} = D_i \tag{2.6}$$

where m_i is the mass of particle i.

2.2.2 Eulerian-Eulerian approach

The governing equations for mass and momentum in a gas-solid flow using the Eulerian-Eulerian approach, can be written as follows. For the gas phase:

$$\frac{\partial}{\partial t}(\varepsilon_g \rho_g) + \nabla \cdot (\varepsilon_g \rho_g \vec{u}_g) = 0 \tag{2.7}$$

$$\frac{\partial}{\partial t}(\varepsilon_g \rho_g \vec{u}_g) + \nabla \cdot (\varepsilon_g \rho_g \vec{u}_g \vec{u}_g) = -\varepsilon_g \nabla p + \nabla \cdot (\varepsilon_g \overline{\overline{\tau}}_g) - \beta(\vec{u}_g - \vec{u}_s) + \vec{f}_g \tag{2.8}$$

where β is the coefficient for the inter-phase momentum change term, $\vec{u}_s$ is the solid phase velocity and $\vec{f}$ presents the all external force acting on the system except the gravity.

For the solid phase:

$$\frac{\partial}{\partial t}(\varepsilon_s \rho_s) + \nabla \cdot (\varepsilon_s \rho_s \vec{u}_s) = 0 \tag{2.9}$$

$$\frac{\partial}{\partial t}(\varepsilon_s \rho_s \vec{u}_s) + \nabla \cdot (\varepsilon_s \rho_s \vec{u}_s \vec{u}_s) = -\varepsilon_s \nabla p + \nabla \cdot (\varepsilon_s \overline{\overline{\tau}}_s) + \beta(\vec{u}_g - \vec{u}_s) + \vec{f}_s \tag{2.10}$$

where ε_s is the volume fraction of sold phase, ρ_s is the intrinsic sold density, $\vec{u}_s$ is the solid velocity.

The sum of the volume fractions should be unity:

$$\sum_{k=1}^{N} \varepsilon_k = 1 \tag{2.11}$$

Many schemes for inter-phase momentum exchange are based on the Wen and Yu model [100] since it can predict reasonable results over the range of relevant solid volume fractions. The coefficient for the inter-phase momentum exchange term, β, is formulated as

$$\beta = \frac{3}{4} C_D \frac{(1-\varepsilon_s)\varepsilon_s \rho_g \left|\vec{u}_g - \vec{u}_s\right|}{d_p} (1-\varepsilon_s)^{-2.65} \tag{2.12}$$

Chapter 3

Fundamental of Solidification

Solidification is an important subject in materials science, and it is very common in many materials processes such as casting and crystal growth. The crystal quality is determined by its microstructure formed during solidification. The understanding of the solidification process is the basis of the control of crystal property and optimization of operation process [101, 102].

3.1 Driving Force of Solidification

Generation of a new solid phase in melt will change the energy of the bulk material per unit volume of solid formed, ΔG_f (see Figure 1). This ΔG_f is the thermodynamic driving force for solidification, where G_s and G_l represent the energies of s unit volume of solid and the volume of liquid transformed to make a unit volume of solid, perceptively. The sign of ΔG_f depends on temperature, which indicates the degree of undercooling. At the equilibrium melting temperature T_{MP}, ΔG_f is zero; there is no thermodynamic driving force for the phase transformation. At a temperature $T > T_{MP}$, the energy of the liquid is lower than that of the solid, and therefore a positive ΔG_f is attained to serve as a thermodynamic driving force for the melting. At a temperature $T < T_{MP}$, the energy of the liquid is higher than that of the solid, and consequently a negative ΔG_f act as a thermodynamic driving force for solidification. The undercooling (ΔT) below the equilibrium transformation temperature T_{MP} is defined as

$$\Delta T = T_{MP} - T^* \tag{3.1}$$

where T^* is the temperature at the solidification interface.

The free energy change during solidification process can be expressed as:

$$\Delta G_f = \Delta H_f - T\Delta S_f \tag{3.2}$$

where ΔS_f and ΔH_f are the entropy change and latent heat of fusion, respectively. When $T=T_{MP}$, $\Delta G_f = 0$, then an expression for the entropy of fusion is given as

$$\Delta S_f = \Delta H_f / T_{MP} \tag{3.3}$$

Therefore the free energy change can be described as follows

$$\Delta G_f = \Delta S_f \cdot \Delta T \tag{3.4}$$

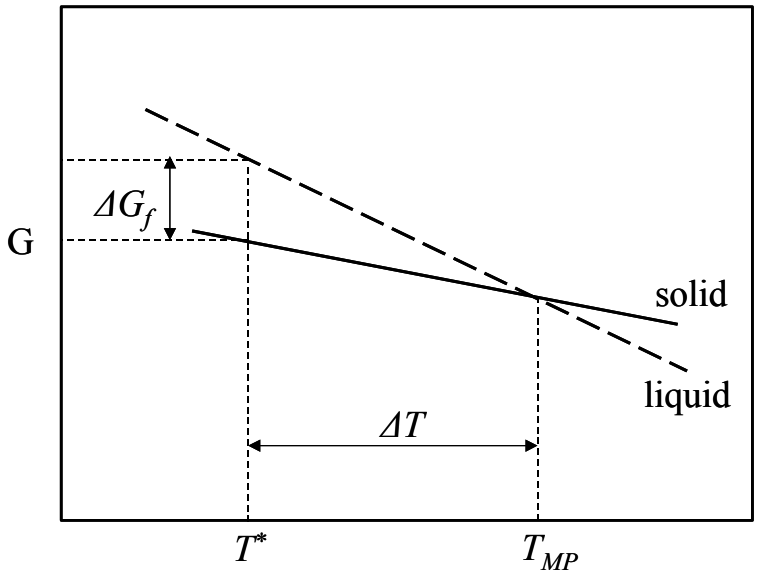

Figure 1 Free energy change during solidification process

3.2 Morphology and Interface in Solidification

Solidification morphology is critical because different morphologies lead to different geometric configurations of the melt/solid interface. In addition, different solidification morphologies are related to different latent heat release mechanisms that can significantly influence the thermal transport during solidification. Three basic solidification morphologies are planar interface, columnar celluar or dendritic, and equiaxed dendritic.

Planar interface solidification occurs under two extreme conditions: very slow and very fast interface movements. For instance, very slow interface movement is observed in single crystal growth process, e.g., Czocharalski pulling and some unidirectional

solidification processes. On the other hand, a planar solidification has also been observed in a few rapid solidification processes where the interface movement is very high. The conditions under which a stable planar interface can exist can be specified from the stability analysis. Figure 2 shows a molten bar solidified by passing a planar solid/liquid interface, normal to its axis at a velocity v. At the solid/liquid interface, the following heat flux balance conditions should be satisfied:

$$k_S G_S - k_L G_L = \Delta H_f v \tag{3.5}$$

where k_S and k_L are the thermal conductivities of the solid and liquid phase, respectively; G_S and G_L are the temperature gradients adjacent to the solid/liquid interface in the solid and liquid phase, respectively; v is the growth rate.

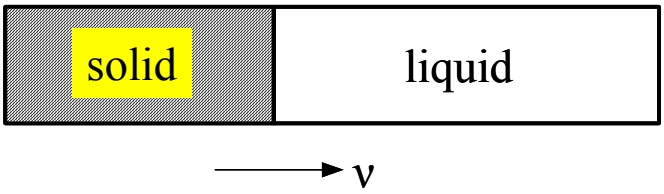

Figure 2 Schematic of directional solidification with a planar interface

When a planar interface reaches unstable conditions, it is followed by cellular or dendritic growth, causing a complex microstructure in the solidified materials. If the growth conditions are not very far from the stability criteria, cellular structures will be developed with cells growth into the melt. However for the cases where the growth conditions strongly depart from the stability condition, dendritic growth will dominate. Extensive research has been done to investigate and simulate such complicated cellular/dendritic growth.

3.3 Solute Distribution in Directional Solidification

During the solidification process, the liquid usually contains other element or compound in solution, i.e. solutes, in the presence of either deliberate additions or inadvertent impurities. Redistribution of such solutes influences the nature of solidification process and the microstructure of the generated product. The theoretical

analysis on solute distribution during solidification is given by Tiller et al [103, 104]. The schematic of solidification process by Tiller is shown in Figure 2.

To analyze the directional solidification quantitatively, Tiller assumed that the diffusion in the solid and convection mixing in the liquid is negligible. The partition coefficient k is defined as

$$k = C_l / C_s \tag{3.6}$$

where C_s is the concentration of impurity in the solid being formed, and C_l the concentration in the liquid from which it forms. And k is assumed to be constant. It should be noted that for most cases the value of k is less than unity. The interface separating solid and liquid is flat and normal to the axis of the specimen. Considering the rate of diffusion of impurity in the liquid, the equation for solute can be written as

$$D\frac{\partial^2 C_l}{\partial x^2} = \frac{\partial C_l}{\partial t} \tag{3.7}$$

where D is the diffusion coefficient of the solute in the melt and C_l is the concentration of solute in the melt. Transforming this equation into the moving solid-liquid interface coordinate will lead to

$$D\frac{\partial^2 C_l}{\partial x'^2} + V\frac{\partial C_l}{\partial x'} = \frac{\partial C_l}{\partial t} \tag{3.8}$$

where x' is the distance measured from the interface into the liquid, V is the constant rate of movement of the interface.

Chapter 4

Physical and Mathematical Model for Synthesis of Uranium-ceramic Nuclear Fuel

4.1 Mechanism of Synthesis of Uranium-ceramic Nuclear Fuel

Pyrolysis and synthesis processes of uranium-ceramic nuclear fuel are composed of four key steps. In the first step, allylhydridopolycarbosilane (AHPCS) polymer precursor (denoted as A) undergoes cross-linking to form a thermoset body (denoted as B) at 150 ^{o}C~250 ^{o}C, in which H_2 is released from the mixture. The second step is the formation of amorphous SiC (denoted as C) from B between 400 ^{o}C and 900 ^{o}C. The third step is crystallization SiC (denoted as D) from amorphous SiC above 1000 ^{o}C. The final step is the chemical reaction between SiC crystal and uranium oxide, and UC can be produced in the synthesis [105].

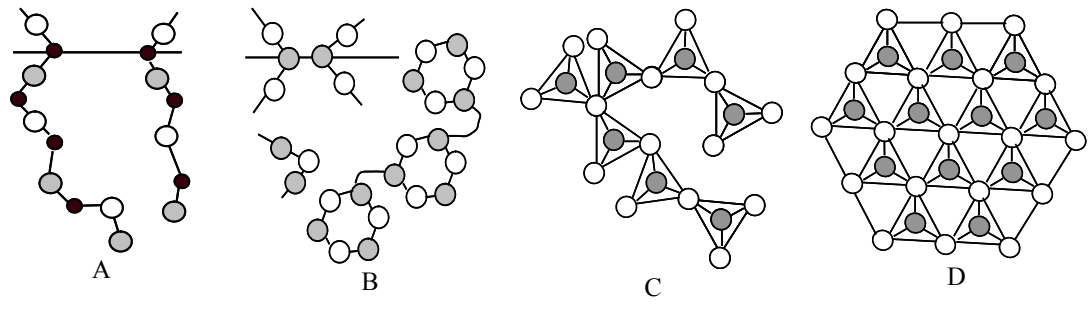

Figure 3 Schematic of polymer (carbosilane) pyrolysis process

The process above can be expressed as follows:

$$1 \text{ kg } A \rightarrow \alpha_1 \text{ kg } B + (1-\alpha_1) \text{ kg } P_1 \quad (4.1)$$

$$1\ \text{kg}\ B \rightarrow \alpha_2\ \text{kg}\ C + (1-\alpha_2)\ \text{kg}\ P_2 \quad (4.2)$$

$$1\ \text{kg}\ C \rightarrow 1\ \text{kg}\ D \quad (4.3)$$

$$1\ \text{kg}\ U_3O_8 \rightarrow \alpha_3\ \text{kg}\ UO_2 + (1-\alpha_3)\ \text{kg}\ P_3 \quad (4.4)$$

$$1\ \text{kg SiC} + \alpha_4\ \text{kg}\ UO_2 \rightarrow \alpha_5\ \text{kg UC} + (1+\alpha_4-\alpha_5-\alpha_6)\ \text{kg}\ \textit{Products} + \alpha_6\ \text{kg}\ P_4 \quad (4.5)$$

where P_1, P_2, P_3 and P_4 represent volatiles produced from reactions (4.1), (4.2), (4.4) and (4.5), respectively.

4.2 System Configuration

The sketch of pyrolysis and synthesis of uranium-ceramic nuclear fuel for process modeling is presented in Figure 4. The crucible is cylindrical. The material in the crucible is composed of SiC matrix and filler particle U_3O_8. Owing to the presence of gas in the reaction, the mixture is thought of as porous media, consisting of gases and solid particles. Due to the size difference for various particles, the granules are divided into two groups. One consists of the products of polymer pyrolysis with remaining polymer. The other is composed of produced uranium carbide and remaining U_3O_8.

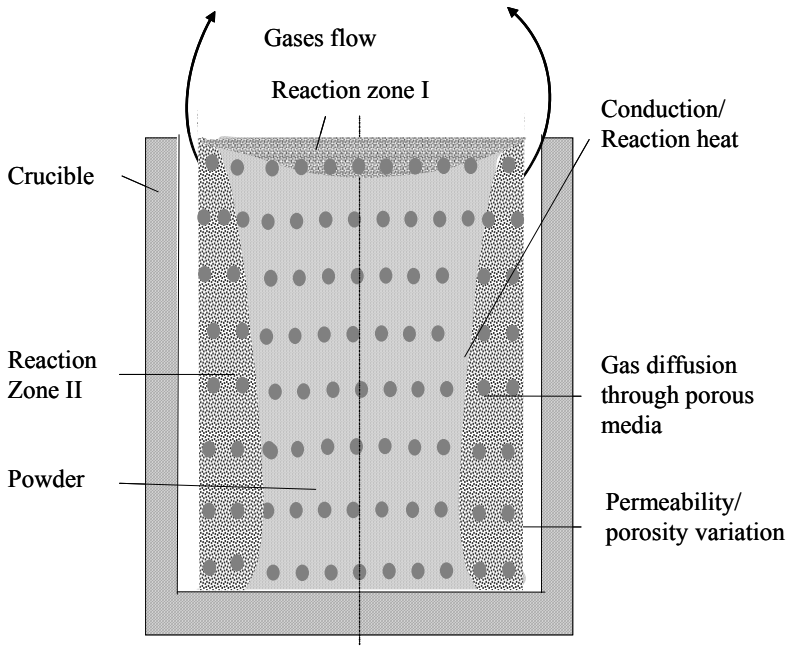

Figure 4 Schematic of the computational domain in the process model

4.3 Multi-scale Model

A multi-scale process model is developed for the process of polymer pyrolysis and synthesis with uranium oxide. The multi-scale model is capable of describing the dynamic behavior of filler particle (uranium oxide and its product) reaction, particle shape variation in the particle-level as well as transient volatiles flow, heat transfer, and species transport at the system-level. The model comprises of (i) a mesoscopic particle-level model and (ii) a porous media macroscale model transport model and two models can be integrated. Global reactions are assumed for the fabrication process and chemical mechanisms of the synthesis process are simplified through apparent kinetic parameters. Thermodynamic and kinetic data can be obtained from the designed experiments of polymer pyrolysis and reaction performed for small samples. The data can serve as input data of the porous media model to study the behavior of larger samples taking into account heat and mass transfer in the samples. Evaluation of polymer pyrolysis and particle reaction rates can be based on the experimental data of gas evaporation rate and porosity variations at various temperatures.

The porous media macroscale model for SiC-based metal-ceramic materials processing is developed to understand the thermal polymer pyrolysis, chemical reaction of active fillers, and transport phenomena in the porous media. A set of conservation equations, including continuity, momentum, energy, and species equations are solved in the macroscale model. The process model includes heat and mass transfer, curing, pyrolysis, chemical reaction and crystallization for the entire source material, e.g., a porous mixture of preceramic polymers and uranium oxide particles. Temperature variation, porosity change, reaction rate evolution, gases pressure and velocity are simulated with the macroscale model. Consequently, the pyrolysis of a larger polymer sample with required geometry of fuel pellet is simulated. The effects of heating rate on mass loss, porosity evolution, and species uniformity are investigated and the role of process temperature on material quality is determined. Active filler particle size, volume of filler, and driving force are expected to be the important parameters for material synthesis. Their effects on mass loss, gas evaporation and product uniformity are studied as well.

The mesoscopic particle-level numerical model is developed for modeling the synthesis of SiC matrix and U_3O_8. The mesoscopi model can be coupled with the macroscale model. The macroscale model provides thermal boundary conditions to the mesoscopic model. The mesoscopic model applies to the repetitive units and describes mass transport, composition changes and motion of filler particles. The unit-cell is the representation unit of source material, and it consists of several U_3O_8 particles, SiC matrix and other components produced from synthesis. Interactions between the two components are simulated with the mesoscopic model. The reactions involved in the synthesis process are the solid-solid phase reactions. Moreover, the shrinkage and motion of filler particles can be considered. Microstructures and compositions of the produced composites are studied as well. Since the control of process temperature plays an important role in material quality, the effects of heating rate and U_3O_8 particle size on species uniformity and microstructure are investigated. Optimal conditions for fuel material fabrication are determined.

4.3.1 Porous media macroscale model

4.3.1.1 Mass conservation equations of macroscale model

The following assumptions are made to simplify the governing equations

1. The gas flow is time-dependent and laminar;
2. The gas and solid phases have the same temperature locally;
3. Radiation heat transfer within the mixture can be incorporated into an effective thermal conductivity.
4. The densities of two different particles (polymer and uranium oxide) remain constant during decomposition.

Void fractions for both groups are introduced. ε_1 is defined as the specific void fraction of U_3O_8 and its yield in the total volume of the mixture and ε_2 as the specific void fraction of polymer and its yield in the remaining void volume of the mixture. Their expression can be given as

$$\varepsilon_1 = \frac{V_{total} - V_1}{V_{total}} \tag{4.6}$$

$$\varepsilon_2 = \frac{V_{total} - V_1 - V_2}{V_{total} - V_1} \tag{4.7}$$

where V_1 , V_2 and V_{total} are volumes of U_3O_8, polymer, and total volume. Thus, the porosity of the porous media ε is defined as

$$\varepsilon = \varepsilon_1 \times \varepsilon_2 = \frac{V_{total} - V_1 - V_2}{V_{total}} \tag{4.8}$$

The density of solid particles mixture is given by

$$\rho_{solid} = \frac{\rho_2 \varepsilon_1 (1-\varepsilon_2) + \rho_1 (1-\varepsilon_1)}{1-\varepsilon} \tag{4.9}$$

where ρ_1 and ρ_2 are volumes of U_3O_8 and polymer, respectively. The conservation of species (components) is given by

$$\frac{\partial[\rho_2 \varepsilon_1 (1-\varepsilon_2)]}{\partial t} = -(1-\alpha_1)\dot{R}_1 - (1-\alpha_2)\dot{R}_2 + (\alpha_4 - \alpha_5 - \alpha_6)\dot{R}_5 \tag{4.10}$$

$$\frac{\partial[\rho_1 (1-\varepsilon_1)]}{\partial t} = -(1-\alpha_3)\dot{R}_4 + (\alpha_5 - \alpha_4)\dot{R}_5 \tag{4.11}$$

Supposing that the reactions are controlled by the Arrhenius relation, the reaction rates can be expressed as:

$$\dot{R}_1 = (1-\varepsilon)\rho_s Y_A Z_1 \exp(-E_1 / RT) \tag{4.12}$$

$$\dot{R}_2 = (1-\varepsilon)\rho_s Y_B Z_2 \exp(-E_2 / RT) \tag{4.13}$$

$$\dot{R}_3 = (1-\varepsilon)\rho_s Y_C Z_3 \exp(-E_3 / RT) \tag{4.14}$$

$$\dot{R}_4 = (1-\varepsilon)\rho_s Y_{U_3O_8} Z_4 \exp(-E_4 / RT) \tag{4.15}$$

$$\dot{R}_5 = (1-\varepsilon)\rho_s Y_{UO_2} (1-\varepsilon)\rho_s Y_C Z_5 \exp(-E_5 / RT) \tag{4.16}$$

4.3.1.2 Momentum conservation equations of macrosalce model

The continuity equation under cylindrical coordinates for the whole mixture is

$$\frac{\partial}{\partial t}\left[\rho_{solid}(1-\varepsilon) + \rho_g \varepsilon\right] + \frac{1}{r}\frac{\partial}{\partial r}\left(r\varepsilon\rho_g u_r\right) + \frac{\partial}{\partial z}\left(\varepsilon\rho_g u_z\right) = 0 \tag{4.17}$$

where ρ_g is the mass density of volatiles, and u_r and u_z are the volatiles velocity components in the radial and axial direction, respectively.

Gas pressure in the powder can be derived from the Darcy's law:

$$\nabla P = \frac{\mu}{K}\vec{u} \tag{4.18}$$

where K is the local permeability of the powder.

Chemical reaction begins from both sides and top surface of the powder, thus two reaction zones (reaction zones I and II, in Figure 4.2) are formed. It's supposed that colatieles produced in the reaction zone I is released from the top surface with an axial velocity u_z only, neglecting the radial velocity u_r. Thus momentum equatjion in the reaction zone I can be simplified as

$$P(r,z) = P_{s,top}(r) + \int \frac{\mu}{K(r,z)} u_z(r,z)dz \tag{4.19}$$

where $P_{s,top}$ is the gas pressure at the top surface of the powder.

Volatiles produced in the reaction zone II escape from the side surface of the powder with radial velocity u_r only. In the reaction zone II, the momentum equation can be simplified as:

$$P(r,z) = P_{s,side}(z) + \int \frac{\mu}{K(r,z)} u_r(r,z)dr \tag{4.20}$$

where $P_{s,side}(z)$ is the gas pressure at the side surface of the powder.

Moreover, volatiles can escape from the mixed powder by the driving force P_{df} induced by natural and forced convection. The forced convection results in the pressure difference (ΔP_1) between furnace and outside environment. The driving force induced by natural convection (ΔP_2) results from the density difference between gas at the top or side surface of the mixed powder and that at environment. ΔP_2 can be described as a function of temperature difference. Thus,

$$P_{df} = \Delta P_1 + \Delta P_2 \tag{4.21}$$

$$\Delta P_2 = \rho_{\arg on} g\beta \Delta T \Delta Z \tag{4.22}$$

where β is the thermal expansion coefficient for the argon gas and ΔZ is the elevation difference., ΔT in the reaction zones I and II are expressed as Eqs. (4.23) and (4.24), respectively:

$$\Delta T = T(r,L) - T_\infty \tag{4.23}$$

$$\Delta T = T(R,z) - T_\infty \tag{4.24}$$

The size and movement of reaction zone are determined by the driving force, porosity and permeability of the mixed powder, and the reaction rate.

4.3.1.3 Energy conservation equation of macroscale model

Under cylindrical coordinates, the conservation of energy is expressed as

$$[\varepsilon\rho_g c_{pg} + (1-\varepsilon)\rho_{solid} c_{ps}]\frac{\partial T}{\partial t} + \frac{1}{r}\frac{d}{dr}\left(\rho_g u c_{pg} T\right) = \frac{\partial}{\partial x}(k\frac{\partial T}{\partial x}) + \frac{1}{r}\frac{\partial}{\partial r}\left(rk\frac{\partial T}{\partial r}\right) + \sum_{i=1}^{5}\Delta H_i R_i \qquad (4.25)$$

where ρ_g and ρ_{solid} are bulk densities of the gaseous product and the mixed solid, respectively, c_{pg} and c_{ps} are specific heats of gases and mixed solid, respectively, k is the effective thermal conductivity of porous media, and ΔH_i i=1, 2, 3, 4 ,5 is i^{th} reaction heat.

The thermal conductivity of the mixture can be taken as a volume-weighted average, given by

$$k_{eff} = f_1 k_{1,eff} + f_2 k_{2,eff} \qquad (4.26)$$

where f_1 and f_2 are volume fractions of U_3O_8, and polymer respectively, $k_{1,eff}$ and $k_{2,eff}$ are effective thermal conductivities of U_3O_8 and polymer, respectively.

4.3.2 Mesoscopic particle-level model

The sketch of mesoscopic model is presented in Figure 5. The computational domain for local model is one macrocell selected from system-level calculation domain. Each macrocell is the representation unit of the source material, which consists of several U_3O_8 particles, SiC matrix and other components produced from the synthesis process. The mesoscopic particle-level model applies to a repetitive macrocell unit for microstructure evolution calculation. The temperature boundary condition for the chosen marcocell can be obtained from its neighbor cells by interpolating the nearest neighbor macrocell temperature to the boundary.

The mesoscopic computational domain, consisting of SiC matrix and U_3O_8 is represented by a set of particles. The reaction mechanism of the synthesis of SiC matrix and U_3O_8 are not clear yet by experiment. It is assumed that the synthesis process contains two key reactions, described by Equations (4.4) and (4.5). If the temperature of a U_3O_8 particle with the mass of m is above 1200˚C, it will be converted into UO_2 with the mass of a_3m. If the concentration of SiC in a UO_2 particle is above a critical concentration and the temperature of the UO_2 particle with the mass of m' is above 1400˚C, the UO_2 particle will be converted into UC particle, the mass of this particle

changes to $a_5\ m'$. The critical concentration ensures that there is enough SiC to synthesize with the UO_2 particle, and is determined by α_4 in the reaction (4.5).

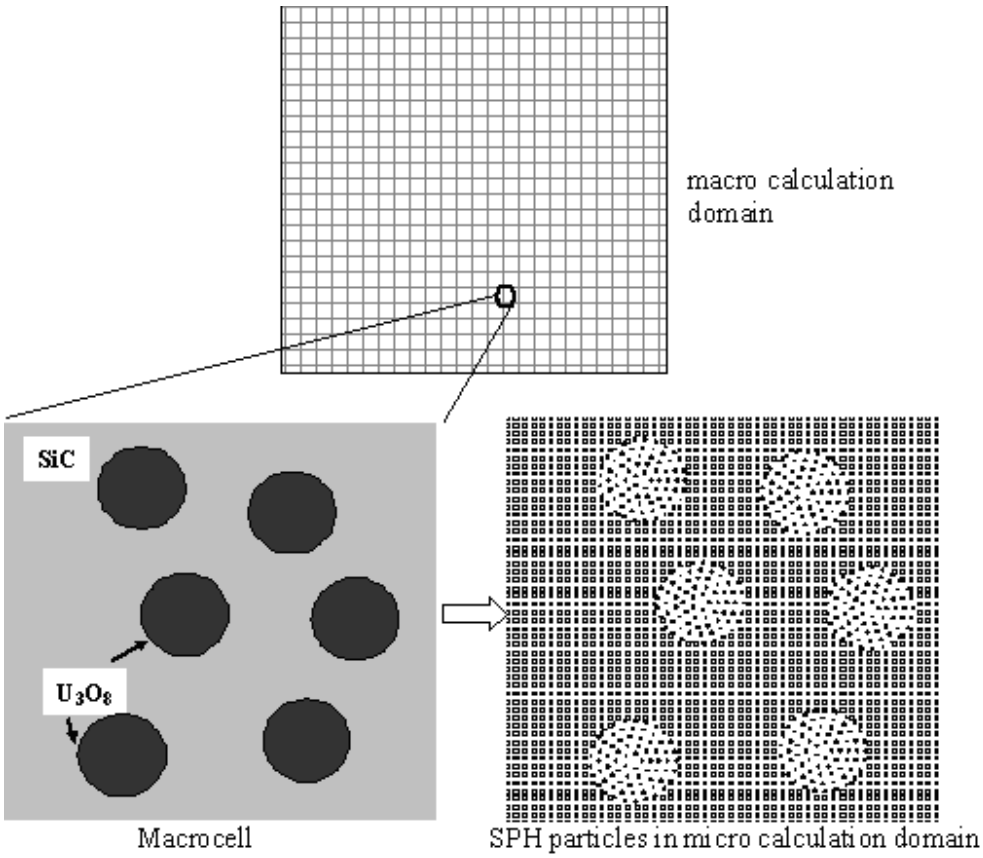

Figure 5 Schematic of the particle-level model

4.3.2.1 Continuity equation of SiC matrix and filler particles

The mass conservation equation is expressed

$$\frac{\partial \rho_i}{\partial t} + \nabla \cdot \left(\rho_i \vec{u} \right) = \dot{m}_i \tag{4.27}$$

where ρ_i is the density of SiC matrix or filler particles; $\dot{m}_i$ is the source terms due to chemical reactions.

4.3.2.2 Momentum equation of filler particles

It is assumed that the shrinkage of U_3O_8/UO_2 particles occurs once they are converted into UO_2/UC particles. Gaps between the filler particles and SiC matrix are formed. It is further assumed that the filler particles move in the gaps with the same translational velocity of SiC matrix. The motion of filler particles is driven by a buoyancy force induced by the total gas pressure on the filler particles. The total pressure on each filler particle is the summation of the gas pressures exerted by all the particles composing the filler particle. The total pressure can be expressed as

$$p = \sum_i p_i \tag{4.28}$$

where p_i is the pressure of gas *i*.

Moreover, the interaction between SiC matrix and filler particles is considered. The structure of SiC matrix forms a force to impede the motion of the filler particles. It is assumed that the impedance of the motion is induced by springs around the filler particles.

4.3.2.3 Energy conservation equation

The governing equation of the energy is:

$$\frac{\partial}{\partial t}(\rho c_p T) + \nabla \cdot (\rho c_p \vec{u} T) = \nabla \cdot \left(k \nabla T\right) + \dot{Q} \tag{4.29}$$

where c_p and κ are the specific heat and thermal conductivity, respectively; $\dot{Q}$ is the source terms due to chemical reactions. In the current particle-level model, heat fluxes provided by system-level model are applied to all the boundaries. Temperature boundary condition can be obtained from the macro neighbor cells of the selected cell. The outmost macrocells are set to time dependent temperature, which are calculated by interpolating the nearest neighbor macrocell temperature to the boundary. Virtual particles are added as boundary particles in the problem considered here. It is assumed that the heat transferred to every boundary particles at the same boundary is identical. The SPH particles exchange heat and material with neighboring particles whether they are of the same or different phase.

4.3.2.4 SiC diffusion equation

It is assumed that SiC particles are stationary due to the matrix structure; nevertheless, diffusion of SiC occurs according to Eq. (4.9) as follows, therefore, the synthesis of SiC and UO_2 can occur. The governing equation of the diffusion is:

$$\frac{\partial Y_i}{\partial t} + \nabla \cdot \left(\vec{u} Y_i \right) = \frac{1}{\rho} \nabla \cdot (D \nabla Y_i) + \dot{Y}_i \tag{4.30}$$

where $\dot{Y}_i$ Y is the mass fraction of SiC matrix or filler particle, and D is the diffusion coefficient; $\dot{Y}$ is the source terms due to chemical reactions. The computational methodology is to assume all the SPH particles in the computational domain hold a concentration of SiC. During the diffusion process, the SiC concentration increases for the U_3O_8 particles, and decreases for the SiC particles.

Chapter 5

Numerical Method

The computational scheme used in the thesis is introduced in this chapter. Two important numerical methods are discussed, i.e., Multi-zone Adaptive Scheme for Transport and Phase-change Processes **(**MASTRAPP) for the Bridgman crystal growth, and Smoothed Particle Hydrodynamics (SPH) for synthesis of uranium-ceramic nuclear fuel. The first scheme is capable of accurately simulating the interface moving during solidification. And the second one has the advantage of studying the evolution of microstructure and species during the synthesis process.

5.1. Multi-zone Adaptive Scheme for Transport and Phase-change Processes (MASTRAPP)

5.1.1 Multi-zone adaptive grid generation (MAGG)

The crystal growth process is involved phase change, and therefore the solid-liquid interface keeps moving, which needs the adaptive grid generation. Consequently, the grids in both melt zone and solid zone is constantly adjusted after each step of iteration for fluid flow and heat conduction calculations.

To accurately and efficiently tracking the melt-crystal interface and its related parameters, the grid lines should be well fitted with the interface shape. In this thesis, the numerical methodology is developed based on the multi-zone adaptive grid generation (MAGG) technique of Zhang and co-workers [106-108] near the melt-solid interface. The MAGG scheme is based on variational principles and has been proved to be very effective for phase change problems.

In order to facilitate the accurate representation of irregular geometries, $\vec{x} = (x, r)$ and $\vec{\xi} = (\xi, \eta)$ are used to denote the physical and computational coordinates,

respectively, and (ξ, ζ) are the body-fitted non-orthogonal coordinate system. The one-to-one coordinate transformation from the computational (or logical) domain Ω_c to the physical domain Ω_p can be denoted by:

$$\vec{x} = \vec{x}(\vec{\xi}), \vec{\xi} \in \Omega_c, \tag{5.1}$$

and its inversion is denoted by:

$$\vec{\xi} = \vec{\xi}(\vec{x}), \vec{x} \in \Omega_p. \tag{5.2}$$

The grid generator MAGG is used for mapping of a grid in the physical domain Ω_p onto the computational domain Ω_c. The boundary fitted coordinate ξ and η, though non-orthogonal in physical domain, are orthogonal in computational domain with integral values (Figure 6).

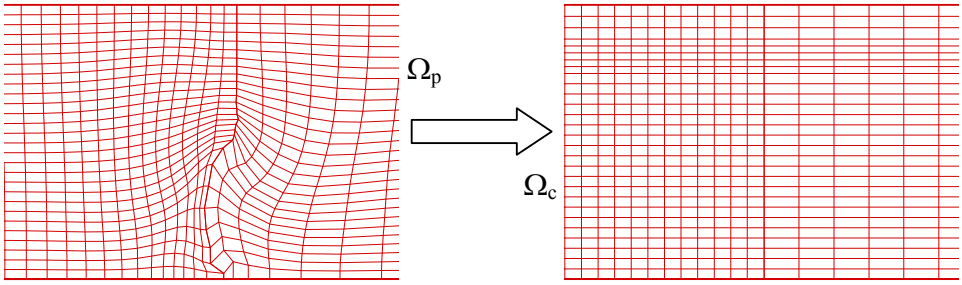

Figure 6 MAGG grid mapping from physical domain to computational domain

For grid generation, as pointed by Brackbill and Saltzman [109], the properties of the grid is defined by the differential properties of the mapping of $x=x(\xi, \eta)$ and $y=y(\xi, \eta)$. Those differential properties are defined by the following functions, includes a measure of smoothness of the grid lines I_s, a measure of the orthogonality of the grid lines I_o and a measure of the area of the grid cells I_w.

$$I_s = \iint_{\Omega_p} \left[(\nabla \xi)^2 + (\nabla \eta)^2 \right] dxdy = \iint_{\Omega_c} \frac{1}{Ja} \left(x_\xi^2 + x_\eta^2 + y_\xi^2 + y_\eta^2 \right) d\xi d\eta \tag{5.3}$$

$$I_o = \iint_{\Omega_p} G(\nabla \xi \cdot \nabla \eta)^2 Ja^3 \, dxdy = \iint_{\Omega_c} G\left(x_\xi x_\eta + y_\xi y_\eta \right)^2 d\xi d\eta \tag{5.4}$$

$$I_w = \iint_{\Omega_p} WJa \, dxdy = \iint_{\Omega_c} WJa^2 \, d\xi d\eta \tag{5.5}$$

where W, G are weight functions specified to control grid volume and orthogonality, respectively. The choice of the weight functions is problem dependent, as discussed by Zhang et al. [106]. In Eqs. (5.3)-(5.5), *Ja* is the Jacobian of the mapping, given by

$$Ja = x_\xi y_\eta - x_\eta y_\xi \tag{5.6}$$

The grid mapping method is conducted through minimizing a weighted sum of those integrals:

$$I = I_s + \lambda_o I_o + \lambda_w I_w = \iint_{\Omega_c} F d\xi d\eta \tag{5.7}$$

where λ_o and λ_w are weight coefficient for I_o and I_w, respectively. F is defined by

$$F = \frac{1}{Ja}\left(x_\xi^2 + x_\eta^2 + y_\xi^2 + y_\eta^2\right) + G\left(x_\xi x_\eta + y_\xi y_\eta\right)^2 + WJa^2, \tag{5.8}$$

which is the "performance function" of the optimization problem.

The Euler equations for the variational problem of Eq. (5.8) form a system of partial differential equations from which the coordinates of the grid nodes are calculated:

$$\left(\frac{\partial}{\partial x} - \frac{\partial}{\partial \xi}\frac{\partial}{\partial x_\xi} - \frac{\partial}{\partial \eta}\frac{\partial}{\partial x_\eta}\right)F = 0 \tag{5.9}$$

$$\left(\frac{\partial}{\partial y} - \frac{\partial}{\partial \xi}\frac{\partial}{\partial y_\xi} - \frac{\partial}{\partial \eta}\frac{\partial}{\partial y_\eta}\right)F = 0 \tag{5.10}$$

At the liquid and solid interface, the grid-generation via the variational problem subject to the constraints of the dynamics of interface movement, and the interface dynamics will be discussed in Section 5.2. Assume the constrains has a form of:

$$g_I \equiv g_I(x, y) = 0 \text{ for } \eta = \eta_I \tag{5.11}$$

where g_I are known real-valued functions with respect to arguments x and y, which are implicit function of ξ and η, and define the interfaces for constant η_I values. The above constrained optimization problems can be converted to unconstrained ones by introducing Lagrange multipliers Λ_I to form augmented functions [106]. As a result, the performance function F is rewritten as:

$$F = \frac{1}{Ja}\left(x_\xi^2 + x_\eta^2 + y_\xi^2 + y_\eta^2\right) + G\left(x_\xi x_\eta + y_\xi y_\eta\right)^2 + WJa^2 + \Lambda_1 g_I \tag{5.12}$$

Finally, F is substituted into Eq. (5.9)-(5.10) to complete the Euler-Lagrange equation for the melt-crystal interfaces.

The finite difference approximation of the Euler- Lagrange equations are formed and solved by the successive over relaxation (SOR) method to determine the coordinates of the grid points.

5.2 Solid-Liquid Interface Dynamics

The condition at the solid-liquid interface needs special considerations. A non-slip condition is imposed for melt flow, and the solidification of a pure substance or eutectic material is modeled with a fixed temperature at the interface,

$$T_I = T_{MP} - \Delta T \tag{5.13}$$

where T_{MP} and ΔT represent melting temperature and undercooling temperature along the interface. If faceting is not considered, ΔT is almost isotropic. The solid and liquid phases are therefore separated by a sharp interface, $f(z,r,t) = s(r,t) - z = 0$, where s is the dimensionless height of the crystal/melt interface. From the energy balance equation, s can be obtained by [33]:

$$\frac{\partial s}{\partial t} - U(t) = \frac{Ste_l}{\mathrm{Pr}}\left(\frac{k_s}{k_m}\frac{\partial \theta_s}{\partial z} - \frac{\partial \theta_m}{\partial z}\right)\left[1 + \left(\frac{\partial s}{\partial r}\right)^2\right] \tag{5.14}$$

where $Ste_l = C_{pl}(T_h - T_f)/h_f$ is the Stefan number of the melt and $U(t)$ is the moving velocity of the furnace (or ampoule). If the internal radiation is considered for semitransparent crystals, Eq. (5.14) can be rewritten as follows:

$$\frac{\partial s}{\partial t} - U(t) = \frac{Ste_l}{\mathrm{Pr}}\left[\frac{k_s}{k_l}\frac{\partial \theta_s}{\partial z} - \frac{\partial \theta_l}{\partial z} - \frac{bn^2 \varepsilon \sigma}{k_l \Delta T}\left(T_I^4 - T_a^4\right)\right]\left[1 + \left(\frac{\partial s}{\partial r}\right)^2\right] \tag{5.15}$$

where T_a is the ambient temperature respect to the melt-crystal interface. T_I is the temperature at the interface. The additional term in RHS of Eq. (5.15) is due to the radiation heat transfer between the interface and the surrounding.

For semitransparent crystals, internal radiation can be calculated by the Rosseland approximation, which consider the radiation by the effective crystal thermal conductivity while the melt is assumed opaque to internal radiation. Therefore the conservation of

energy in the as-grown crystal can still follow the energy equation in Chapter 2 except k_s is replaced by the effective thermal conductivity $k_{s,eff}$ [110, 111]:

$$k_{s,eff} = k_s + \frac{16n^2\sigma T^3}{3a_R} \tag{5.16}$$

where n is the refractive index, σ the Stefan-Boltzmann constant, and a_R the Rosseland mean absorption coefficient.

The temperature field at the solid-liquid interface will be anisotropic if faceting is considered. This anisotropy is explained by the anisotropic kinetic undercooling along the liquid-solid interface.

In order to assign the interface temperature boundary, the position of the melt-crystal interface must be located. In this thesis, MASTRAPP numerical scheme is used to simulate the global heat transfer in the proposed design solving governing equations of mass, momentum, and energy [33, 112] and in this process, the interface location is dynamically simulated by the following steps as follows: (i) First, the temperature distribution in the solid, melt and ampoule, flow and concentration fields in the melt, and the shape of the solid/melt interface are given as initial conditions; (ii) The temperature profile at the ampoule wall moves at a rate, U , and a new temperature profile at the wall is obtained accordingly; (iii) A new interface line is computed using $s^{n+1} = s^n + (\partial s / \partial t)^n \Delta t$; (iv) Converged flow field, temperature and concentration distributions are predicted using the new interface; (v) The velocities of the grid movements are calculated thereafter; (vi) The procedure is repeated starting from (ii). The technology of multiple adaptive grid generation (MAGG) makes the above procedure possible and allows the interface to be captured accurately and efficiently.

5.2 Smoothed Particle Hydrodynamics (SPH)

In this part, the introduction about the basic theory on Smoothed Particle Hydrodynamics (SPH) will be given. SPH, as a meshfree and particle method, was originally developed for modeling astrophysics, and later widely extended for applications of problems of solid and fluid mechanics. As the major type of particle method, SPH possesses many advantages in solving some specific problems over the traditional computational methods, such as Finite Element Method (FEM) and Finite Difference Method (FDM). Based on the adaptive nature of SPH method, it can be employed to study the problems involving with free surface, moving interface and large deformation.

The basic ideas of SPH are described as follows. After the system is represented by a number of arbitrarily distributed particles, the function approximation and then particle approximation are employed to the original PDEs to obtain a set of ODEs in a discretized form with respect to time only. The ODEs can be solved using an explicit integration approach to get convergent results.

5.2.1 Integral representation of a function and its derivative

The integral representation of $f(x)$ is addressed as

$$f(x) \doteq \int_{\Omega} f(x')W(x-x',h)dx' \tag{5.17}$$

where $W(x\text{-}x',h)$ is called the smoothing function or kernel function. In the smoothing function, h is the smoothing length determining the influence area of the smoothing function W. The kernel approximation operator is usually marked by the angle bracket <> which is expressed as

$$< f(x) >= \int_{\Omega} f(x')W(x-x',h)dx' \tag{5.18}$$

The smoothing function W is usually chosen to be an even function. Several limitations are set on it. Firstly, it should satisfy the normalization condition

$$\int_{\Omega} W(x-x',h)dx' = 1 \tag{5.19}$$

Secondly, the Delta function property is observed when the smoothing length h is approaching zero

$$\lim_{h\to 0} W(x-x',h) = \delta(x-x') \tag{5.20}$$

where $\delta(x\text{-}x')$ is the Delta function kernel. The third one is the compact condition

$$W(x-x',h) = 0 \text{, when } |x-x'| > kh \tag{5.21}$$

where k is a constant related to the smoothing function.

The cubic spline kernel function is widely used, which is described as

$$W(R,h) = a_d \times \begin{cases} \frac{2}{3} - R^2 + \frac{1}{2}R^3 & 0 \le R < 1 \\ \frac{1}{6}(2-R)^3 & 1 \le R < 2 \\ 0 & 2 \le R \end{cases} \tag{5.22}$$

where a_d is $\frac{1}{h}$, $\frac{15}{7\pi h^2}$ and $\frac{3}{2\pi h^3}$ in one, two, three dimensional space, respectively.

To approximate the spatial derivative $\nabla \cdot f(x)$, $f(x)$ is substitute with $\nabla \cdot f(x)$ and plugged into the equation (3.1)

$$< \nabla \cdot f(x) >= \int_{\Omega} [\nabla \cdot f(x')] W(x-x',h) dx' \tag{5.23}$$

Finally, it can be simplified as

$$< \nabla \cdot f(x) >= -\int_{\Omega} f(x') \cdot \nabla W(x-x',h) dx' \tag{5.24}$$

5.2.2 Particle approximation

The particle approximation for a function $f(x)$ at particle i can be expressed as

$$f(x_i) = \sum_{j=1}^{N} \frac{m_j}{\rho_j} f(x_j) W(x_i - x_j, h) \tag{5.25}$$

and it can also written as

$$< f(x_i) >= \sum_{j=1}^{N} \frac{m_j}{\rho_j} f(x_j) W_{ij} \tag{5.26}$$

where $W_{ij} = W(x_i - x_j, h) = W(r_{ij}, h)$.

The particle approximation for the spatial derivative of the function can be given by

$$< \nabla \cdot f(x_i) >= -\sum_{j=1}^{N} \frac{m_j}{\rho_j} f(x_j) \cdot \nabla_i W_{ij} \tag{5.27}$$

where $\nabla_i W_{ij} = \frac{x_i - x_j}{r_{ij}} \frac{\partial W_{ij}}{\partial r_{ij}} = \frac{x_{ij}}{r_{ij}} \frac{\partial W_{ij}}{\partial r_{ij}}$.

5.2.3 Navier-Stokes equations in Lagrangian forms

The basic governing equations for fluid mechanics include the conservation of mass, momentum and energy, which are well known as Navier-Stokes equations, and they can be expressed as a set of PDEs in Lagrangian form. If α and β denote the coordinate directions, and Einstein summation is performed to the repeated indices, Navier-Stokes equation in Lagrangian form can be expressed as

continuity equation

$$\frac{D\rho}{Dt} = -\rho \frac{\partial v^\beta}{\partial x^\beta} \tag{5.28}$$

momentum equation without external forces

$$\frac{Dv^\alpha}{Dt} = \frac{1}{\rho} \frac{\partial \sigma^{\alpha\beta}}{\partial x^\beta} \tag{5.29}$$

energy equation

$$\frac{De}{Dt} = \frac{\sigma^{\alpha\beta}}{\rho} \frac{\partial v^\alpha}{\partial x^\beta} \tag{5.30}$$

where σ is the total stress tensor, which consists of isotropic pressure p and viscous stress τ. It is given by

$$\sigma^{\alpha\beta} = -p\delta^{\alpha\beta} + \tau^{\alpha\beta} \tag{5.31}$$

The viscous shear stress τ is proportional to the shear strain rate ε for the Newtonian fluid:

$$\tau^{\alpha\beta} = \mu \varepsilon^{\alpha\beta} \tag{5.32}$$

$$\varepsilon^{\alpha\beta} = \frac{\partial v^\beta}{\partial x^\alpha} + \frac{\partial v^\alpha}{\partial x^\beta} - \frac{2}{3}(\nabla \cdot v)\delta^{\alpha\beta} \tag{5.33}$$

where μ is dynamic viscosity.

5.2.4 SPH formulations for Navier-Stokes equations

5.2.4.1 Particle approximation of density

According to the continuity equation (5.28), the particle approximation of density can be given by

$$\frac{D\rho_i}{Dt} = -\rho_i \sum_{j=1}^{N} \frac{m_j}{\rho_j} v_j^{\beta} \frac{\partial W_{ij}}{\partial x_i^{\beta}} \tag{5.34}$$

Other alternative formulations include

$$\frac{D\rho_i}{Dt} = \rho_i \sum_{j=1}^{N} \frac{m_j}{\rho_j} v_{ij}^{\beta} \frac{\partial W_{ij}}{\partial x_i^{\beta}} \tag{5.35}$$

$$\frac{D\rho_i}{Dt} = \sum_{j=1}^{N} m_j v_{ij}^{\beta} \frac{\partial W_{ij}}{\partial x_i^{\beta}} \tag{5.36}$$

where $v_{ij} = v_i - v_j$

5.2.4.2 Particle approximation of momentum

Based on the momentum equation, the particle approximation of momentum evolution can be expressed as [113]

$$\frac{Dv_i^{\alpha}}{Dt} = \frac{1}{\rho_i} \sum_{j=1}^{N} m_j \frac{\sigma_j^{\alpha\beta}}{\rho_j} \frac{\partial W_{ij}}{\partial x_i^{\beta}} \tag{5.37}$$

Adding the following identity

$$\sum_{j=1}^{N} m_j \frac{\sigma_j^{\alpha\beta}}{\rho_j \rho_i} \frac{\partial W_{ij}}{\partial x_i^{\beta}} = \frac{\sigma_j^{\alpha\beta}}{\rho_i} \left(\sum_{j=1}^{N} \frac{m_j}{\rho_j} \frac{\partial W_{ij}}{\partial x_i^{\beta}} \right) = 0 \tag{5.38}$$

to equation (5.37) leads to

$$\frac{Dv_i^{\alpha}}{Dt} = \sum_{j=1}^{N} m_j \frac{\sigma_j^{\alpha\beta} + \sigma_j^{\beta\alpha}}{\rho_j \rho_i} \frac{\partial W_{ij}}{\partial x_i^{\beta}} \tag{5.39}$$

Another commonly used formulation of momentum evolution is written as

$$\frac{Dv_i^{\alpha}}{Dt} = \sum_{j=1}^{N} m_j \left(\frac{\sigma_i^{\alpha\beta}}{\rho_i^2} + \frac{\sigma_j^{\alpha\beta}}{\rho_j^2} \right) \frac{\partial W_{ij}}{\partial x_i^{\beta}} \tag{5.40}$$

Considering equation (5.38), equations (5.39) and (5.40) can be expressed, respectively, in detail

$$\frac{Dv_i^{\alpha}}{Dt} = -\sum_{j=1}^{N} m_j \frac{p_i + p_j}{\rho_i \rho_j} \frac{\partial W_{ij}}{\partial x_i^{\alpha}} + \sum_{j=1}^{N} m_j \frac{\mu_i \varepsilon_i^{\alpha\beta} + \mu_j \varepsilon_j^{\alpha\beta}}{\rho_i \rho_j} \frac{\partial W_{ij}}{\partial x_i^{\beta}}$$

and

$$\frac{Dv_i^\alpha}{Dt} = -\sum_{j=1}^{N} m_j \left(\frac{p_i}{\rho_i^2} + \frac{p_j}{\rho_j^2} \right) \frac{\partial W_{ij}}{\partial x_i^\alpha} + \sum_{j=1}^{N} m_j \left(\frac{\mu_i \varepsilon_i^{\alpha\beta}}{\rho_i^2} + \frac{\mu_j \varepsilon_j^{\alpha\beta}}{\rho_j^2} \right) \frac{\partial W_{ij}}{\partial x_i^\beta} \tag{5.41}$$

The SPH approximation of viscous stress $\varepsilon^{\alpha\beta}$ for particle *i* can be given as

$$\varepsilon_i^{\alpha\beta} = -\sum_{j=1}^{N} \frac{m_j}{\rho_j} v_j^\beta \frac{\partial W_{ij}}{\partial x_i^\alpha} + \sum_{j=1}^{N} \frac{m_j}{\rho_j} v_j^\alpha \frac{\partial W_{ij}}{\partial x_i^\beta} - \left(\frac{2}{3} \sum_{j=1}^{N} \frac{m_j}{\rho_j} v_j \cdot \nabla_i W_{ij} \right) \delta^{\alpha\beta} \tag{5.42}$$

or

$$\varepsilon_i^{\alpha\beta} = -\sum_{j=1}^{N} \frac{m_j}{\rho_j} v_{ji}^\beta \frac{\partial W_{ij}}{\partial x_i^\alpha} + \sum_{j=1}^{N} \frac{m_j}{\rho_j} v_{ji}^\alpha \frac{\partial W_{ij}}{\partial x_i^\beta} - \left(\frac{2}{3} \sum_{j=1}^{N} \frac{m_j}{\rho_j} v_{ji} \cdot \nabla_i W_{ij} \right) \delta^{\alpha\beta} \tag{5.43}$$

To simulate low Reynolds number incompressible flows, the following momentum evolution approach is used

$$\frac{Dv_i^\alpha}{Dt} = -\sum_{j=1}^{N} m_j \left(\frac{p_i}{\rho_i^2} + \frac{p_j}{\rho_j^2} \right) \frac{\partial W_{ij}}{\partial x_i^\alpha} + \sum_{j=1}^{N} m_j \frac{\mu_i + \mu_j}{\rho_i \rho_j} v_{ij}^\beta \left(\frac{1}{r_{ij}} \frac{\partial W_{ij}}{\partial r_{ij}^\beta} \right) \tag{5.44}$$

For incompressible flow, small time step results in the fact that a theoretically incompressible flow is treated as a compressible one. This treatment leads to the concept of artificial compressibility. A probable choice of the artificial equation of state is

$$p = c^2 \rho \tag{5.45}$$

where *c* is numerical sound speed. For fluid flow in porous media, the momentum equation includes a drag force term, which can be expressed as

$$\eta \frac{Dv}{Dt} = -\phi \nabla p + \eta g + \phi \mu \nabla (\nabla v) - \nabla f_d \tag{5.46}$$

where $\eta = \phi \rho$ is the apparent density, and f_d is the drag force expressed as

$$f_d = \phi \mu K^{-1} v \tag{5.47}$$

where *K* is the permeability and μ is the dynamic viscosity. The particle approximation of momentum equation is as follows:

$$\frac{Dv_i^\alpha}{Dt} = -\phi_i \sum_{j=1}^{N} m_j \left(\frac{p_i}{\rho_i^2} + \frac{p_j}{\rho_j^2} \right) \frac{\partial W_{ij}}{\partial x_i^\alpha} + \phi_i \sum_{j=1}^{N} m_j \frac{\mu_i + \mu_j}{\rho_i \rho_j} v_{ij}^\beta \left(\frac{1}{r_{ij}} \frac{\partial W_{ij}}{\partial x_i^\alpha} \right) - \phi_i^2 \mu K_i^{-1} \frac{v_i}{\eta_i} \tag{5.48}$$

5.2.4.3 Particle approximation of energy

The most frequently used SPH formulations for energy are as follows

$$\frac{De_i}{Dt} = \frac{1}{2}\sum_{j=1}^{N} m_j \left(\frac{p_i}{\rho_i^2} + \frac{p_j}{\rho_j^2} \right) v_{ij}^{\beta} \frac{\partial W_{ij}}{\partial x_i^{\beta}} + \frac{\mu_i}{2\rho_i} \varepsilon_i^{\alpha\beta} \varepsilon_i^{\alpha\beta} \tag{5.49}$$

and

$$\frac{De_i}{Dt} = -\frac{1}{2}\sum_{j=1}^{N} m_j \frac{p_i + p_j}{\rho_i \rho_j} v_{ij}^{\beta} \frac{\partial W_{ij}}{\partial x_i^{\beta}} + \frac{\mu_i}{2\rho_i} \varepsilon_i^{\alpha\beta} \varepsilon_i^{\alpha\beta} \tag{5.50}$$

5.2.4.4 Particle approximation of energy

The mass fraction of a certain component is denoted by *C*, so that the mass of the component in a mass *M* of liquid is *CM*. The diffusion of the component is given by the following equation:

$$\frac{DC}{Dt} = \frac{1}{\rho} \nabla \left(D \nabla C \right) \tag{5.51}$$

where *D* is the coefficient of diffusion. Because the diffusion equation involves second derivatives, it is necessary to choose an SPH form with care to avoid large errors. In addition, the form should ensure conserved matter for isolated systems and lead to an increase in the entropy of the system. A suitable form can be found by starting with the integral:

$$\frac{1}{\rho(r)} \int \left[k(r) + k(r') \right] \left[T(r) - T(r') \right] F(r - r', h) dr' \tag{5.52}$$

Where *dr*' is a volume element and *h* is a length scale. The function *F* is defined by

$$rF(r,h) = \nabla W(r,h) \tag{5.53}$$

The SPH method allows us to approximate volume integrals by summation over particles according to

$$\int A(r') dr' \approx \sum_j m_j \frac{A_j}{\rho_j} \tag{5.54}$$

If the rule is applied to the diffusion equation, take *r* to be the coordinate r_i of particle *i*, the SPH form of mass diffusion for any particle *i* becomes

$$D_i \frac{DC_i}{Dt} = \sum_j \frac{m_j}{\rho_i \rho_j} \left(D_i + D_j \right) \left(C_i - C_j \right) F_{ij} \tag{5.55}$$

F_{ij} denotes $F(r_{ij})$ with the notation $r_{ij} = r_i - r_j$. This form of the mass diffusion equation does not guarantee that the mass flux will be continuous when j is discontinuous. Cleary and Monaghan show from an analysis of the finite difference case that this problem can be solved by replacing $(D_i + D_j)$ by

$$\frac{4D_iD_j}{(D_i + D_j)} \tag{5.56}$$

Thus, the rate of change of the concentration of C_i of particle i is given by

$$\frac{DC_i}{Dt} = \sum_j \frac{m_j}{\rho_i \rho_j} \frac{4D_iD_j}{(D_i + D_j)} (C_i - C_j) F_{ij} \tag{5.57}$$

5.2.5 Boundary treatment

SPH method once suffered from the problem of particle deficiency near or on the boundary. For one particle located near or on the boundary, it has more neighbors inside the boundary than outside the boundary since there are less or no particles beyond the boundary, which will result in the asymmetry of field variables. One possible approach to fix this problem is to set virtual particles outside the boundary. Usually, two types of virtual particles are used to treat the solid boundary condition. The type I virtual particles are located right on the boundary, which can produce enough repulsive for and thus prevent the real particles from penetrating though the boundary. The type II virtual particles are filled in the boundary region as ghost particles and reflect a symmetrical surface boundary condition.

The interaction between the type I virtual particle and real particle can be chosen to be Lennard-Jones form

$$PB_{ij} = \begin{cases} D\left[\left(\frac{r_0}{r_{ij}}\right)^{n_1} - \left(\frac{r_0}{r_{ij}}\right)^{n_2}\right] & r_0/r_{ij} \le 1 \\ 0 & r_0/r_{ij} > 1 \end{cases} \tag{5.58}$$

where the parameters n_1 and n_2 are usually 12 and 4, respectively. D depends on the specific problems, the cutoff distance r_0 is usually selected close to the initial particle spacing.

For the flow with low Reynolds number, no-slip boundary condition on the wall or solid particle surface is needed. Libersky *et al.* [114-116] proposed a general treatment for the straight channels by assigning the same field variables to all the ghost particles but with opposite velocities. For a curved surface, Morris *et al*. [117] addressed a novel approach to achieve no-slip boundary condition. For the fluid particle *a*, normal distance, d_a, to the boundary is calculated. The tangent line is defined as well. The normal distance d_B is also calculated. The velocity $\vec{u}_B$ is expressed as:

$$\vec{u}_B = -\frac{d_B}{d_a}\vec{u}_a \tag{5.59}$$

If the boundary is in motion, $\vec{u}_a$ will be the fluid velocity relative to the boundary. If a fluid particle closely approaches a boundary surface during simulation, potentially large artificial velocity for boundary particles may occur. To avoid this problem, the following expression is applied to calculate the relative velocity between fluid and boundary particles

$$\vec{u}_{ab} = \beta\vec{u}_a \tag{5.60}$$

where $\beta = \min(\beta_{\max}, 1+\frac{d_B}{d_a})$ and $\beta_{\max}$ is around 1.5.

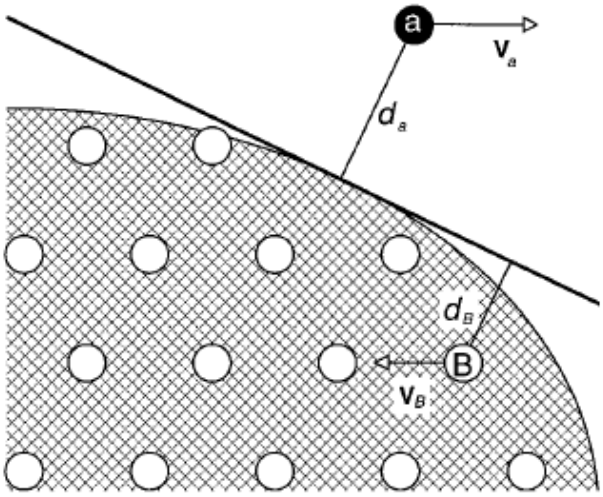

Figure 7 Artificial velocity for boundary particles to simulate a no-slip boundary condition

5.2.6 Time integration

Many approaches such as the second order accurate Leap-Frog (LF), predictor-corrector, Runge-Kutta (RK) schemes can be employed to integrate the discrete SPH equations.

Explicit time integration is performed using the predictor-corrector method with the time step, Δt, limited by stability constraints. Courant-Friedrichs-Levy (CFL) condition needs to be satisfied. CFL condition states that in a numerical simulation, the computational domain of dependence should include the physical domain of dependence, or the maximum speed of numerical propagation must exceed the maximum speed of physical propagation. This CFL condition requires the time step to be proportional to the smallest spatial particle resolution, which is represented by the smallest smoothing length in SPH applications. When taking into account the viscous dissipation and the external force, two expressions were given by Monaghan

$$\Delta t_{cv} = \min\left(\frac{h_i}{c_i + 0.6\left(\alpha_\Pi c_i + \beta_\Pi \max\left(\phi_{ij}\right)\right)}\right) \tag{5.61}$$

$$\Delta t_f = \min\left(\frac{h_i}{f_i}\right)^{\frac{1}{2}} \tag{5.62}$$

Combining equations (5.61) and (5.62) together with two corresponding safety coefficients λ_1 and λ_2, the typical time step is calculated using

$$\Delta t = \min\left(\lambda_1 \Delta t_{cv}, \lambda_2 \Delta t_f\right) \tag{5.63}$$

Monaghan suggested that λ_1 =0.4 and λ_2=0.25.

Another expression of time step estimation is also given by Monaghan when considering viscous diffusion:

$$\Delta t = 0.125 \frac{h^2}{\nu} \tag{5.64}$$

where $\nu = \mu / \rho$ is kinetic viscosity.

Chapter Six

Multiphase Flow with Solidification – Application I Crystal Growth by Bridgman Technique

In this chapter, we studied the Bridgman crystal growth of six semiconductor materials, such as InAs, InSb, GaSe, CdTe, PbTe and GaP. By comparing the difference of thermophysical properties and dimensionless parameters, we categorized the materials into different groups and thus established a process map based on Prandtl and Grashof numbers to enable the optimal growth conditions. Melt flow and heat transfer behaviors are similar for the same group. Numerical simulations are then performed to show the velocity and temperature fields in the same growth system and at the same operating conditions. The interface shapes are also plotted and compared. A new growth system is also designed, which is capable of reducing melt convection when the melt flow is too strong. The capability of the proposed design is demonstrated. By changing the design parameters, the strength of melt flow can be manipulated. From numerical simulation, it seems that the proposed design is suitable for growing large diameter crystals.

6.1 Single Crystal Growth by Bridgman Technique

6.1.1 Mechanism of single crystal growth by Bridgman technique

Figure 8(a) presents the schematic of vertical Bridgman furnace, and Figure 8(b) depicts the temperature profile applied to the furnace. Bridgman growth system is mainly composed of high temperature zone where the melt is loaded, a low temperature zone where the as grown crystal is located, an adiabatic zone where a suitable temperature

gradient is established, and an ampoule, which holds the feedstock. Bridgman technique is characterized by the relative translation between crucible and furnace, and Bridgman growth method is basically a controlled freezing process taking place under liquid - solid equilibrium conditions. Directional solidification takes place because of the axial temperature gradient in the furnace, and the mechanism is to produce a single nucleus from which a single crystal will propagate and grow. This is achieved simply by applying the translation to lower the crucible through the axial temperature field of the furnace. Another way is to hold the crucible stationary and translate the furnace a linear track assembly. The translation speed is rather slow (5-50 mm/day) until the whole molten charge is solidified.

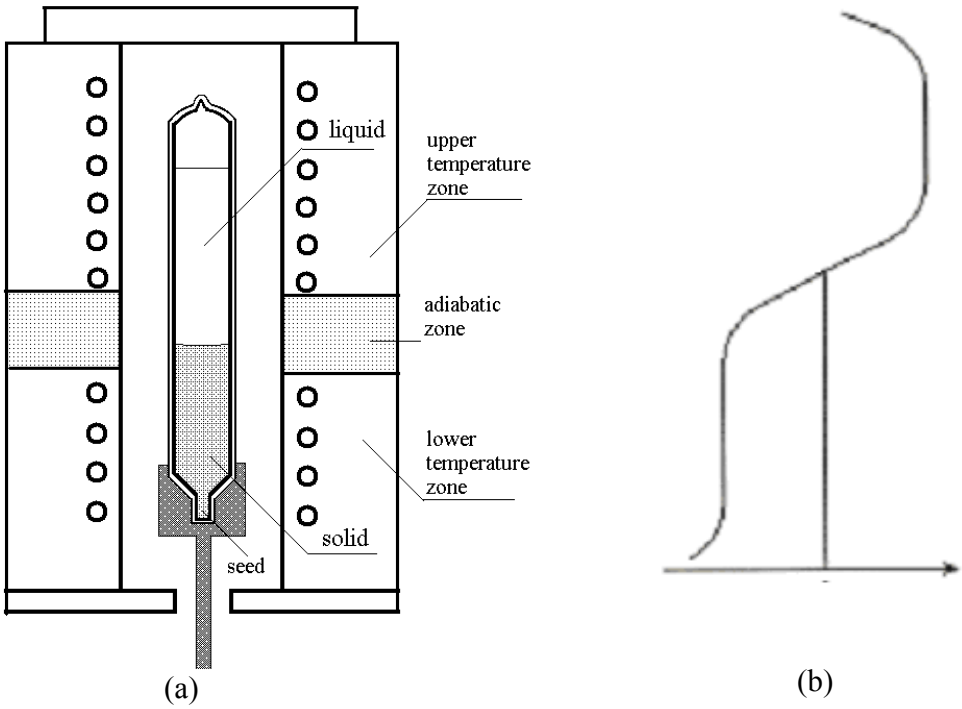

Figure 8(a) Schematic of vertical Bridgman system, (b) temperature profile applied to the furnace

6.1.2 Simulation domain and computational scheme

Our research focuses on the velocity field, temperature distribution and interface shape in the central part of Bridgman system, which includes melt/solid and crucible. Figure 9(a) shows the schematic of crucible in a traditional Bridgman system. It consists

of hot, cold and adiabatic zones with the heights of H_h, H_c and H_{ad}, respectively. Crystal diameter (ampoule's inner diameter) is D_{cry}, ampoule wall thickness is δ_{amp} and the gap between ampoule and furnace is δ_{gap}. The feedstock is first loaded into the ampoule and heated to the temperature above the melting temperature. After stabilization, the furnace (or ampoule) is then moved downward (or upward) and molten melt is solidified. T_h, T_c and T_M represent temperatures at the hot and cold zones and at melting point.

A state-of-the-art computer model, *MASTRAPP* (Multizone Adaptive Scheme for TRAnsport and Phase-change Processes) is used for numerical simulations. The model solves governing equations of mass, momentum, and energy to predict the melt flow pattern and heat transfer in a crystal growth system. The numerical scheme is capable of capturing the interface shape and location efficiently since the solid/melt interface is tracked explicitly using the multizone adaptive grid generation scheme. The entire equations are solved using curvilinear finite volume approach together with adaptive grids so that sufficient fine grids can be guaranteed near the growth interface [118-123]. Numerical simulations have been performed for Bridgman crystal growth of different materials. The grids are shown in Figure 9(b) and flow chart is presented in Figure 10.

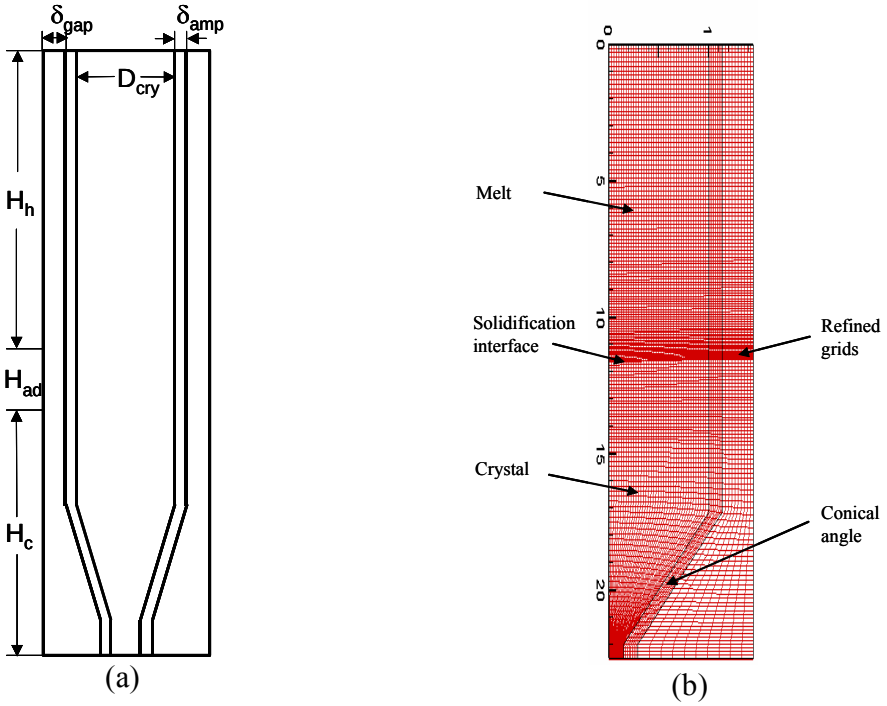

Figure 9(a) Schematic of simulation domain and (b) computational grids

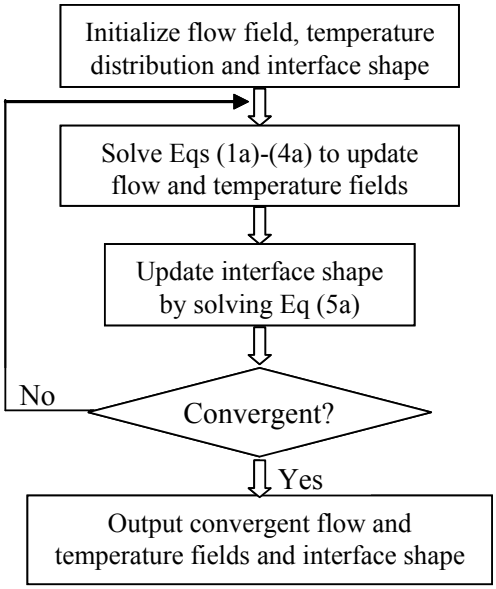

Figure 10 Flow chart for the numerical scheme

6.2 Numerical Model

6.2.1 Governing equations

To simulate the velocity field and temperature distribution during uni-directional solidification, the following assumptions are made: (i) Melt flow is incompressible, laminar, and axisymmetric; (ii) Melt is the Newtonian fluid; (iii) Thermo-physical properties are assumed to be constant at the given phases. With the above assumptions, the governing equations can be written as follows:

For the melt:

Continuity equation: $$\nabla \cdot (\rho_l \vec{u}) = 0 \tag{6.1}$$

Momentum equation: $$\frac{\partial}{\partial t}(\rho_l \vec{u}) + \nabla \cdot (\rho_l \vec{u}\vec{u}) = -\nabla p + \mu_l \nabla^2 \vec{u} + \rho_l \vec{g} \tag{6.2}$$

Energy equation: $$\frac{\partial}{\partial t}(\rho_l C_{pl} T) + \nabla \cdot (\rho_l C_{pl} T \vec{u}) = \nabla \cdot (k_l \nabla T) + S \tag{6.3}$$

For the solid (crystal and ampoule):

Energy equation: $$\frac{\partial}{\partial t}(\rho_s C_{ps} T) = \nabla \cdot (k_s \nabla T) \tag{6.4}$$

At the solidification interface

Energy balance: $$-\kappa_s \left.\frac{\partial T}{\partial n}\right|_s + \kappa_l \left.\frac{\partial T}{\partial n}\right|_l = \rho_l \Delta H_f u_n \tag{6.5}$$

where ρ, C_p and κ are the density, specific heat capacity and thermal conductivity, respectively, ΔH_f is the latent heat; S is the heat source term. The subscripts s, l, and n represent solid, liquid and direction normal to the interface, respectively.

6.2.2 Thermophysical properties and dimensionless parameters

Thermophysical properties of GaSe, InSb, InAs, CdTe, PbTe and GaP crystals are summarized in Table 1. In the system being studied, melt motion is primarily due to buoyancy convection. In order to find the role of the control parameters, the governing equations (2.1) to (2.5) are non-dimensionalized. The reference scales include the length scale by the inner radius of ampoule, b, velocity scale by the ratio of kinematic viscosity, ν_l, to reference length scale, and the temperature scale (ΔT) by temperature difference between high temperature T_h and melting temperature T_m. The governing equations (2.1) to (2.5) is non-dimensionalized using the non-dimensional parameters, $x' = x/b$, $y' = y/b$, $u' = ub/\nu_l$, $t' = t\nu_l/b^2$, $p' = \left(p - \rho_l g x\right)/\left(\rho \nu_l^2/b^2\right)$, $\theta = \left(T - T_M\right)/\Delta T$, and $k' = k/k_l$. The dimensionless forms of the governing equations can then be written as follows,

$$\nabla \cdot \vec{u'} = 0 \tag{6.1a}$$

$$\frac{\partial \vec{u'}}{\partial t'} + \nabla \cdot \left(\vec{u'}\vec{u'}\right) = -\nabla p' + \nabla^2 \vec{u'} - Gr\,\theta \vec{i}_g \tag{6.2a}$$

$$\frac{\partial \theta}{\partial t'} + \nabla \cdot \left(\theta \vec{u'}\right) = \frac{1}{\mathrm{Pr}} \nabla^2 \theta + S' \tag{6.3a}$$

$$\frac{\partial}{\partial t'}(\rho_s' C_{ps}' \theta) = \frac{1}{\mathrm{Pr}} \nabla \cdot \left(k_s' \nabla \theta\right) \tag{6.4a}$$

$$-\frac{\kappa_s}{\kappa_l}\frac{\partial \theta}{\partial n}\bigg|_s + \frac{\partial \theta}{\partial n}\bigg|_l = \frac{\mathrm{Pr}}{Ste} u_n' \tag{6.5a}$$

The dimensionless parameters include the Grashof number, $Gr = \beta \Delta T g b^3/\nu_l^2$, the Prandtl number, $\mathrm{Pr} = \nu_l/\alpha_l$, and the Stefan number, $Ste = C_{pl}\Delta T/\Delta H_f$. The important control parameters are the Grashof number $Gr = \beta \Delta T g b^3/\nu_l^2$, the Prandtl number $\mathrm{Pr} = \nu_l/\alpha_l$, and the Stefan number $Ste = C_{pl}\Delta T/\Delta H_f$. Other interface and boundary conditions at this geometry will be straightforward, which will be listed here. After non-dimensionless, a new dimensionless number, the Biot number, $Bi = hb/k_s$, will be appeared. The Grashof

number is one of the most important parameters in melt flow, which represents the strength of melt convection driven by natural convection. The Prandtl number is another important parameter representing the coupling between fluid and thermal transport and it indicates the influence of melt convection on temperature distribution. In convective heat transfer, the influence of melt flow on heat transfer is sometimes determined by the Rayleigh number, Ra=Gr*Pr. The Stefan number is strongly related with the latent heat releasing, consequently, related to the shape and movement of the solidification interface. The Biot number can be used to describe the temperature difference between the center and the edge, which is related to the shape of the solidification interface. For a very small Biot number, temperature in the crystal is uniform in the radial direction. Almost flat interface can be obtained if the melt flow is not very strong. In additional to the dimensionless parameters, the ratios of the thermal conductivity between the crystal, melt and ampoule play the very important role on the solidification interface shape. Table * summarizes the different dimensionless parameters mentioned above for six materials.

Table 1 Thermophysical Properties of GaSe, InSb, InAs, CdTe, PbTe and GaP

Property	**GaSe**	**InSb**	**InAs**
Melting point, T_M, K	1210 [124]	800 [125]	1215 [125]
Enthalpy of fusion, ΔH_f, J/kg	376.65×10^3 [124]	101.0×10^3 [126]	405.74×10^3
Thermal expansion coefficient, β, /^{0}C	1.287×10^{-4} [124]	1.0×10^{-4} [125]	4.07×10^{-5} [127]
Density, ρ, kg/m^3			
Melt	4814 [124]	6480 [125]	5890 [125]
Crystal	4930 [124]	5760 [125]	5500 [125]
Thermal conductivity, κ, W/m K			
Melt	$-3.168+3.243\times10^{-3}T$ [124]	$5.289+1.573\times10^{-2}$ T [128]	
Liquid melting point	0.756 [124]	17.873 (calculated from [128])	13.692
Crystal along c axis	$609\times T^{-1.045}$ [124]	$1826\times T^{-0.826}$ [129]	$10941\times T^{-1.070}$ [129]
Solid melting point	0.366 [124]	7.30 (calculated from [129])	5.477 [129]
Crystal ⊥ c axis	$5558\times T^{-1.063}$ [124]		
Solid melting point	2.937 [124]		
Specific heat, C_p, J/kg K			
Melt	560 [124]	280 [125]	297.6
Crystal	340 [124]	238 [125]	$240+3.97\times10^{-2}$ T [13]
			288 [13]
Kinematic viscosity, ν, m^2/s			
Melt	4.0237×10^{-8}	2.8535×10^{-8}	1.5254×10^{-8}
Liquid melting point	exp(3558.64/*T*) [124]	exp(2089.74/T) [125]	exp(2882.61/*T*) [125]
	7.81×10^{-7} [124]	3.70×10^{-7} [125]	1.75×10^{-7} [125]
Dynamic viscosity, μ, kg/m s			
Liquid melting point	3.76×10^{-3} [124]	2.400×10^{-3} [125]	1.025×10^{-3} [125]
Thermal diffusivity, α, m^2/s			
in the melt	2.80×10^{-7} [124]	9.85×10^{-6} [125]	7.81×10^{-6} (calculated from definition)

(continued)

Property	CdTe	PbTe	GaP
Melting point, T_M, K	1365 [128]	1190 [14]	1730 [14]
Enthalpy of fusion, ΔH_f, J/kg	209.20×10^3 [18]	342.29×10^3 [19]	706.06×10^3 [130]
Thermal expansion coefficient, β, /^{0}C	5.0×10^{-4} [3]	2.13×10^{-4} [14]	4.65×10^{-4} [14]
Density, ρ, kg/m^3			
Melt	5640 [19]	7450 [14]	4562 [14]
Crystal	6200 [19]	8160 [14]	4138 [14]
Thermal conductivity, κ, W/m K			
Melt			
Liquid melting point	2.0 [128]	4.18 [14]	13.0 [132]
		$0.029\times T^{-0.66}$ [131]	
Crystal along c axis			
Solid melting point	1.0 [128]	3.11 [131]	5.2 [132]
Crystal ⊥ c axis			
Solid melting point			
Specific heat, C_p, J/kg K			
Melt	187 [18]	200 [133]	482 [14]
Crystal	160 [18]	165 [133]	430 [14]
Kinematic viscosity, ν, m^2/s			
Melt		$9.093\times10^{-9}\exp(3955.61/T)$ [14]	
Liquid melting point	8.0×10^{-7} [3]	6.790×10^{-7} [14]	4.5×10^{-7} [14]
Dynamic viscosity,μ, kg/m s			
Liquid melting point	4.51×10^{-3} [3]	5.059×10^{-3} [14]	2.05×10^{-3} [14]
Thermal diffusivity, α, m^2/s			
in the melt	1.89×10^{-6}	2.80×10^{-6} [14]	5.91×10^{-6} [14]

Table 2 Effects of Prandtl, Grashof, Stefan, Biot and Rayleigh numbers (based on 7 mm in radius and 75 degrees above melting temperature) on interface curvature

Material	InAs	GaP	InSb	PbTe	CdTe	GaSe
Prandtl number, Pr	0.022	0.03	0.038	0.24	0.42	2.78
Grashof number, Gr	3.35×10^5	5.8×10^5	1.85×10^5	1.16×10^5	2.0×10^5	5.32×10^4
Stefan number, Ste	0.055	0.051	0.21	0.044	0.067	0.11
Ste/Pr	2.5	1.7	2.76	0.18	0.156	0.04
Biot number, Bi	0.24	0.74	0.048	0.39	1.86	3.50
K_s/K_l	0.40	0.39	0.41	0.74	0.50	0.48
K_a/K_l	0.19	0.20	0.14	0.62	1.30	3.44
Rayleigh number, Ra	7.37×10^3	1.74×10^4	7.03×10^3	2.78×10^4	8.4×10^4	1.48×10^5
Interface curvature, δ	0.065	0.15	0.048	0.45	0.63	1.38

(note: ,K_s, K_l and K_a are the thermal conductivities of crystal, melt and ampoule, respectively. δ is the dimensionless height difference between points at centerline and inner ampoule wall in the interface)

6.3 Result and Discussions

6.3.1 Effect of the controlling parameters

To study the effects of material properties, the geometry and operating conditions are fixed. In this paper, we have selected 14mm diameter crystal, which is grown in EIC laboratory. The results obtained here can then be directly used to compare with the

experimental studies there. The hot zone temperature is assumed to be 75^{o}C higher than the melting temperature. Thermophysical properties of GaSe, InSb, InAs, CdTe, PbTe and GaP crystals are summarized in Table 1. The gap between the ampoule and the inner wall of the furnace is filled with gas at the high temperature. Radiation heat transfer between the outer surface of the ampoule and the inner surface of the furnace is very strong. An effective thermal conductivity is assigned to the gap considering radiation.

For the system considered in this study, melt motion is primarily due to the buoyancy convection and no rotation is considered in the ampoule. In the crystal growth, a slow rotation rate is usually applied, which is mainly for the uniformity of the heating. It will have minor influence on the melt flow by comparing the rotational Reynolds number and the Grashof number. The rotation is therefore not considered here. To analyze the key control parameters, the Grashof, Prandtl, Stefan, and Biot numbers are calculated in a 14 mm crystal diameter with reference temperature difference of ΔT = 75K for InAs, InSb, GaP, PbTe, CdTe and GaSe, respectively. Table 2 shows the calculation results. It is generally believed that, for a crystal with Prandtl smaller than 0.1 and Grashof number less than 10^5, the crystal can be grown successfully using a traditional Bridgman system. The melt flow pattern and temperature distribution are very similar. In fact, due to the small Prandtl number, the melt flow is not significantly affected by temperature distribution. On the other hand, the temperature distribution will be close to the conduction case. For a crystal with high Prandtl number and/or high Grashof numbers, melt flow, temperature field and growth interface are strongly coupled. To predict the solidification interface shape is not straightforward. For example, it is possible to change the growth interface shape from convex to concave shape by changing the growth rate.

Figure 11 shows the temperature variations along the centerline of the ampoule for six materials for pure conduction and convection cases. The difference between two profiles indicates the influence of melt convection on temperature distribution. The Prandtl number plays an important role to reflect such difference. When the Prandtl number is small, in the cases of InAs, GaP, and InSb. The effect of temperature field on the melt flow is minor. The results without and with convection are very similar. When the Prandtl number is large, in the case of PbTe, CdTe, and GaSe, the difference of

temperature profiles between the cases with and without convection becomes obvious, confirming a strong dependence of temperature on melt convection of large Prandtl number. Figure 12 presents the interface shapes of six materials. It is clearly shown that the interface shape becomes more curved when the Prandtl number is increased. In the case of melt flow, the Grashof number plays an important role. Melt convection becomes stronger when the Grashof number increases. The flow may change from laminar to turbulence. Since instability/perturbation in melt flow will distort the species distribution near the interface, which may cause local undercooling. It will therefore benefit to suppress such perturbation. At the same time, we have to maintain a certain temperature gradient in the melt near the interface so that a stable growth condition with relatively high growth rate can be maintained. To investigate the effects of Pr and Gr on crystal growth, a *Gr* - *Pr* graph (Figure 13) is drawn and divided into four regimes, based on the flow type (laminar, transition, turbulent) and Prandtl number regime. Regime I represents where melt flow is laminar and heat transfer is dominated by heat conduction ($Pr < 0.1$). Regime II is where melt flow is laminar, but melt flow will affect the temperature distribution significantly ($Pr > 0.1$). Regimes III and IV are where melt flow is either in transition or turbulent regime. Regime I is the favorable zone for crystal growth and other Regimes exhibit some unfavorable conditions for crystal growth, special measures are necessary.

The effects of Prandtl, Grashof and Stefan numbers on interface curvature are summarized in Table 2. The interface evolution is mathematically determined by dimensionless equation (5a). It is known that the interface curvature in a vertical Bridgman system is strongly influenced by the rate at which the latent heat can be transferred away from the interface through the crystal. This rate can be reflected from the dimensionless parameter Ste/Pr. It is easily seen that interface is more curved with the reduction of Ste/Pr. It is also found that as the Rayleigh number (Gr*Pr) increases, the interface shapes is more curved, which can be explained by the effect of strong convection on temperature distribution. The predicted temperature and velocity distributions are presented in Figure 14. Again, simulation results also show that for InAs and InSb growth, temperature distribution is controlled mainly by heat conduction, while melt convection has a minor influence on temperature distribution due to small Prandtl

number. Results also indicate that temperature distribution is strongly affected by the length of the adiabatic zone for the growth of high Prandtl number crystal, e.g., CdTe and GaSe.

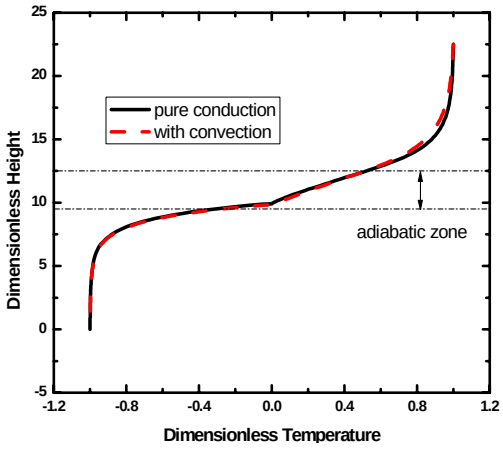

(a) InAs

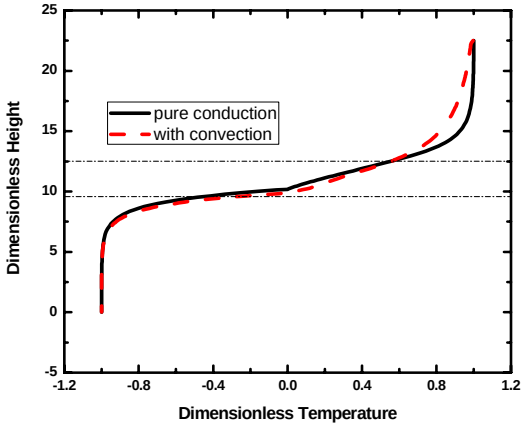

(b) GaP

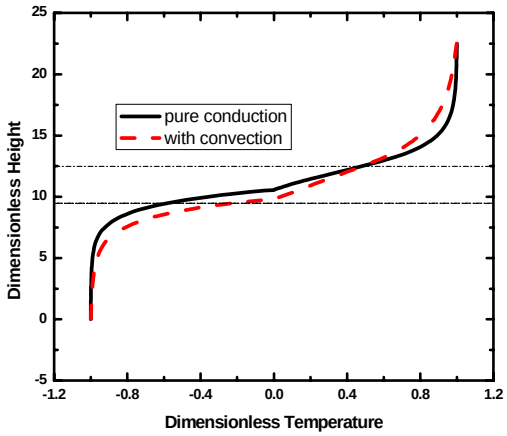

(c) InSb

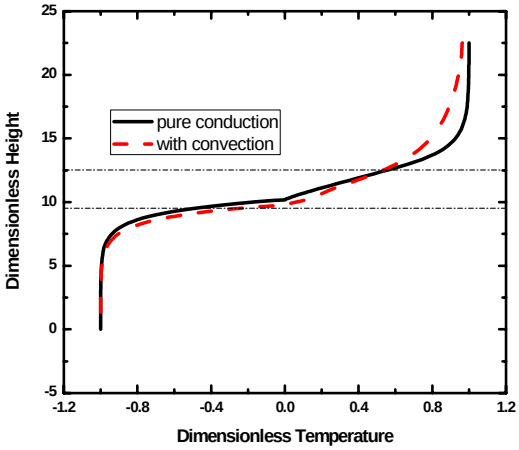

(d) PbTe

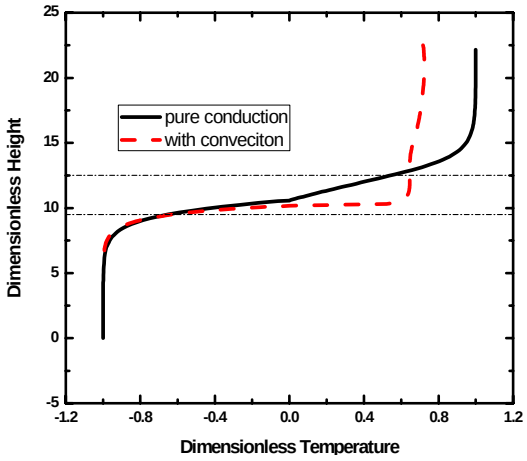

(e) CdTe

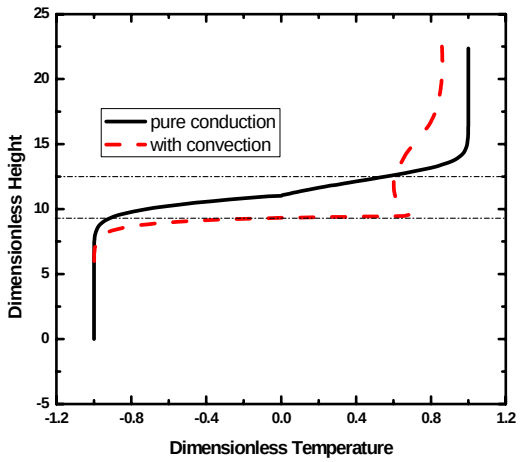

(f) GaSe

Figure 11 Temperature profile along centerline for 6 material with or without convection in the sequence of increase of Rayleigh number, (a) InAs, (b) InSb, (c) GaP, (d) PbTe, (e) CdTe and (f) GaSe.

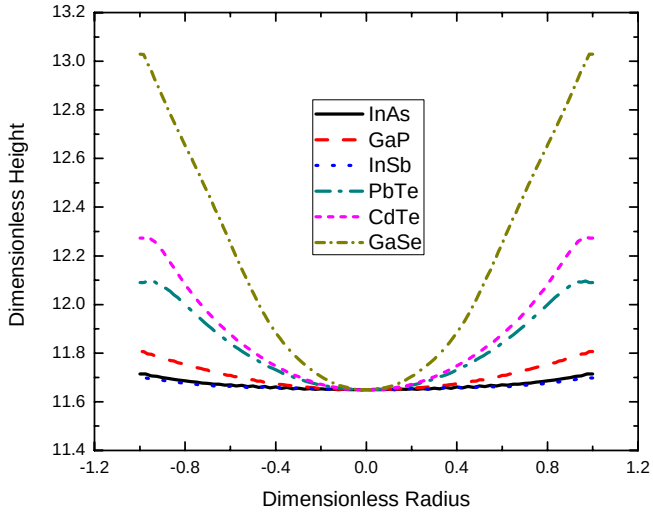

Figure 12 Solidification interface shapes for six materials

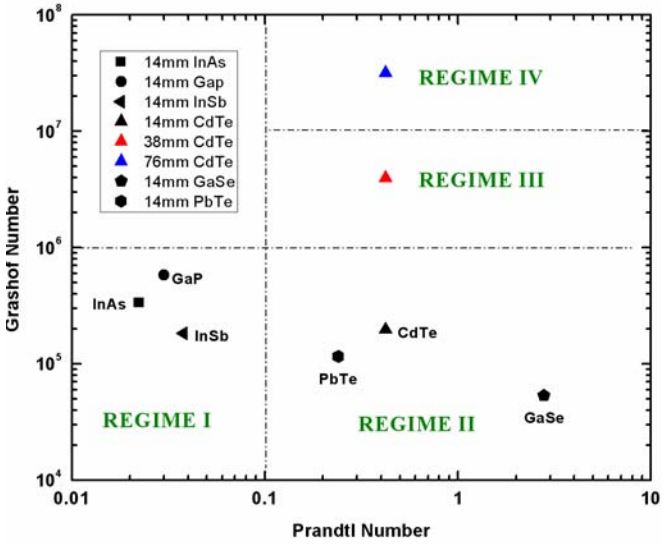

Figure 13 Symbols of square, circle, left-triangle, up-triangle, pentagon and hexagon represent InAs, GaP, InSb, CdTe GaSe and PbTe, respectively. The Grashof numbers are calculated with temperature difference between the hot temperature and melting point of 75 K. Black, red and blue colors represent CdTe crystal sizes of 14 mm (0.55 inch), 38 mm (1.5 inch) and 76 mm (3.0 inch), respectively.

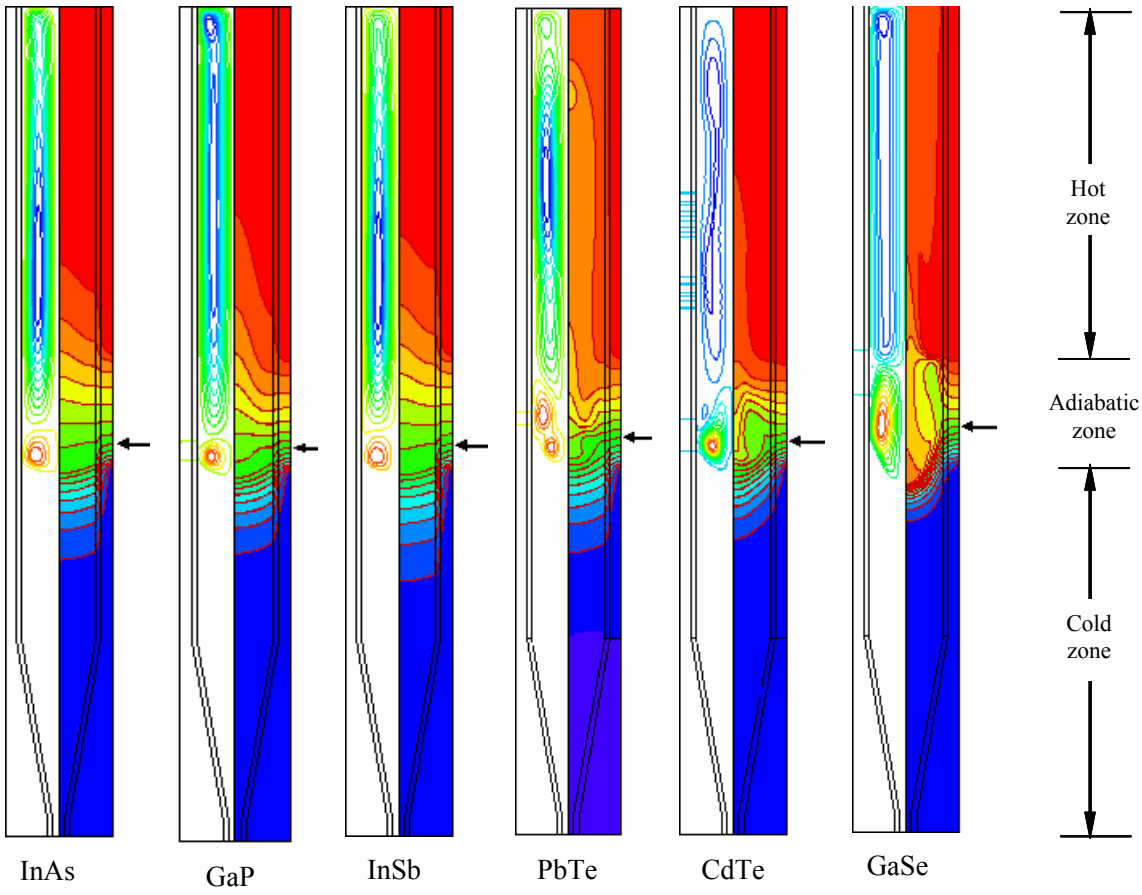

Figure 14 Temperature distributions and streamlines with enlarged views for the growth of CdTe at 14, 25.4, 38 mm in diameters.

6.3.2 Effect of crystal diameter on CdTe crystal growth

For CdTe crystal, three diameters are used to study the effect of crystal size on the strength of melt flow and solidification interface shape. As the diameter increases, the Grashof number increases while the Prandtl number is fixed. The Grashof number of the small crystal with 14 mm diameter is at the order of magnitude of 2.0×10^5, indicating laminar melt flow. By increasing crystal size to 25.4 mm, the Grashof number is increased to 1.18×10^6, which may be set in the oscillatory region. This Grashof number indicates that melt convection is intensified and strong melt flow may disturb the growth interface. If we increase the crystal size to 38 mm, the Grashof number reaches to 4.0×10^6, which is at the oscillatory region. It is anticipated that temperature distribution

and solidification interface will be influenced strongly by melt flow. It will be beneficial to reduce the melt flow and minimize the temperature fluctuation at the growth interface.

Figure 15 shows temperature distributions and streamlines for the growth of CdTe crystal of 14 mm, 25.4 mm and 38 mm in diameter in the enlarged view around the growth interface. Due to the relatively large Prandtl number, temperature distribution in the CdTe growth system is strongly influenced by melt flow, *i.e.* convection, causing unstable growth (interface) condition. Improvement on growth system design or suppressing melt convection is required to grow larger diameter crystals (>50mm).

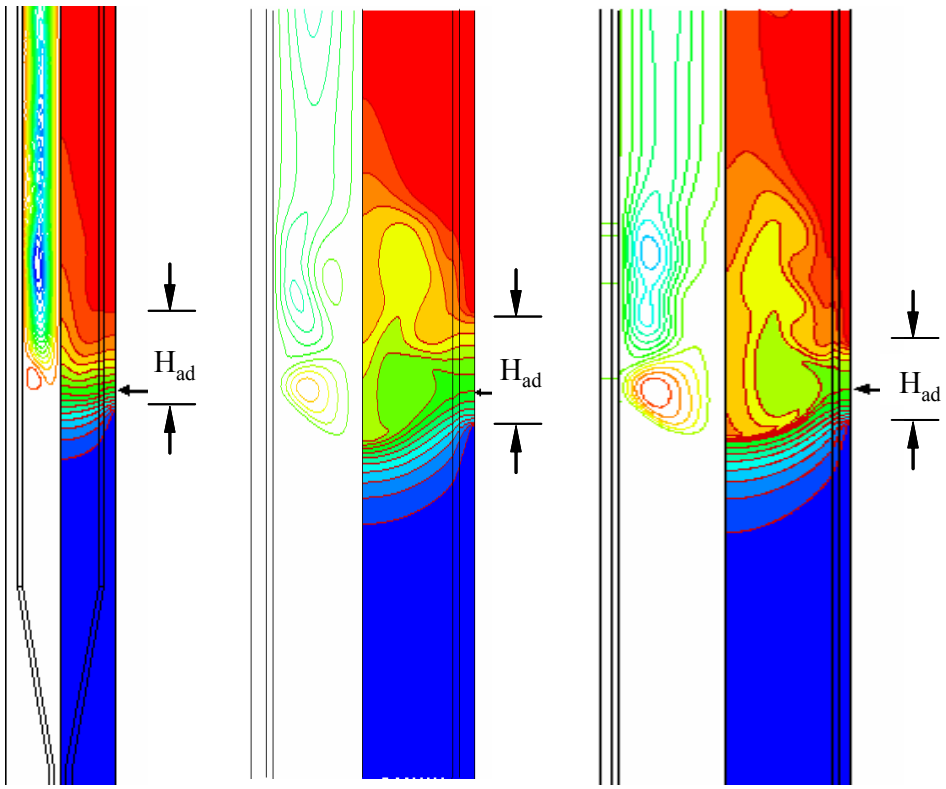

(a) 14mm (b) 25.4mm (c) 38 mm

Figure 15 Temperature distributions and streamlines with enlarged views for the growth of CdTe at 14, 25.4, 38 mm in diameters.

6.4 Proposed Growth System

As stated in the introduction part of Chapter One, many approaches can be applied to optimize the growth conditions, including the following skills: accelerated crucible rotation, ampoule tilting, submerged baffle and heater, submerged vibrator, alternating

magnetic fields, and so on. However, to change the temperature profile applied to the furnace, system geometry and thermal-physical properties of some key components seems to be the easiest to fulfill the optimization.

6.4.1 Optimization of temperature profile and furnace geometry

As concluded in the previous section, the hot zone temperature boundary condition is important for melt flow. A new design is proposed as shown in Figure 16(b). The modified Bridgman system consists of two hot zones heated with the heights of H_t (hot zone 1) and H_h (hot zone 2), together with transition, adiabatic and cold zones with the heights of H_{tr}, H_{ad} and H_c. The ampoule that holds the crystal has the thickness of δ_{amp} and the gap between the ampoule's external wall and the furnace inner surface is δ_{gap}. The hot zone 1 has the temperature slightly above the melting point to ensure no freezing on the wall and hot zone 2 will have a high temperature for establishing a certain temperature gradient to facilitate growth together with the given cold zone temperature. In this part, we will model the InSb crystal growth in the proposed furnace and investigate whether two-hot zone design can suppress melt convection. It is worthy noted that InSb is selected to illustrate the ideas. It is expected the geometric parameters such as H_{tr}, H_h and H_{ad} will determine the level of the melt flow suppression. To investigate the effects of geometry size of different zones in this new design, parametric study is performed. Note that people will think that flow will be unstable if hot melt is sitting at the bottom. In this case, it is a tall liquid column with lower sidewall temperature. The hot melt cannot penetrate into the lower temperature region very deep. The flow is therefore limited in the second hot zone. Simulation results show that the flow is weak and melt flow is stable.

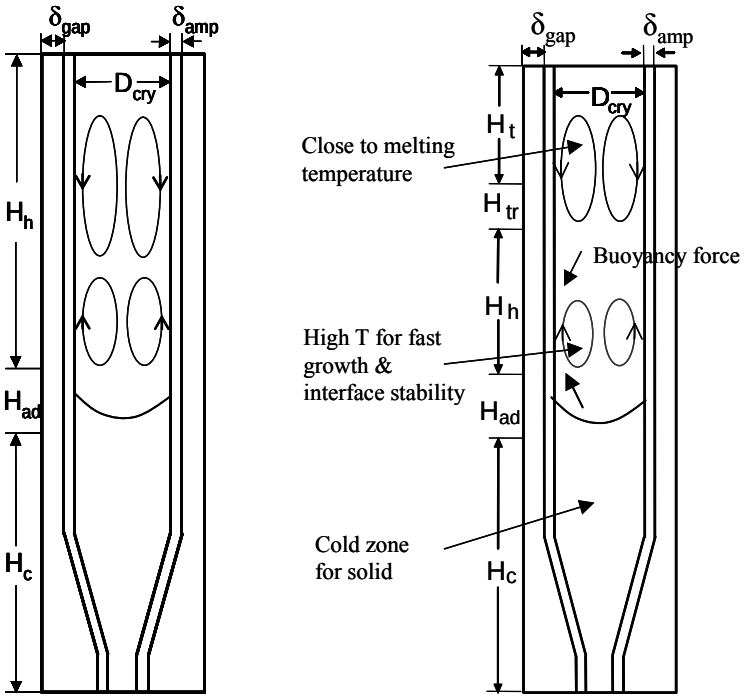

(a) Traditional design (b) New design

Figure 16 Schematic and comparison of (a) traditional Vertical Bridgman system and (b) proposed new design

To study the effect of hot zone length H_2 on melt flow, three cases are completed with different hot zone length H_h and $H_{tr}/D_{cry}=0.5$ and $H_{ad}/D_{cry}=1$. Temperature distributions and stream function distribution are presented in Figure 17 for hot zone sizes of H_h/D_{cry} = 5, 2, and 1 with D_{cry}= 38 mm in InSb growth. When the length of hot zone is small (H_h/D_{cry} = 1), weak melt convection and more flat solidification interface are predicted, indicating stable growth condition. When H_h/D_{cry} = 5 is appplied, strong convection is predicted. The temperature profile has varied significantly as the length of hot zone changes. It is noted that traditional Bridgman system has the H_h/D_{cry} value much larger than 5. Figure 18 shows the temperature profiles along the centerline when H_h/D_{cry} =5, 2 and 1, respectively. From the results, the growth interface is close to the bottom edge of adiabatic zone. It is because melt convection will push the solidification interface moves downward.

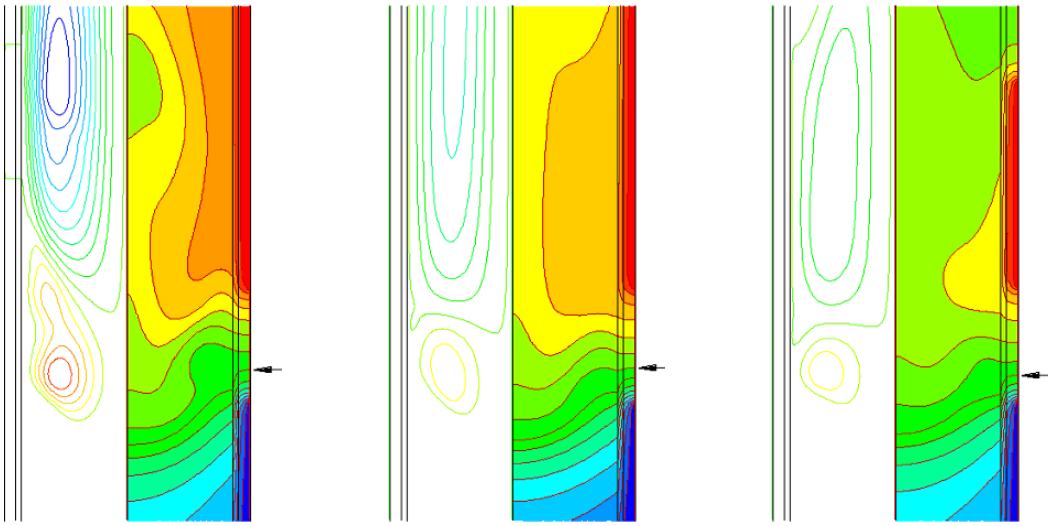

H_h/D_{cry}=5 H_h/D_{cry}=2 H_h/D_{cry}=1

Figure 17 Streamlines and isotherms for 38mm InSb with Grashof number of 3.2×10^6 for three cases with different H_h. Ψ_{min}=-192.5 (upper vortex),Ψ_{max}=104.9 (lower vortex); The black arrow indicates the location of solidification interface, the interval is 10K.

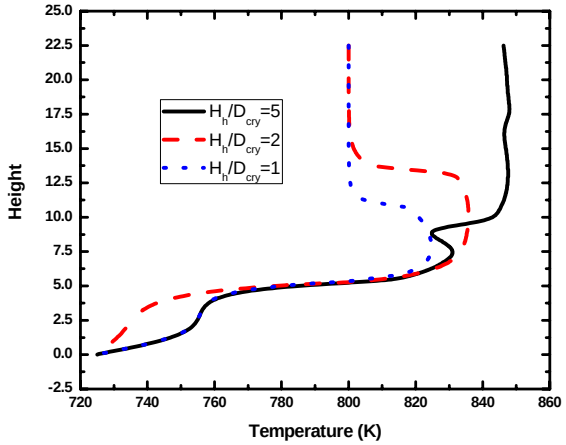

Figure 18 Temperature profile along centerline of a 38mm InSb ingot with different H_h

To investigate the effect of transition zone length H_{tr}, different cases are performed. The baseline case has the following geometry size: H_h/D_{cry} = 1, H_{tr}/D_{cry}=*0.5* and H_{ad}/D_{cry}=*1*. The lengths of H_2 and H_{ad} are fixed, while H_{tr} changes. Figure 19 indicates the temperature distribution and streamline for different sizes of H_{tr}/D_{cry}=*0.5, 1,* and *2.5*. As H_{tr} increases, temperature distribution and streamline change slightly. Figure 20 presents the temperature profile along the centerline of crystal. The profiles in the solid are almost the same, and meanwhile the ones in the melt just shift a little bit. It can

be concluded that the size change of H_{tr} has minor influence on temperature and velocity distribution when the lengths of H_2 and H_{ad} are fixed.

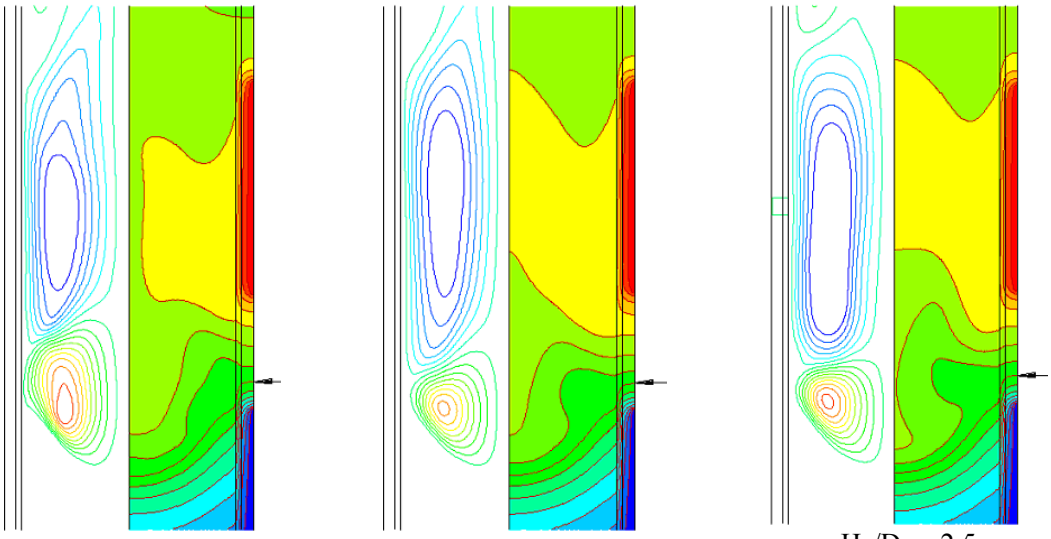

H_{tr}/D_{cry}=0.5 H_{tr}/D_{cry}=1.0 H_{tr}/D_{cry}=2.5

Figure 19 Streamlines and isotherms of 38mm InSb for three cases with different H_{tr}. Ψ_{min}=-54.3 (upper vortex), Ψ_{max}=83.0 (lower vortex); The black arrow indicates the location of solidification interface, the interval is 10K.

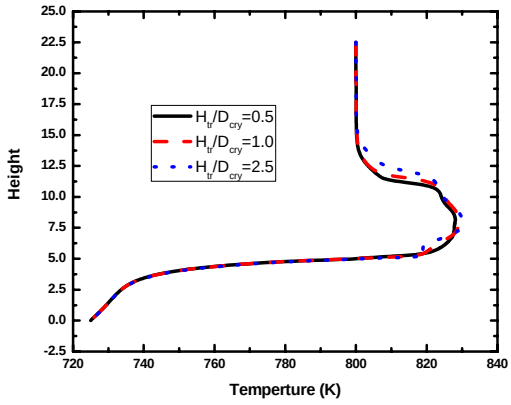

Figure 20 Temperature profile along centerline of a 38mm with different H_{tr}

The effect of adiabatic zone length H_{ad}, different cases are also completed. The baseline case has the following geometry size: H_h/D_{cry} = 1, H_{tr}/D_{cry}=*0.5* and H_{ad}/D_{cry}=*1*.

The lengths of H_2 and H_{tr} are fixed, and H_{ad} varies. Figure 21 indicates the temperature distribution and streamline for different sizes of H_{ad}/D_{cry}=*1, 2,* and *0.5*. Figure 22 presents the temperature profile along the centerline of crystal. It is shown that when the length of adiabatic zone is doubled, melt convection becomes much weaker. While the adiabatic zone length is cut to half of the original size, temperature distribution and streamline don't seem to change too much. It is quite surprised. Since the adiabatic length considers to be important to temperature gradient in the melt. In fact, it is used to estimate the temperature gradient. A short adiabatic length means a high temperature gradient in the melt. In the conduction case when the Grashof number is small. It will be true that the length of the adiabatic region determines the temperature gradient since almost linear temperature profile is expected from the growth interface to the hot zone. However, when the melt convection is strong, the temperature gradient in the melt is mainly determined by the thermal boundary layer of the melt flow. The thickness of the boundary layer depends on the Grashof number and interface curvature. It seems that the length of adiabatic region plays a minor role in the growth process when it is short. Of course, when the length of adiabatic region is very long, the temperature gradient will be reduced and melt convection is weakened.

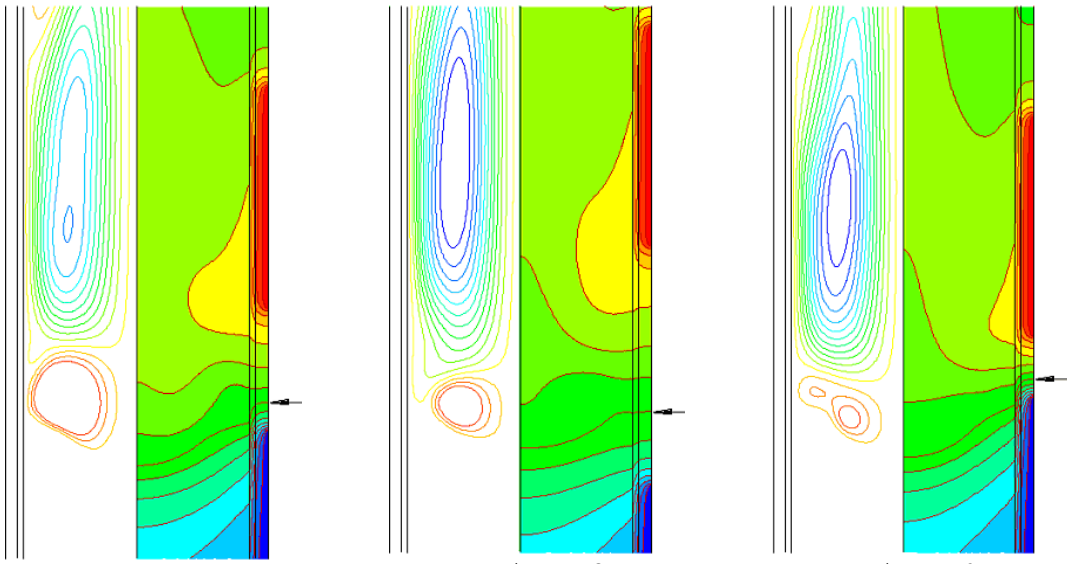

H_{ad}/D_{cry}=1 H_{ad}/D_{cry} =2 H_{ad}/D_{cry} =0.5

Figure 21 Streamlines and isotherms of 38mm InSb for three cases with different H_{ad}. Ψ_{min}=-76.1 (upper vortex), Ψ_{max}=17.6 (lower vortex); The black arrow indicates the location of solidification interface, the interval is 10K.

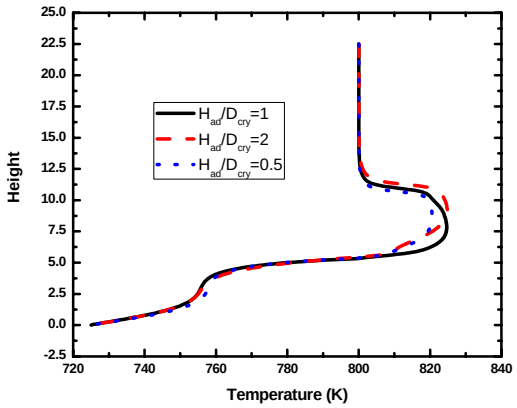

Figure 22 Temperature profile along centerline with different H_{ad}

6.4.2 Optimization of thermal-physical properties of ampoule

For the single crystal growth of GaSe, it is worthy to be noted that the thermal conductivity of melt or solid is relatively low compared with other II-VI or III-V compounds. The main disvatigate of low thermal conductivity is the difficulty of heat release from the solid and large temperature gradient in radial direction, resulting in strongly curved interface shape. Consequently a scheme is proposed to flatter the interface by reducing the thermal conductivity of ampoule. This part presents the numerical simulation of GaSe crystal growth with diameter of 2.5 inch (63.5 cm). In this case, the new design mentioned above is applied in the simulation. Temperature difference between adiabatic and cold zone is kept 75K.

Figure 23 shows the temperature distribution and velocity field and Figure 24 presents the temperature profiles along the centerline of ampoule when H_2/D_{cry} =5, 2 and 1, respectively. It is found that when the length of hot zone is increased, temperature profile becomes more curved, which indicates the significant effect of melt convection on temperature distribution. Figure 25 shows the interface shapes, which are less curved when the length of hot zone is reduced. From Table 1, it can be seen that thermal conductivity of ampoule, k_a, is much larger than those of GaSe in both melt and solid. It results in that heat flux is mainly flown from the melt to the ampoule rather than to the solid, which can cause a curved interface. To make the interface less curved, a design by reducing thermal conductivity of ampoule is proposed, where $k_a=0.6$ is used. In practice,

reduction of thermal conductivity of the ampoule can be achieved by coating in the inner wall of the ampoule. The validation of this scheme is performed. Figure 26 compares the interface shapes for all cases with normal and smaller thermal conductivities of ampoule. It can be concluded that the reduction of the thermal conductivity of the ampoule can flatter the interface, which favors the crystal growth.

.
.

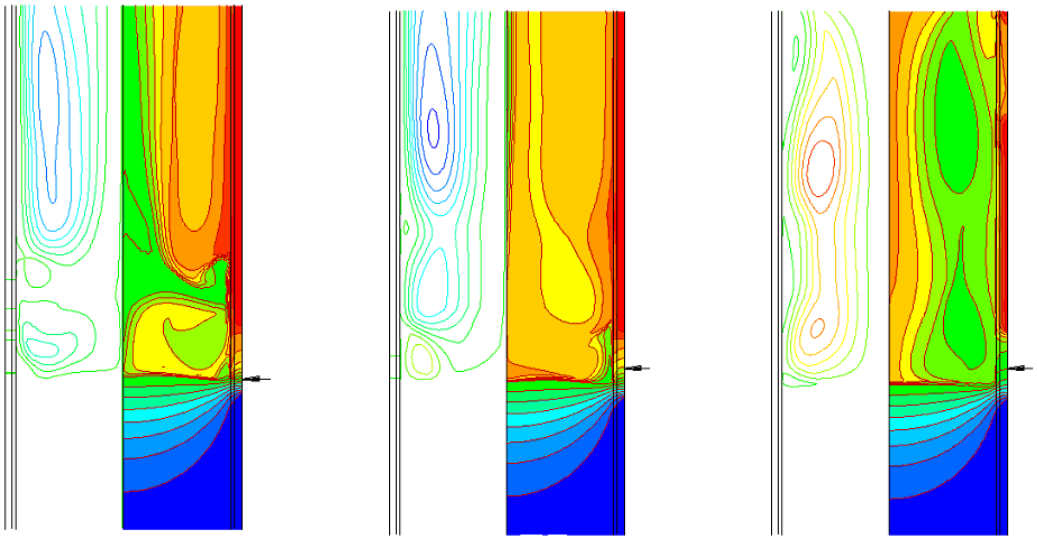

(a) $H_h/D_{cry}=5$ (b) $H_h/D_{cry}=2$ (c) $H_h/D_{cry}=1$

Figure 23 Streamlines and isotherms of 2.5inch GaSe for three cases with different H_h. Ψ_{min}=-283.3 (upper vortex), Ψ_{max}=211.2 (lower vortex); The black arrow indicates the location of solidification interface, the interval is 10K. And the thermal conductivity of ampoule is normal.

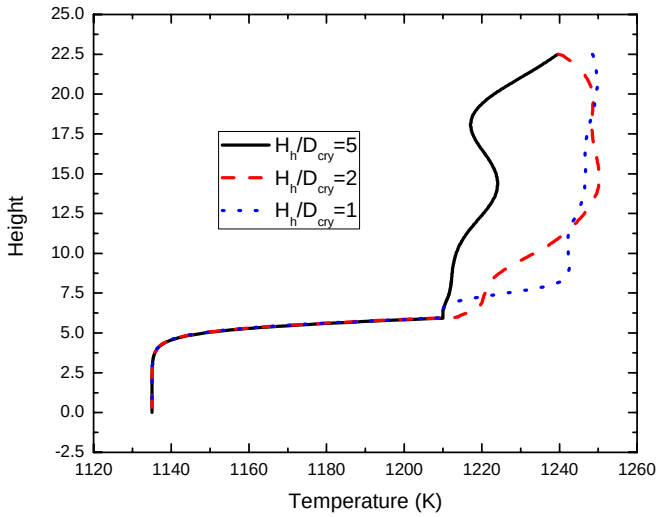

Figure 24 Temperature profiles along the centerline of the ampoule

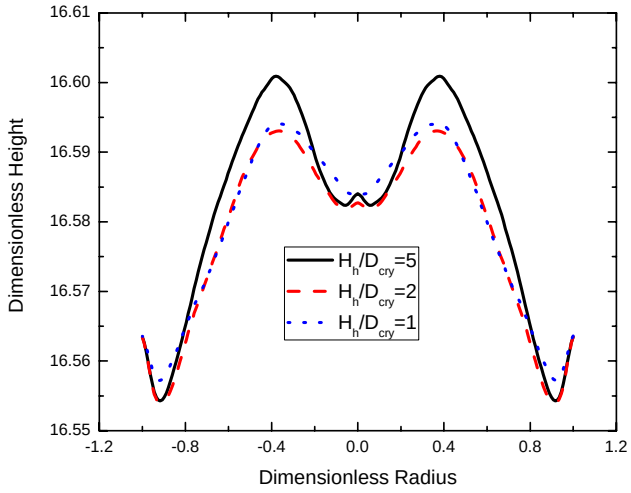

Figure 25 Interface shapes for three cases when H_h/D_{cry}=*5, 2, 1*, respectively for 2.5 inch GaSe growth

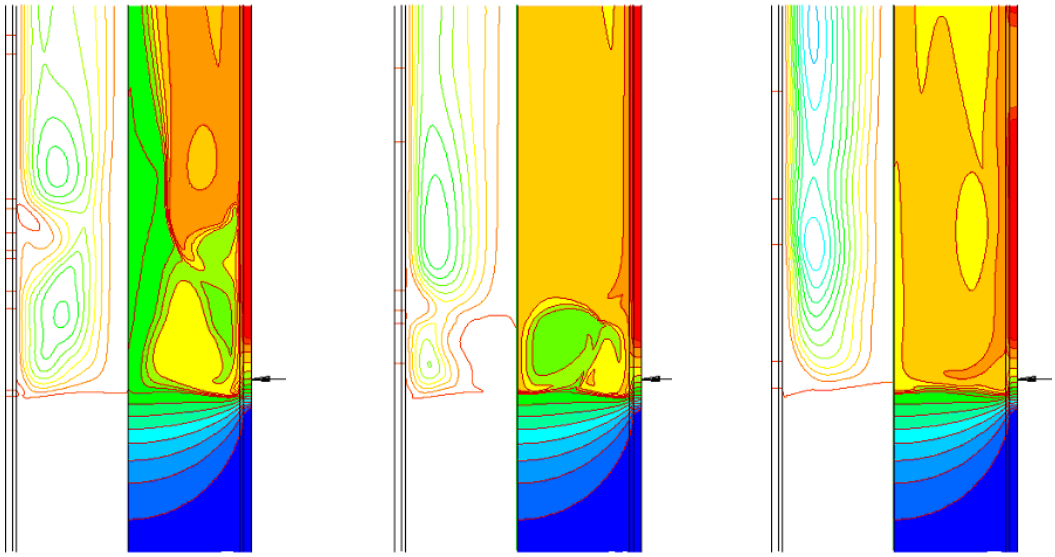

(a) $H_h/D_{cry}=5$ (b) $H_h/D_{cry}=2$ (c) $H_h/D_{cry}=1$

Figure 26 Streamlines and isotherms of 2.5inch GaSe for three cases with different H_h. Ψ_{min}=-280.5 (upper vortex), Ψ_{max}=0.0 (lower vortex); The black arrow indicates the location of solidification interface, the interval is 10K. And the thermal conductivity of ampoule is reduced.

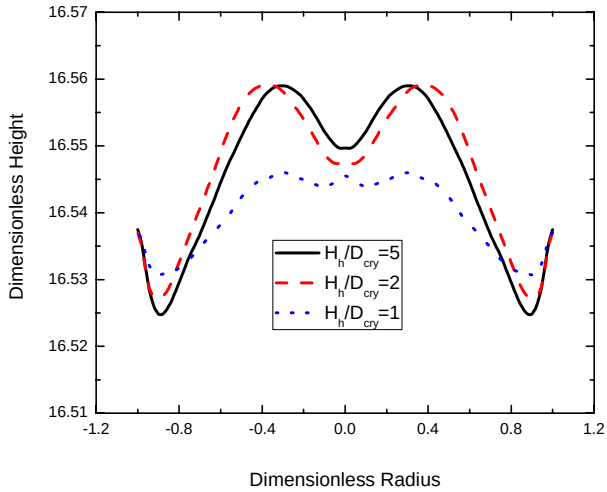

Figure 27 Interface shapes for the cases with a smaller thermal conductivity of the ampoule

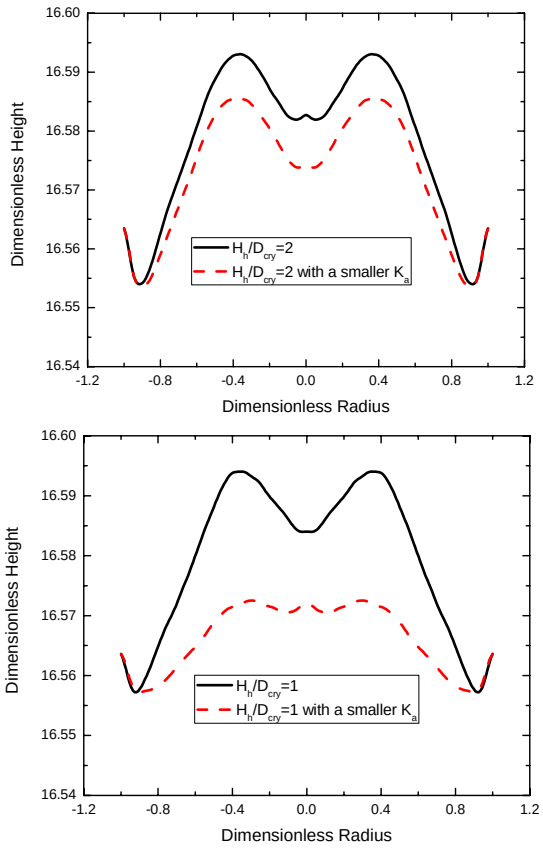

(a) $H_h/D_{cry}=2$ (b) $H_h/D_{cry}=1$

Figure 28 Comparison of the interface shapes for the cases with a normal and smaller thermal conductivity of the ampoule, (a) $H_h/D_{cry}=2$, (b) $H_h/D_{cry}=1$.

6.4.3 Summary

GaSe crystal growth with 2.5 inch and 4.0 inch in diameter is studied. Temperature distribution, velocity field and interface shape are presented for both cases. Using the proposed two hot zone design, the interface is less curved and melt convection is reduced. To further improve the growth process, a scheme by decreasing the thermal conductivity of ampoule is proposed to flatter the interface shape. It is demonstrated that a less curved interface can be obtained by reducing thermal conductivity of the ampoule.

6.5 Conclusions

The effects of Prandtl, Grashof, Stefan and Biot numbers on axial temperature profile, interface shape and temperature, and flow fields are investigated. It is found that the influence of melt flow on temperature distribution is strong when the Prandtl number

is large. For a material with high Prandtl and Grashof numbers, temperature field and growth interface will be significantly influenced by melt convection, resulting in complicated temperature distribution and curved interface shape.

A system with improved heat zone design has been proposed through reducing the length of primary hot zone for suppressing natural convection. Numerical results show that natural convection is significantly suppressed and temperature perturbation is decreased at the growth interface using the new design. Parametric studies are performed to investigate the effects of geometry size of different zones on crystal growth. Simulation results prove that natural convection is significantly suppressed and temperature perturbation is decreased at the growth interface, when the length of hot zone H_2 is reduced. However the length of transition zone has little effect on melt convection and temperature distribution. Simulation results can provide help to optimize this top portion cooling design.

Chapter Seven

Multiphase Flow with Solidification – Application II Crystal Growth by DSS

In this chapter, a numerical model is developed to simulate mc-Si ingot production in an industrial directional solidification furnace. Thermal distribution, interface shape and energy consumption are presented for different operating conditions. The purpose of this part is to evaluate the applicability of thermal design to achieve better crystal quality and energy efficiency. Heat losses at different portions were calculated so that the energy efficiency of the system can be improved. The effects of heating power and the position of the side insulation layer on solidification interface position/shape are discussed. The effects of geometry modification are investigated.

7.1 System Configuration

Multi-crystalline silicon is usually cast in a fused silica crucible supported by graphite, which is placed in a temperature-controlled furnace. After the feedstock is melted, solidification is initiated at the bottom of the crucible when the temperature of silicon melt is reduced to a value below the melting temperature by adjusting heat power and/or moving side insulation layer upward. After a thin layer of silicon grains is formed on the bottom of the crucible, the growth process starts; meanwhile the temperature gradient suitable to growth is maintained by adjusting heater power or by cooling from the bottom through radiation. Figure 29 shows the schematic of the heat zone in a DSS station together with the key heat loss in the system from the top, side and bottom insulation by conduction labeled as $\dot{Q}_1$ $\dot{Q}_2$ and $\dot{Q}_3$, respectively, and from the hot HEX bottom to the cold surrounding by radiation labeled as $\dot{Q}_4$

The furnace is well insulated to ensure no large temperature gradient built in the heat zone. The silicon charge was loaded into a quartz crucible with 69 ×69×46cm^3, and the height of ingot is around 24cm with a mass of approximately 240kg. To improve the productivity, 275kg ingots were grown in this furnace with increased height. Susceptor, which is made of graphite, surrounds the sides of crucible and serves as the heat source/sink during melting and growth. Resistive heaters surrounding the susceptor heat the feedstock and attempt to achieve uniform temperature distribution in the charge. A heat exchange block is assembled in the bottom of susceptor to allow heat dissipation. A movable side insulation layer is moved upward, while the crucible remains stationary, to release energy mainly from the HEX bottom by radiation to achieve the desired cooling rate and ingot growth rate. Thermal couples and optical pyrometer are installed to monitor temperature of specific positions throughout the hot zone to help the thermal profiling and numerical modeling. A water-cooled chamber encapsulates the heat zone and inert gas is regulated. It should be noted that the only movable part in the furnace will be the side insulation layer, which can be moved upward. Figure 30 shows the measured process parameters in the actual growth experiments.

It is noted that Thermocouple 1 (TC1) is installed next to the graphite heaters near the melt surface and its reading is used to control the heat power. During melting, TC1 is initially maintained at a high temperature beyond the melting temperature and it is cooled to a temperature slightly higher than the melting temperature. During the growth, the side insulation moves upward and TC1 changes slightly. After the insulation reaches the maximum position, TC1 is decreased and solidification continues until all melt is solidified. Melt at the four corners will be the last portions to be solidified and the growth rate of the solidification interface is about 1 to 2cm/h. Thermocouple 2 (TC2) is installed vertically in the center of the HEX to monitor the temperature of HEX.

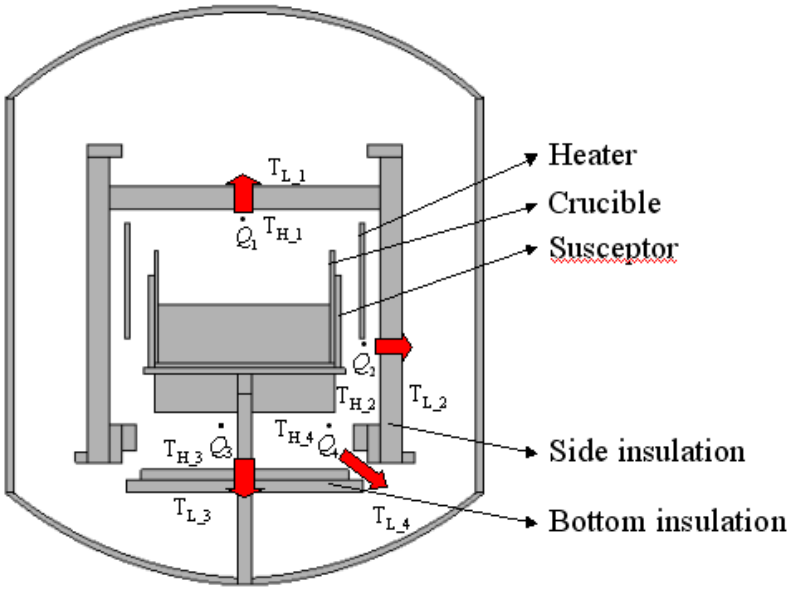

Figure 29 Schematic of a directional solidification furnace

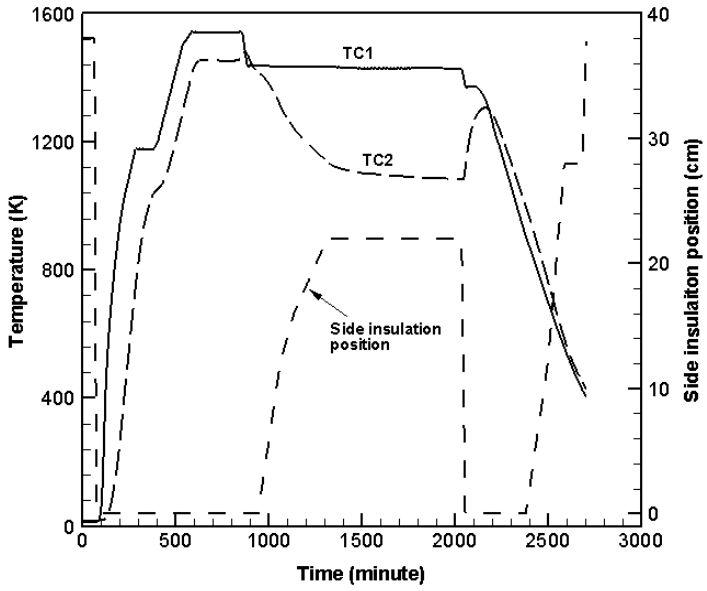

Figure 30 Process parameters for 240kg multi-crystalline silicon ingot growth

7.2 Numerical Model and Energy Balance Analysis

Mathematical model was built considering conductive heat transfer in all solid components, radiative heat exchange between all gray and diffusive surfaces in the furnace, and phase transformation. Radiation is simulated using the discrete ordinates method, and the dependence of thermal physical properties of all components on temperature is also considered. The latent heat release is considered through increasing the effective specific heat – a method proposed by Majchrzak and Szopa (2001). Temperature at the outer surface remains as constant considering water-cooling of the furnace. The generic governing equations are written as follows,

Continuity equation:
$$\frac{\partial \rho}{\partial t} + \nabla \cdot (\rho \vec{u}) = 0, \tag{7.1}$$

Momentum conservation:
$$\frac{\partial}{\partial t}(\rho \vec{u}) + \nabla \cdot (\rho \vec{u} \vec{u}) = -\nabla p + \nabla \cdot \tau_{ij} + \rho \vec{g}, \tag{7.2}$$

Energy conservation:
$$\frac{\partial}{\partial t}(\rho h) + \nabla \cdot (\rho \vec{u} h) = \nabla \cdot (k \nabla T) + S_h, \tag{7.3}$$

where ρ is the density, $\vec{g}$ is the gravitational acceleration vector, $\vec{u}$ is the velocity, p is the pressure, τ is the viscous stress tensor, T is the temperature, k is the thermal conductivity, and S_h is the heat source term. Numerical solutions to the governing equation are realized by using the commercial software CFD-ACE. It shall be noted that the temperature distribution of the furnace depends on the heat power input. As the input heat power increases, the temperature in the crucible increases. It is possible to adjust the heat power input so that the center of the solidification interface is located to a pre-described location.

In order to investigate the relationship between heat power and processing parameters, energy balance analysis was performed to the DSS furnace. As seen in Figure 29, $\dot{Q}_1$, $\dot{Q}_2$ and $\dot{Q}_3$ are the rate of heat loss due to conduction from the top, side and bottom insulation, respectively; $\dot{Q}_4$ is the heat loss rate by radiation from the hot HEX bottom to the cold surrounding. Energy balance analyses are performed for both 3D and 2D geometries.

Table 3 Summarized thermal-physical properties of different components

Component	Material	Density *kg/m^3*	Specific heat *J/kg-K*	Thermal conductivity *W/m-K*	Emissivity
Melt	Liquid Si	2420	1000	64	0.2
Crystal	Solid Si	2300	1059	22	0.7
Crucible	Zyarock quartz	1950	710	0.64 (293K) 0.55 (1073K)	0.6
Suscepter	Graphite	1750	1800	80	0.6
HEX	Dense graphite	1750	1800	80	0.8
Bottom insulation	Felt graphite	150	1000	0.4~2.0	0.8
Side insulation	Felt graphite	150	1000	0.4~2.0	0.8
Top insulation	Felt graphite	150	1000	0.4~2.0	0.8
Chamber	Stainless Steel 304SS	7900	477	15	0.22
Heater	Graphite	1750	1800	80	0.9
Argon near the heater	Argon	0.3485	1141	1	0.0
Argon near the bottom insulation	Argon	0.3485	1141	0.5	0.0
Argon outside the insulation layer	Argon	0.3485	1141	0.2	0.0

7.3 Results and Discussions

7.3.1 Simulation of constant growth rate

Temperature distribution in the furnace can be controlled by heat power through TC1 and the opening of the furnace through the insulation position. To grow a high quality ingot with high productivity, it generally requires that (a) a constant growth rate or a slightly reduced growth rate if the impurity concentration is high, (b) a flat solidification interface or a slightly convex interface. In this case, the crucible wall should remains slightly higher so that nucleation from the crucible wall can be avoided. Also, impurity and defects can be grown outwards.

We aim at achieving constant growth during solidification process while investigate the evolution of heat power, temperature distribution and interface shape as well as temperature gradient. At the beginning of solidification, heat zone is closed, and then the side insulation is moved upward by 4, 8, 12, 16 and 20cm, respectively. Corresponding to five side insulation positions, the interfaces are located in 1/5, 2/5, 3/5, 4/5 and 1, respectively, of the total ingot height, which is 24cm at the end.

Temperature distributions in the overall furnace and silicon at different insulation positions are shown in Figures 31 and 32. In the simulations, we have adjusted heat power to ensure the solidification interface located at the pre-scribed location. Table 4 summarizes the achieved interface location, highest temperature and temperature range in the silicon. It is seen that temperature of solid silicon crystal decreases gradually when solidification processes with a constant growth rate.

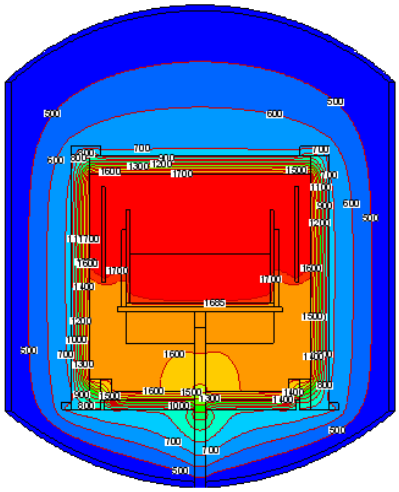

(a)

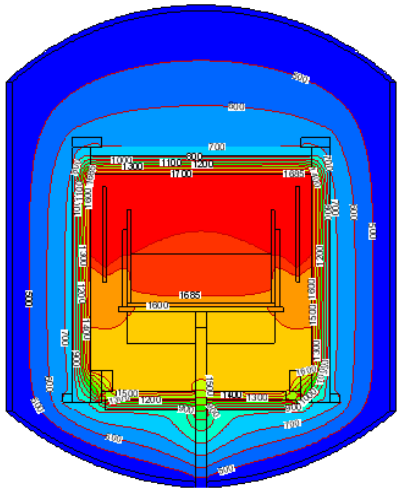

(b)

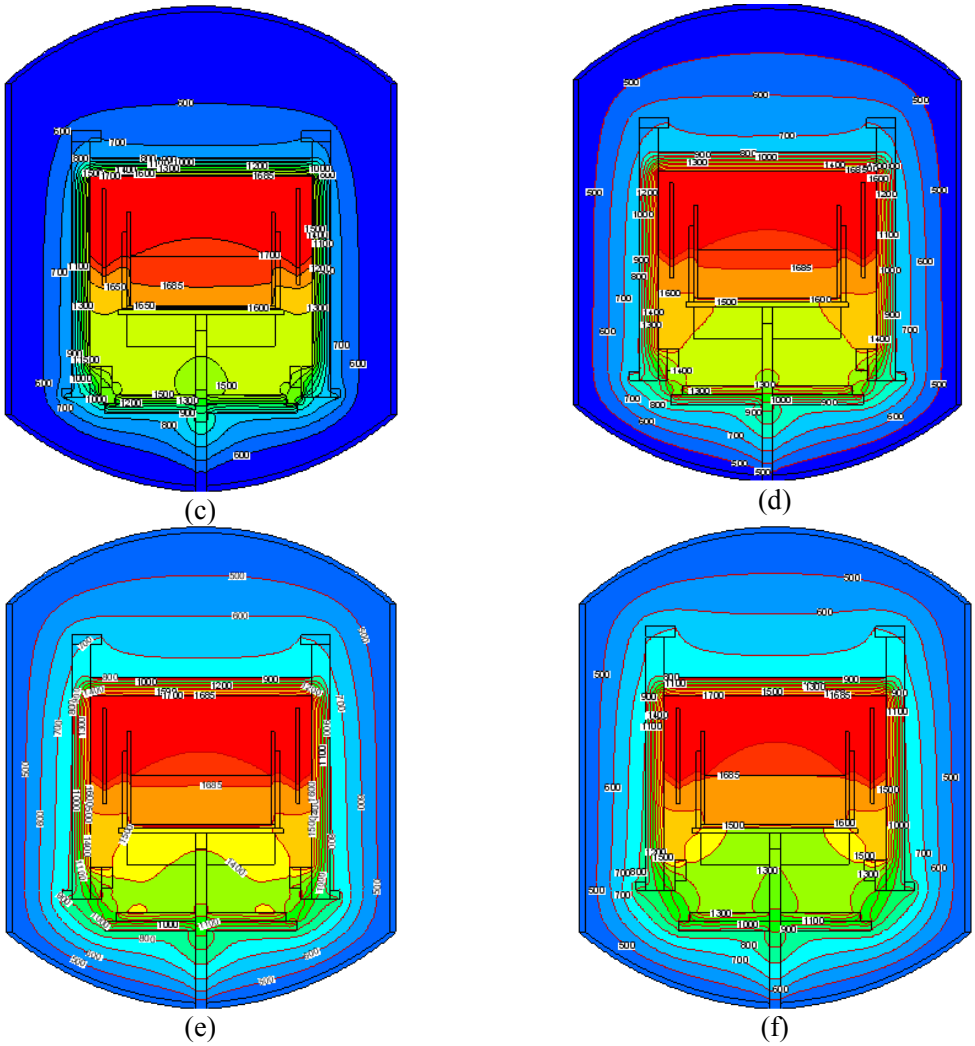

(c) (d) (e) (f)

Figure 31 Temperature distribution in the furnace when side insulation is moved upward by different distances, (a) completely closed, (b) 4cm, (c) 8cm, (d) 12cm, (e) 16cm, (f) 20cm

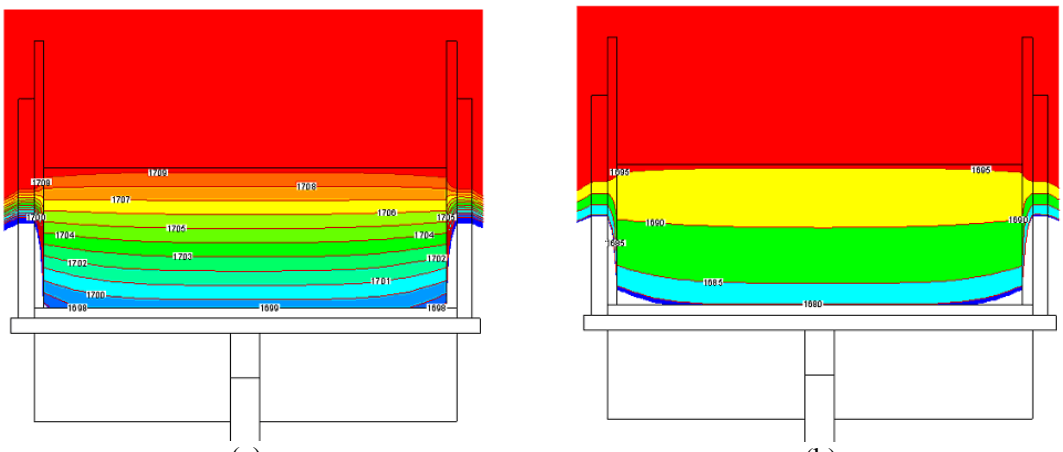

(a) (b)

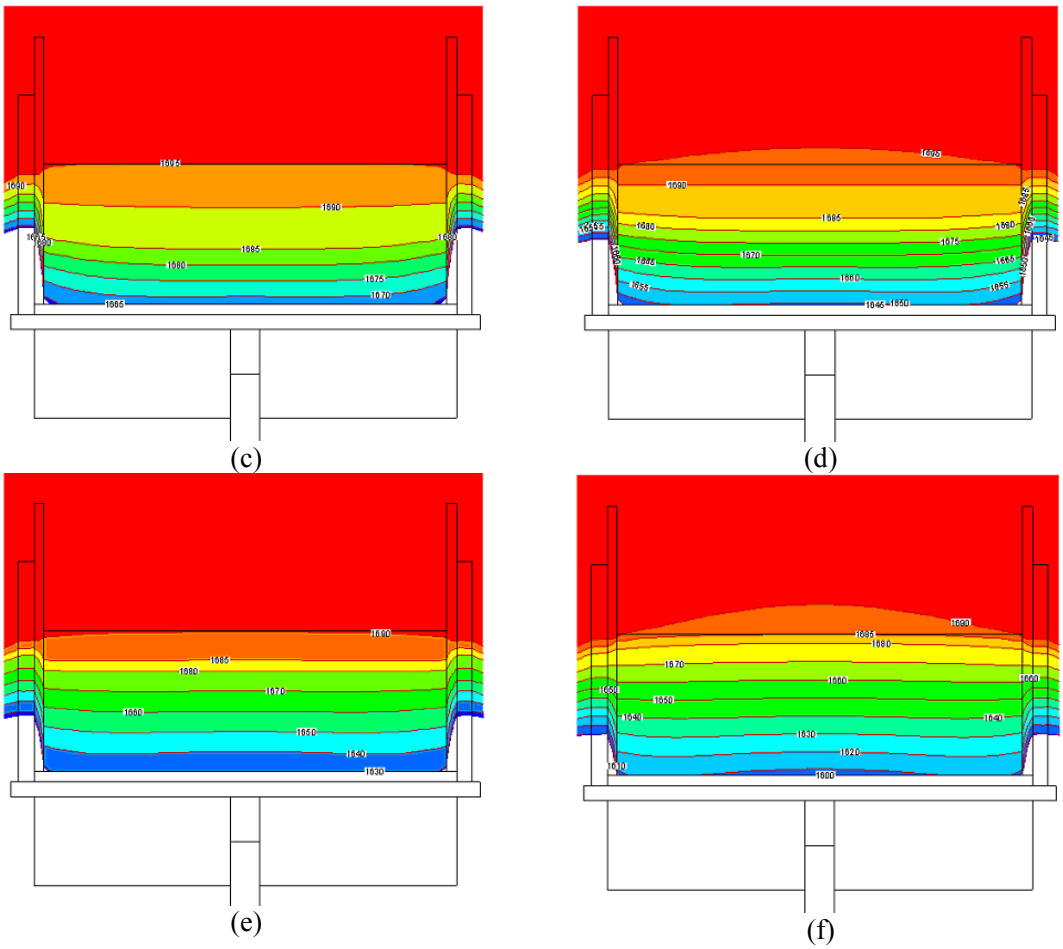

Figure 32 Temperature distribution in the silicon when side insulation is moved upward by different distances, (a) completely closed, (b) 4cm, (c) 8cm, (d) 12cm, (e) 16cm, (f) 20cm

Table 4 Achieved interface locations and temperature ranges in the silicon

Insulation location (cm)	Specified interface location (cm)	Achieved interface location (cm)	Highest temperature (K)	Temperature range in the silicon (K)
0	0	-0.3	1746	1698~1709
4	4.8	3.8	1737	1680~1696
8	9.6	9.4	1744	1667~1695
12	14.4	14.8	1750	1648~1693
16	19.2	19.1	1755	1630~1690
20	24.0	24.1	1755	1607~1685

Figure 33 is the energy balance analyses based on assumed 2D and actual 3D geometries. The temperature used in calculating conduction and radiation heat loss $\dot{Q}_1$, $\dot{Q}_2$ $\dot{Q}_3$ and $\dot{Q}_4$ are simulation results. $\dot{Q}_{total}$ is the calculated consumed heater power based on temperature distribution for energy balance. $\dot{Q}_{real}$ is the heater power used in numerical simulations. From energy balance analysis results, it is concluded that: (i) $\dot{Q}_1$ and $\dot{Q}_3$ change slightly with the movement of side insulation upward; (ii) $\dot{Q}_2$ decreases linearly with the movement of side insulation upward, due to the decrease of conduction area; (iii) Radiation heat loss, $\dot{Q}_4$, increases sharply due to the gap increase with the side insulation movement upward; (iv) Calculated heater power, $\dot{Q}_{total}$, increases mainly due to the increase of radiation heat loss; (v) from 2D analysis, real heater power used in CFD-ACE, $\dot{Q}_{real}$, is almost equal to the calculated heater power, $\dot{Q}_{total}$, indicating the energy balance achieved for 2D case and consequently verifying the validation of current model.

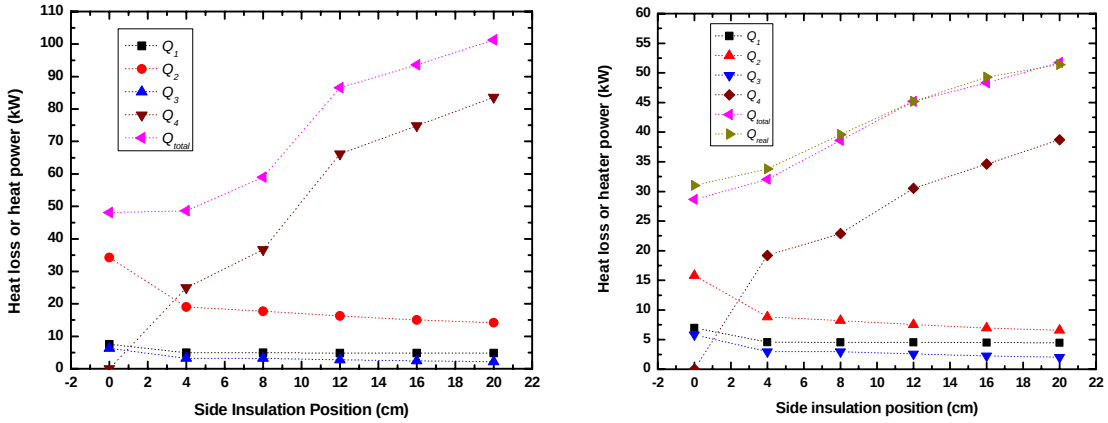

Figure 33 Energy balance analysis based on simulation results, (a) 3D analysis, (b) 2D analysis, $\dot{Q}_{total}$ is the calculated heater power to be consumed based on temperature distribution to make energy balance. $\dot{Q}_{real}$ is the heater power used in CFD-ACE simulation.

Temperature profiles in the vertical direction along the centerline of the silicon and the outer wall of susceptor are also investigated, shown in Figure 34. The temperature

difference between the centerline and outer wall is also plotted in Figure 35. It is noted that this temperature difference is related to melt inclusion and density of grain boundary and dislocations. It is seen that the temperature gradients among the silicon in the vertical direction along the centerline of the silicon initially does not change much with the movement of side insulation, while side insulation is further moved upward, this temperature difference is significantly enlarged.

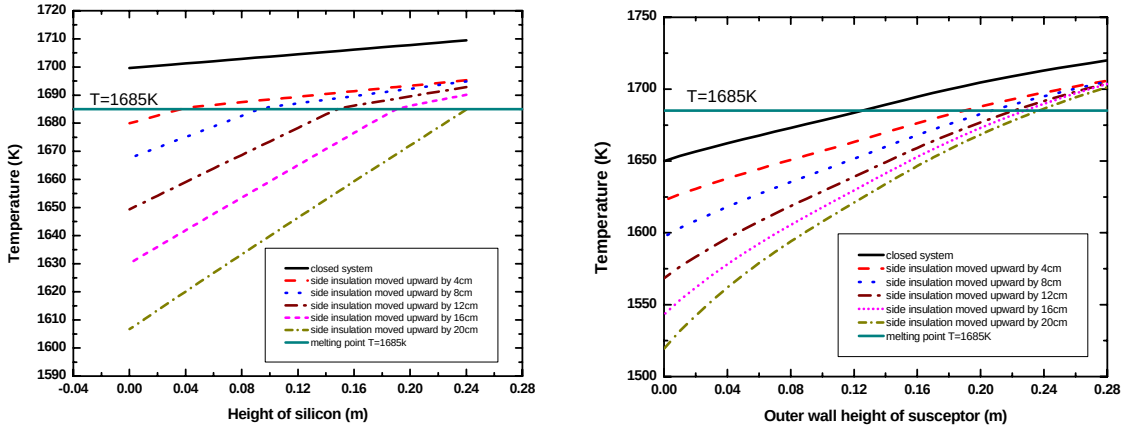

(a) (b)

Figure 34 Temperature profiles in the vertical direction along (a) the centerline of silicon, (b) outer wall of susceptor

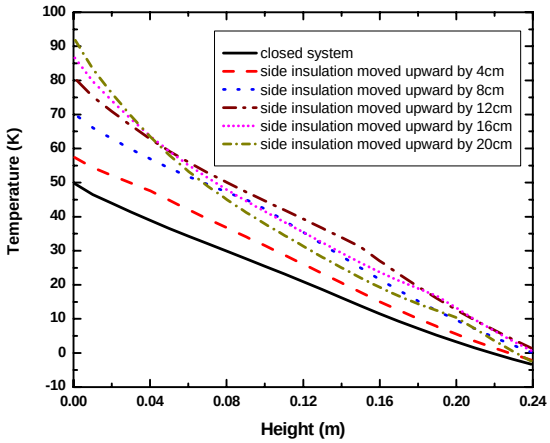

Figure 35 Temperature difference between the centerline of silicon and outer wall of susceptor

7.3.2 Effect of thermal conductivity of insulation layer

According to energy balance analysis, thermal conductivity of insulation layer plays an important role in determining heat loss rate due to conduction from the top, side and bottom insulation layer to surroundings. Effects of thermal conductivity of insulation layer on heat loss rate and consumed heater power are thus investigated. In the baseline case, thermal conductivity of insulation layer is k=0.4W/m K, and thermal conductivity with 0.2, 0.6, 0.8 and 1.2 W/m K, is also tested. For all of these cases, side insulation is moved upward by 12cm, and meanwhile the heat power is tuned to achieve the specified interface position, which is located in the 3/5 of the total ingot height. Figure 36 presents the change of heater power used in CFD-ACE and the highest temperature achieved in the furnace with the variation of thermal conductivity of insulation layer. Heater power and achieved highest temperature increase linearly with the increase of thermal conductivity. The temperature distribution in the whole furnace and the silicon region are also obtained (results are not shown here). It is found that although heater power varies in different cases, the temperature range in the silicon region is almost the same, which is between 1650 and 1695K.

3D energy balance analysis is also performed based on the simulation results, as shown in Figure 37. The key observations are summarized as follows: (i) $\dot{Q}_1$ and $\dot{Q}_3$ increases linearly with increase of thermal conductivity of insulation layer; (ii) $\dot{Q}_2$ increases much faster due to its larger conduction area with increase of thermal conductivity of insulation layer; (iii) Radiation heat loss $\dot{Q}_4$ almost keep the same since the very similar temperature distribution is obtained in the region near HEX; (iv) Heater power increases because of the increase of heat conduction loss; (v) For 3D energy balance analysis, the difference between real heater power used in CFD-ACE and calculated total heater power become larger with increase of thermal conductivity.

Table 5 Summary of interface location, heater power, highest temperature and temperature range in the silicon when thermal conductivity of insulation layer varied

Thermal conductivity of insulation layer (W/m-K)	Achieved interface location (cm)	Heater power in CFD-ACE (W)	Highest temperature (K)	Temperature range in the Silicon (K)
0.2	14.8	19400	1744	1650~1693
0.4	14.8	22600	1750	1648~1693
0.6	14.2	25550	1757	1650~1695
0.8	14.0	28270	1763	1650~1695
1.2	14.3	33200	1773	1649~1695

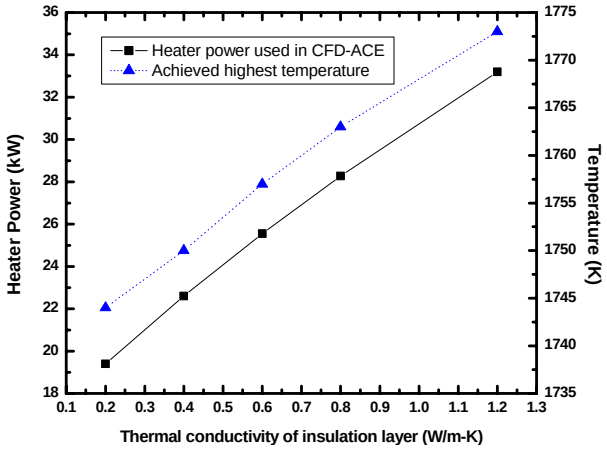

Figure 36 Heater power used in CFD-ACE and highest temperature achieved when thermal conductivity of insulation layer varies

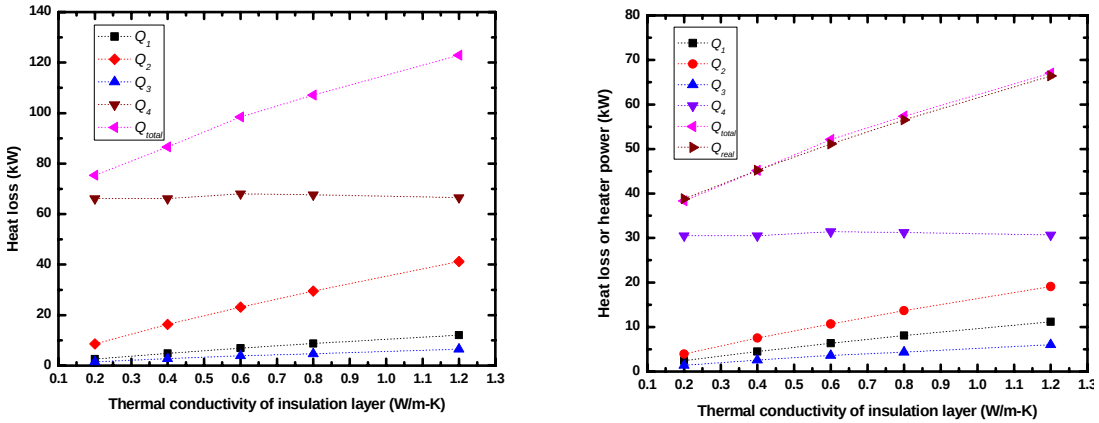

Figure 37 Energy balance analysis with the variation of thermal conductivity of insulation layer, (a) 3D energy balance analysis, (b) 2D energy balance analysis

7.3.3 Effect of partition part

A partition part is placed under the heater power to serve as radiation shield. In this case, side insulation is moved upward by 20cm, and interface to be achieved is located at the top of silicon ingot. The effects of partition part on consumed heater power and temperature difference between the centerline of silicon and outer wall of susceptor are studied. Temperature distributions in the furnace and silicon are described in Figure 38. Figure 40 presents temperature difference between the centerline of silicon and outer wall of susceptor. It is found that temperature contour in the silicon becomes from concave to convex and temperature difference between outer wall of susceptor and center of silicon is larger with the addition of partition part.

Energy balance analysis is completed to reveal the relationship of heater power with partition part. Compared with the results of the case without partition part, the conclusions are derived as follows: (i) $\dot{Q}_1$ almost keeps the same; (ii) $\dot{Q}_2$ increases a little bit due to the increase of temperature difference between inner and outer side of insulation layer; (iii) $\dot{Q}_3$ decreases due to the lower temperature under HEX; (iv) Radiation heat loss, $\dot{Q}_4$, decreases intensely because of lower temperature under HEX; (v) Heater power dramatically decreases by 30% mainly due to reduction of radiation heat loss.

The temperature contours in Figure 38 indicate melt/solid interface shape during solidification. With the addition of partition part, interface becomes convex from the flat

or slightly concave. It is well known that a slightly convex interface shape is favorable since impurities can be pushed away from the solidification front into corner region of the ingot and improve the crystal quality and lifetime. Therefore, the modification in system geometry can improve energy efficiency as well as crystal quality.

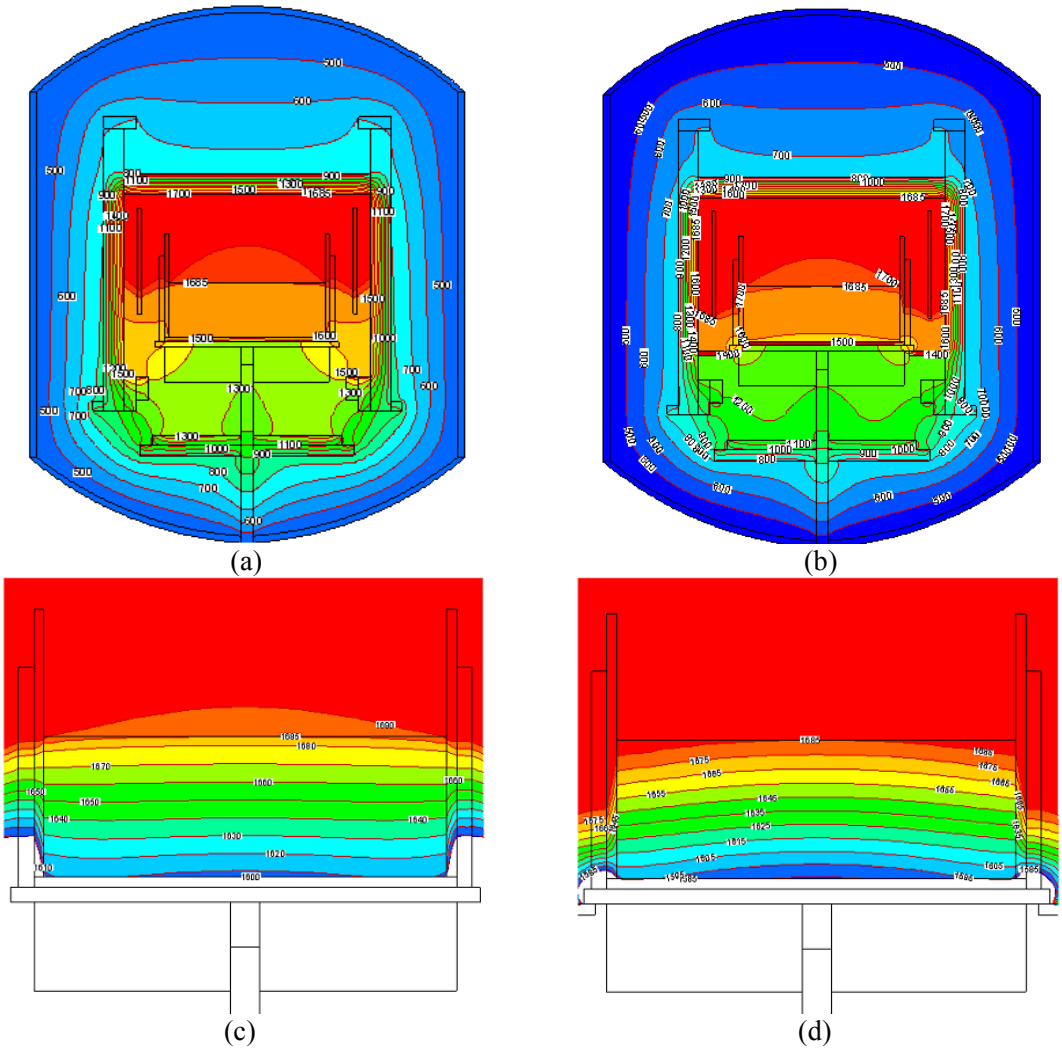

Figure 38 Temperature distribution in the furnace and silicon for two systems: (a) without partition part; (b) with partition part

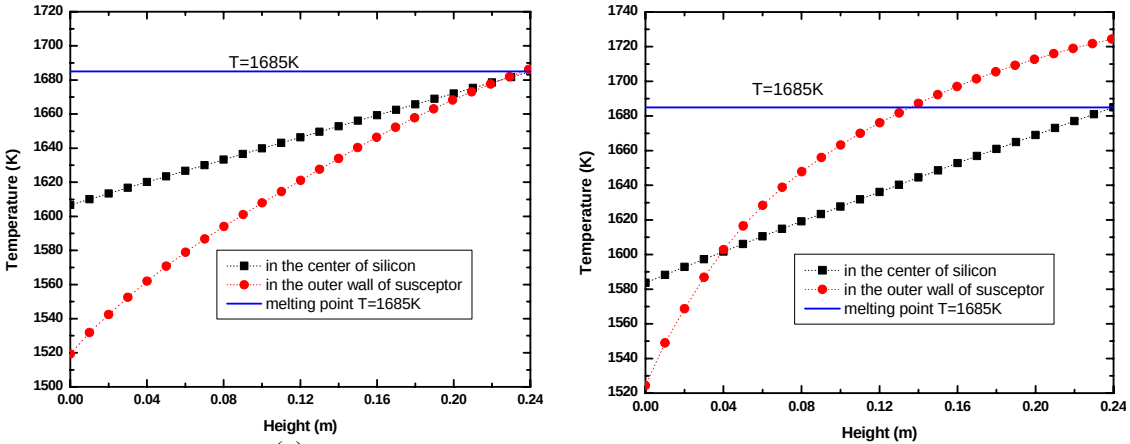

Figure 39 Temperature profiles in the vertical direction along the centerline of silicon and outer wall of susceptor for two systems (a) without partition part; (b) with partition part

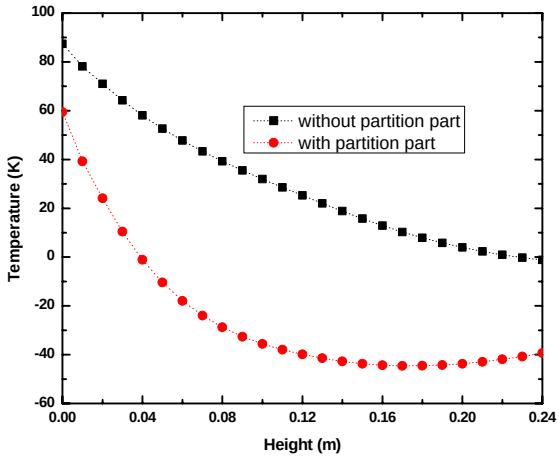

Figure 40 Comparison of temperature difference between the centerline of silicon and outer wall of susceptor for system without and with partition part

Table 6 3D Energy balance analysis for different systems

System	$\dot{Q}_1$ (W)	$\dot{Q}_2$ (W)	$\dot{Q}_3$ (W)	$\dot{Q}_4$ (W)	$\dot{Q}_{total}$ (W)
without partition part	4826	14184	2167	83623	101276
with partition part	4886	16122	1835	55372	74961

Table 7 2D Energy balance analysis for different systems

System	$\dot{Q}_1$ (W)	$\dot{Q}_2$ (W)	$\dot{Q}_3$ (W)	$\dot{Q}_4$ (W)	$\dot{Q}_{total}$ (W)	$\dot{Q}_{real}$ (W)
Without partition part	4469	6557	2006	38714	51756	51400
With partition part	4524	7464	1699	25635	39323	39200

7.3.4 Proposed method to detect the solidification interface

It is difficult to detect solidification interface location by laser or other optical method during growth. Although ultrasonic can be used for silicon interface detection during melting and solidification, it is not visible to install it in the production line. In the current production line, a quartz stick is used to detect the interface location and growth rate. This method may affect the stability of the growth interface. Without the interface location, the feedback for fully process control is not possible. It is therefore important to find an easy method to detect the solidification interface location.

One of easy methods is through the volume change. Since the density of solid silicon is smaller than that of the melt, total volume will be increased during solidification although total mass is almost unchanged. By monitoring the volume or height changes, it is possible to detect the solidification interface location if the solidification interface is assumed to be flat. So far, nobody has tested this method in the experiments.

In this section, we propose another method, in which we will utilize thermocouples, TC1 and TC2, as shown in Figure 41. The question is whether it is possible to find the interface location through the readings of TC1 and TC2. An analytic solution is proposed to investigate the temperature at the bottom of heat exchange block, TC2 and correlate temperature readings in TC2 with the growth rate. It is assumed that temperature profile from the top of melt to the bottom of heat exchange block is piecewise linear. Therefore we can calculate the heat flux released from the liquid and removed from the silicon solid. According to energy balance at the growth interface, the following formulation can be obtained

$$\frac{(T_m - T_2)}{\frac{x}{k_s} + \frac{D}{k_g}} = \frac{k_l (T_1 - T_m)}{L - x} + \rho L_{latent} \frac{dx}{dt} \tag{7.4}$$

where T_1 and T_2 is the temperatures at the top of the melt and bottom of heat exchange block, respectively; T_m is the melting point of silicon; k_l , k_s and k_g is the thermal conductivity of melt, solid and heat exchange block. We have assumed that no melt undercooling exists and convection heat transfer can be factored into thermal conductivity of the melt. In this formulation, only unknown parameters are T_1, T_2 and x. If we can measure T_1 and T_2, it is possible to solve x from this equation. Of course, this equation can be further improved considering convection heat transfer and heating from side.

To prove the concept, we further assume that T_1 is a linear function of x changing from 1713K at x=0 to $T_1=T_m=1685$K at $x=L$, then the expression of T_1 can be formulated as,

$$T_1 = -\frac{28}{L} x + 1713 \tag{7.5}$$

We can then write T_2 as follows

$$T_2 = T_m - \left(\frac{x}{k_s} + \frac{D}{k_g} \right) \left[\frac{k_l (-\frac{28}{L} x + 28)}{L - x} + \rho L_{latent} c \right] \tag{7.6}$$

Figure 43 plots the results of T_1 and T_2 from numerical results and above analytic solution at steady state. The change of T_2 predicted by analytic solution agrees fairly well with numerical prediction. If other factors are considered in analytic solution such as heating from side and convection heat transfer, the agreement can be easily improved. From Figure 43, it can be concluded that T_2 decreases as the growth rate increases. It is therefore possible to find the growth rate when T_1 and T_2 are measured.

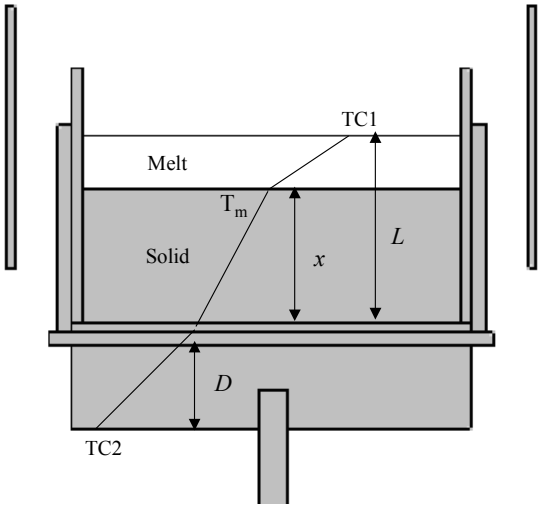

Figure 41 Temperature profile in the solid, melt and graphite

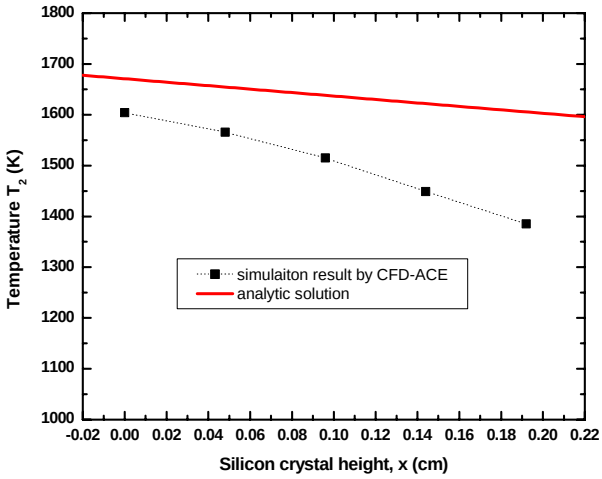

Figure 42 HEX bottom temperature T_2 when growth rate is zero

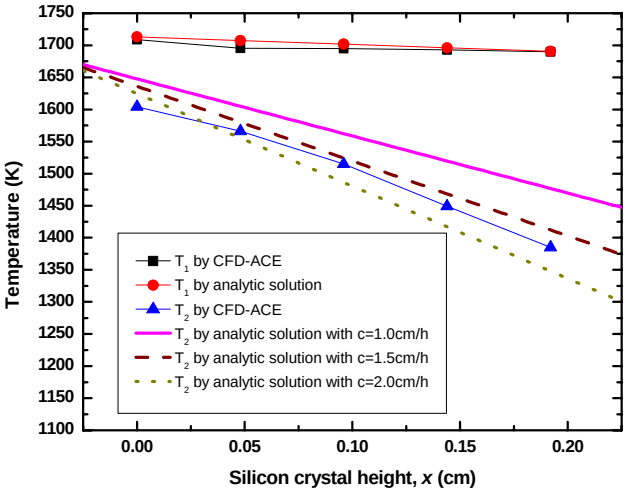

Figure 43 Comparison about T_1 and T_2 between simulation results and analytic solution

7.4 Conclusions

In this part, A numerical model is developed to study heat transfer and solidification in an industrial directional solidification system used for multi-crystalline silicon ingot production. The evolution of temperature distribution and interface are presented for various operational conditions. The energy balance is provided and heat loss at different portion is calculated as the gap size increases. It can be found the effectiveness of the insulation and hot zone design. The effects of thermal conductivity of insulation layer are also discussed. It can be concluded that consumed heating power increases because of the increase of heat conduction loss. A key geometry modification of furnace components, where partition part is placed under the heater power, is investigated. By adding a radiation partition in between the heater and cooling area, the energy can be saved by 30%. However, temperature gradient in the silicon ingot is increased. By this way, the gap size can be reduced. The methods to detect the solidification interface are also proposed and proved.

Chapter 8

Multiphase Flow with Chemical Reaction – Application: Synthesis of Uranium-ceramic Nuclear Fuel

A global model for pyrolysis processing was developed in the prior research in which the Darcy's law and convection-diffusion equations were used to model the volatile flow in porous media. The system level or global model describes polymer pyrolysis processing, including heat transfer, polymer pyrolysis, SiC crystallization, chemical reactions, and volatiles transport. However, the modeling of particle level structure evolution of composite produced during synthesis of uranium oxide and SiC is needed for process optimization. In this chapter, a mesoscopic particle-level model is developed based on meshless particle method to study the structure and species evolution at the mesoscopic or local level. The mesoscopic model is applied to a repetitive unit cell and describes mass transport, composition change and movement of particles. The unit cell represents a unit of the source material that consists of several U_3O_8 particles, SiC matrix and other components produced from synthesis. The Smoothed Particle Hydrodynamics (SPH) technique is employed to solve the solid-solid reaction between SiC matrix and filler particles, composition changes, uniformity of resulting products, and shrinkage and motion of U_3O_8 particles in SiC matrix. Results from system-level simulation are used to provide the necessary thermal boundary conditions for the particle level simulations. The structure and composition of produced composite evolved due to heat fluxes are monitored. The effects of heating rate and U_3O_8 particle size and volume

on species uniformity and structure formation are investigated. Uncertainty due to random distribution of filler particles is also investigated.

8.1 Numerical Method

8.1.1 Assumptions

U_3O_8 filler particles are assumed to disperse in the SiC matrix and both are represented by the SPH particles, as shown in Figure 44. These SPH particles are assigned a mass, position, density, temperature and concentration of SiC or filler particles. SiC particles are assumed to be stationary due to the matrix structure. U_3O_8 filler particles are allowed to move and also react with SiC SPH particles. If the temperature of a SPH U_3O_8 particle is above 1200˚C, it will be converted into UO_2. If SiC volume ratio in a SPH UO_2 particle is above a critical value and the temperature of SPH UO_2 particle is above 1400˚C, SPH UO_2 particle will be converted into UC particle. The critical concentration value ensures enough SiC particles being present to synthesize with the SPH UO_2 particles.

In the current model, SiC particles are assumed to be stationary since SiC forms a matrix. Due to the elevation in density and reduced mass of the filler particles (U_3O_8 or other components produced) during synthesis process, the shrinkage of filler particles needs to be considered. In our model, it is assumed that U_3O_8/UO_2 particles shrink once they are converted to UO_2/UC particles. Gaps between the filler particles and SiC matrix are thus formed. The filler particle can move in the gap as the result of the pressure change caused by generated gases. The total pressure on each filler particle is related to gas production rate determined from reaction rate. The structure of SiC matrix forms a force to impede the motion of filler particles. It is assumed that the impedance of the motion is induced by the springs or forces from the neighboring structure. In other words, the filler particle is assumed to sit at the center initially (Figure 45), and total force on the filler particle is the summation of all the forces from the neighboring matrix. Without reaction, the forces surrounding the filler particle are at equilibrium.

Two key reactions are considered for synthesis process. It is assumed that reaction 1 (4.4) occurs when temperature is above 1200˚C and reaction 2 (4.5) occurs when temperature is higher than 1400˚C.

$$1\ \text{kg}\ U_3O_8 \rightarrow \alpha_3\ \text{kg}\ UO_2 + (1-\alpha_3)\ \text{kg}\ P_3 \quad (4.4)$$

$$1\ \text{kg SiC} + \alpha_4\ \text{kg}\ UO_2 \rightarrow \alpha_5\ \text{kg UC} + (1+\alpha_4-\alpha_5-\alpha_6)\ \text{kg}\ \textit{Products} + \alpha_6\ \text{kg}\ P_4 \quad (4.5)$$

where a_3, a_4, a_5 and a_6 are mass (kg) based stoichmetry constants; P_1 and P_2 represent volatiles produced from reactions 1 and 2, respectively. It should be noted that the reactions between SiC and U_3O_8 are not known yet, but UC is the product. The detailed reaction kinetics and mechanisms are yet to be established. Nevertheless, this chapter employs two global reaction steps. Once the detailed reaction kinetics and mechanisms are established in the experiments, the model can be improved.

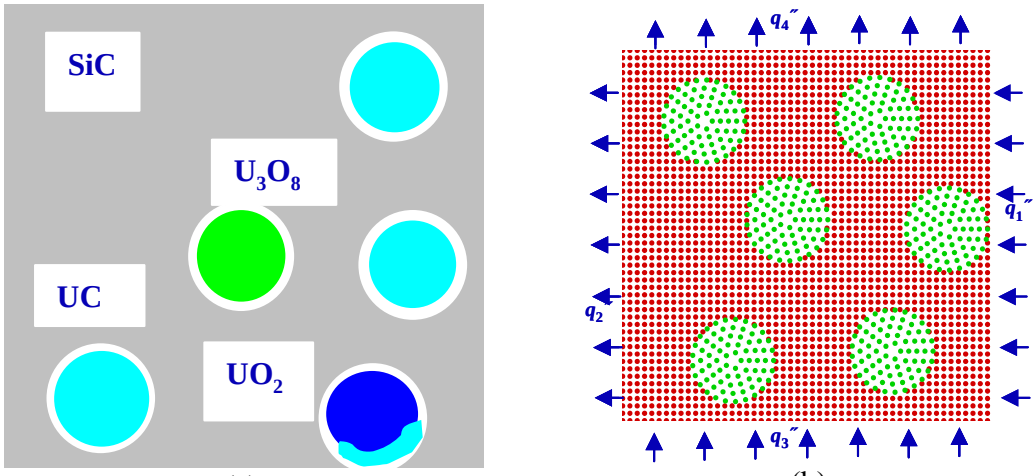

(a) (b)

Figure 44 Schematic of the SPH local model and thermal boundary conditions, (a) mesoscopic model and computational domain, (b) boundary conditions in the mesoscopic model

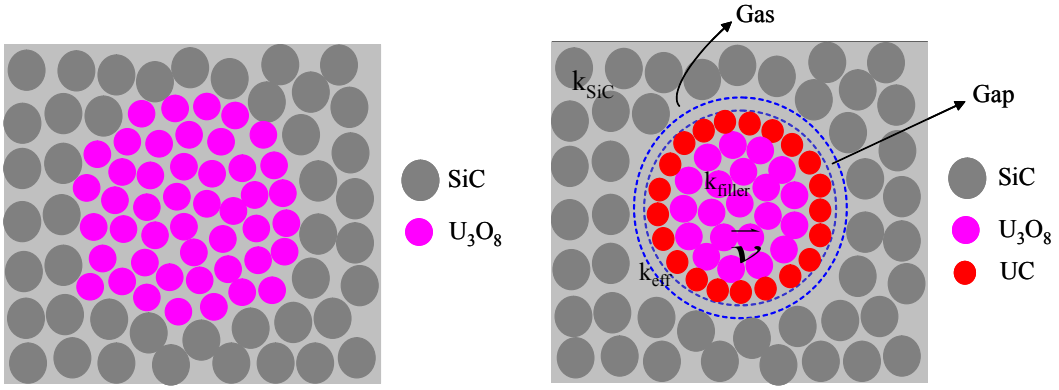

(a) Initial formation (b) Gap formation and shrinkage

Figure 45 Model of shrinkage and movement. k_{filler}, k_{eff} and k_{SiC} are the thermal conductivity of filler particles, gap and SiC matrix, respectively.

8.1.2 SPH Equations

The mass conservation equation in the Lagrangian form is written as

$$\frac{D\rho}{Dt} + \rho\nabla \cdot v = \dot{m} \tag{8.1}$$

The SPH form of mass conservation equation is

$$\frac{D\rho_i}{Dt} = -\rho_i \sum_{j=1}^{N} \frac{m_j}{\rho_j} v_{ij}^{\beta} \cdot \frac{\partial W_{ij}}{\partial x_i^{\beta}} + \dot{m}_i \tag{8.2}$$

where m_i and ρ_i are the mass and density of particle i, respectively; W_{ij} is so called kernel function in SPH; β is the coordinate direction; $v_{ij}^{\beta} = (v_i^{\beta} - v_j^{\beta})$.

The energy equation in the Lagrangian form is as follows:

$$\rho c_P \frac{DT}{Dt} = \nabla\left(k\nabla T\right) + \dot{Q} \tag{8.3}$$

The particle approximation of energy is expressed as:

$$\left(\rho c_p \frac{DT}{Dt}\right)_i = \left(\sum_j \frac{m_j}{\rho_j}(k_j - k_i)\frac{\partial W_{ij}}{\partial x_i^{\beta}}\right)\left(\sum_j \frac{m_j}{\rho_j}(T_j - T_i)\frac{\partial W_{ij}}{\partial x_i^{\beta}}\right) + k_i \sum_j \frac{m_j}{\rho_j}(T_j - T_i)\frac{\partial^2 W_{ij}}{\partial x_i^{\beta}\partial x_i^{\beta}} + \dot{Q}_i \tag{8.4}$$

The mass fraction of SiC is *Y* so that the mass of SiC in a mass *M* of medium is *YM*. The diffusion and reaction of SiC is given by the following equation [134]:

$$\frac{DY}{Dt} = \frac{1}{\rho}\nabla\left(D\nabla Y\right) + \dot{Y} \tag{8.5}$$

where *D* is the coefficient of diffusion. The rate of change of mass fraction Y_i is given by

$$\left(\frac{DY}{Dt}\right)_i = \left(\sum_j \frac{m_j}{\rho_j}(D_j - D_i)\frac{\partial W_{ij}}{\partial x_i^{\beta}}\right)\left(\sum_j \frac{m_j}{\rho_j}(Y_j - Y_i)\frac{\partial W_{ij}}{\partial x_i^{\beta}}\right) + D_i \sum_j \frac{m_j}{\rho_j}(Y_j - Y_i)\frac{\partial^2 W_{ij}}{\partial x_i^{\beta}\partial x_i^{\beta}} + \dot{Y}_i \tag{8.6}$$

Note that diffusion is very weak in this process comparing with reaction.

It is assumed that the heat content of the system only changes because the particles lose or gain heat through the boundary, although it would be possible to include the heat sources such as reaction heating. For the problem considered here, the heat fluxes are

obtained from the global model and are applied to the SiC particles at the four boundaries.

Using the standard techniques such as the leapfrog (LF), predictor–corrector and Runge–Kutta (RK) schemes can carry out numerical integration of ordinary differential equations for physical variables for every particle. In this paper, the LF method is employed for its low memory storage and efficiency. The particle density, velocity, internal energy and position can be updated with the LF method [135].

Table 8 Thermophysical properties used in the analysis and modeling

Parameters	Value used in the model
c_{pg} (J/kg K)	1600
c_{ps}(J/kg K)	1080
k_{s1} (W/m K)	100
k_{s2} (W/m K)	100
k_{gas} (W/m K)	0.1859
ρ_1 (kg/m^3)	8600
ρ_2 (kg/m^3)	2500
ρ_g (kg/m^3)	0.15
D (m^2/s)	4.5×10^{-8}

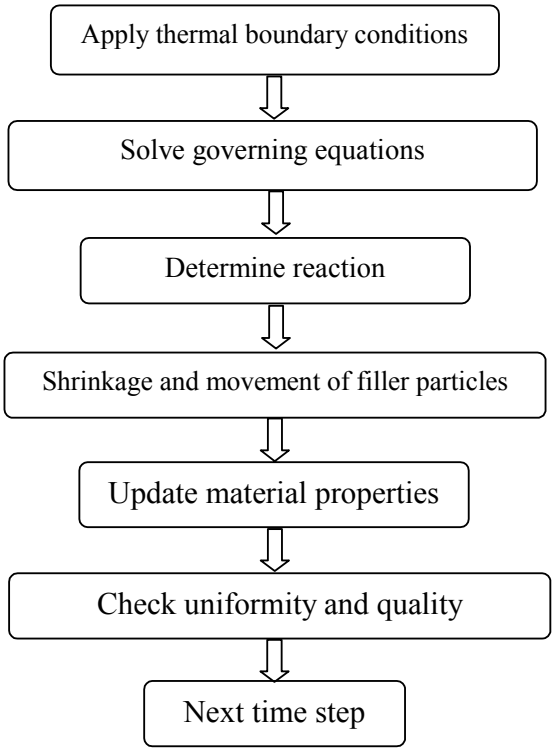

Figure 46 Flow chart in process simulation

8.2 Shrinkage and Particle Movement

At the beginning, a filler particle generated by many SPH particles is set in the middle of SiC matrix. The pressure forces acted on the filler particle are calculated from the forces acted on all SPH filler particles. They are balanced. Due to heat flux and temperature change during process, temperature of some portion of particle will increase, and SPH particles will react and they will shrink locally. The pressure forces due to gas products will generate larger forces on the SPH filler particles near the reaction region. The filler particles will then be pushed to move due to the imbalance of the total forces. The movement will continue until reactions are completed. There are two ways to handle the gap. The first method is assuming that there is a small gap between the filler particle and surrounding SiC matrix and gap contains no material. The SPH particles are pushed away by the gap. The overall density, thermal conductivity and diffusivity will be reduced slightly due to SPH particle positions change. The second method is more complicated. The gas SPH particles are generated and filled into the gap. The gas SPH particles will have their own properties such as mass, thermal conductivity, etc. Both

methods are tested. However, since the gap between the filler particle and SiC matrix is usually very small in our cases, e.g., it is smaller than 25% of the smoothing length. The results obtained by two methods provide the almost the same results. Using the SPH method, shrinkage and movement of filler particles can be treated straightforward. This is one of advantages of this method comparing with the grid methods.

8.3 Results and Discussion

Basic thermal and physical properties used in the simulation are listed in Table 8. The dimension of the unit is identical to the macrocell size in the global model: 0.62mm×0.62mm. The black and the grey solid circles represent the SPH SiC particles and U_3O_8 particles, respectively. Four heat fluxes, q_i'' (i=1, 2, 3, and 4) are computed from the global model and applied to four boundaries. The directions of the heat fluxes are also illustrated. It is noted that the heat fluxes in the x-direction is higher than that in the y-direction. We study the effect of heating rate, q_i'', applied to the macro computational domain, filler particle volume and size on the evolution of species and structures.

8.3.1 Baseline case study

A baseline case is selected as follows: volume ratio of the filler particles is 20%, and filler particle diameter is 0.062mm. The heating flux applied to the macro computational domain is 0.05W/m^2. The structure and composition evolution of the baseline case is presented first. Figure 47 shows the structure evolution of the filler particles for the baseline case. The black solid circle, grey solid circle, black hollow circle and black triangle represent SiC, U_3O_8, UO_2 and UC, respectively. It is seen that the SPH U_3O_8 particles close to the right and lower boundaries are converted to UO_2 first (Figure 47(a) and (b)), this is due to the directions of heat fluxes in x- and y- directions. In addition, owing to the same reason, SPH UO_2 particles close to the right and lower boundaries, are converted to UC first (Figure 47(c)~(f)). Meanwhile, SPH UO_2 particles close the SiC matrix are converted to UC earlier. It is interesting to notice that some UO_2 SPH particles very close to the right boundary remain unchanged (Figure 47(d) and (e)); this can be explained by less availability of SiC. To quantify the composition evolution of

the filler, we plot the ratio of SPH particles of U_3O_8, UO_2, and UC to all the SPH filler particles (total number of SPH U_3O_8, UO_2, and UC particles), as shown in Figure 48. The total number of SPH UO_2 particles increases first, and then decreases due to the reaction with SiC. It is illustrated that the UC production rate keeps very high from 10hours to 18hours, and decreases dramatically after 18hours due to less availability of UO_2. Furthermore, the filler particles shrink after all the SPH U_3O_8 particles are converted to UO_2 as shown in Figure 47 (b)~(f). The gap is formed between the filler particle and SiC matrix.

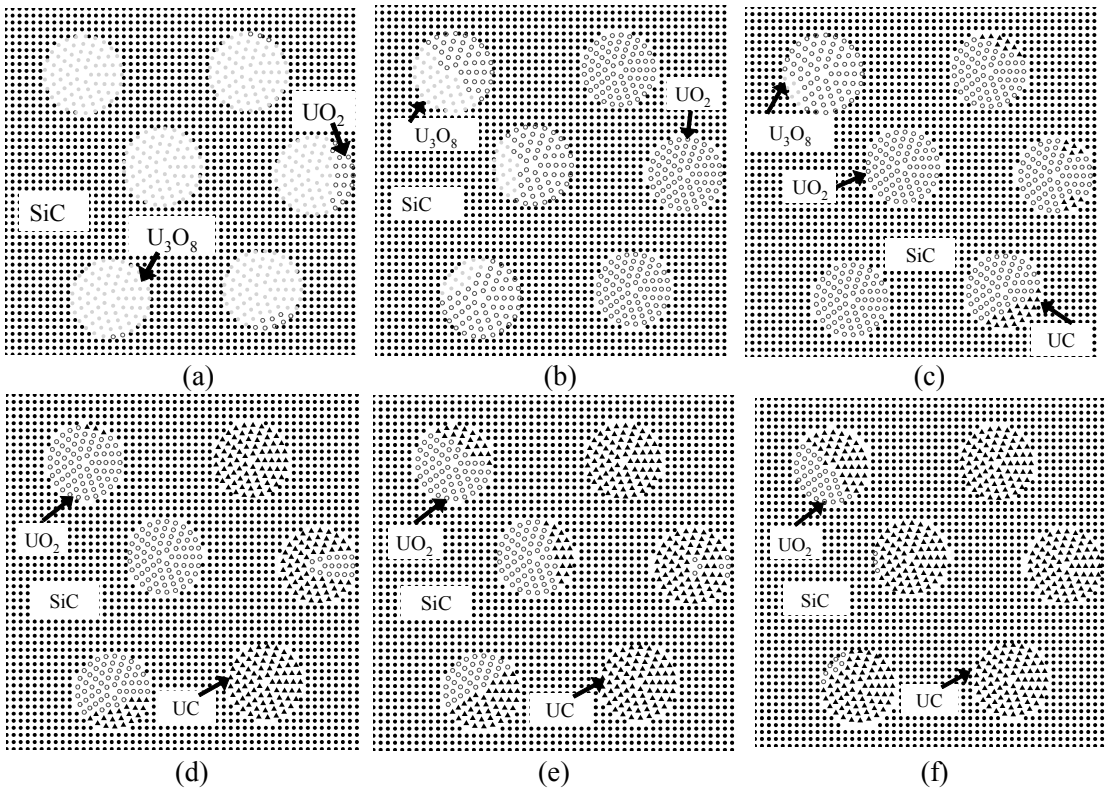

Figure 47 Structure evolutions of filler particles for the baseline case. The volume ratio of filler particles is 20%. Diameter of the filler particles is 0.062mm. Reaction time is (a) 5.5hours, (b) 7.0hours, (c) 8.5hours, (d) 10hours, (e) 11.5hour, and (f) 13hours. The black solid circle, grey solid circle, black hollow circle and black triangle represent SiC, U_3O_8, UO_2 and UC, respectively.

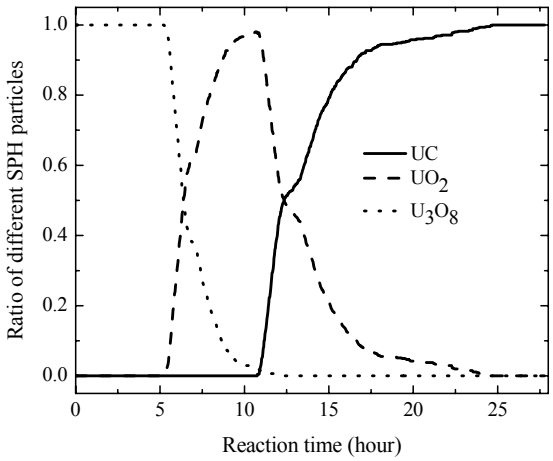

Figure 48 Composition evolution of filler particles for the baseline case.

8.3.2 Results of filler particle motion

The filler particles move in the gap, all the SPH particles composing a filler particle move at the same velocity. The motion of the filler particles is driven by the total gas pressure acted on the filler particles from the neighboring SPH particles. We characterize this motion by plotting the position of the center of a filler particle. Figure 49 shows the velocity vectors of filler particles in the baseline case. By choosing the initial position of the filler particle as reference, we compute the relative position of the filler particle. In addition, the relative position is normalized to the dimension of the unit, 0.62mm. Figure 50 shows the normalized relative position of a filler particle with different diameters: 0.062mm and 0.056mm. The filler volume ratio is sit to be 20%. The initial position of the filler particle center is (0.27mm, 0.34mm). It is seen that the translational velocity in the *x*-direction is higher than that in the *y*-direction. This is because of high heat flux along the *x*-direction ($0.1 w/m^2$) than along the *y*-direction ($0.025 w/m^2$), thus, UO_2 –UC conversion is faster in this direction. More gases are produced and filler particles move with higher speed in the *x*-direction. In addition, it is seen that the velocity for the filler particles with smaller radius is higher. This is due to the greater mass of the bigger filler particles.

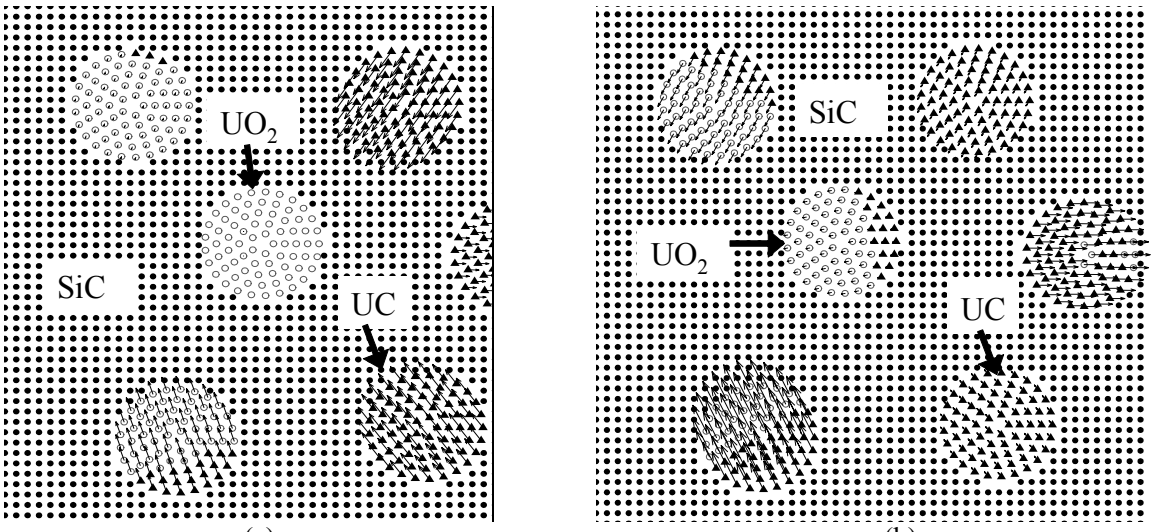

(a) (b)

Figure 49 Velocity vectors of filler particles for the baseline case. The reaction times are (a) 10hours and (b) 11.5hours.

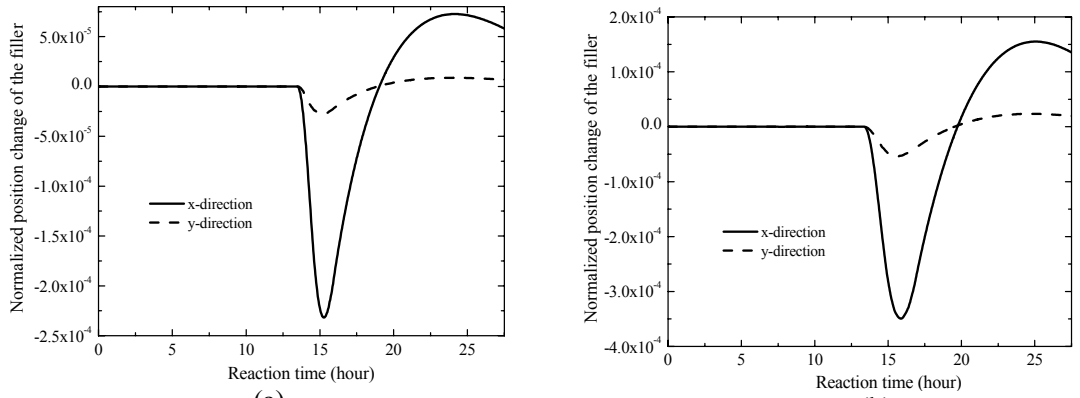

(a) (b)

Figure 50 Normalized relative position of a filler particle. The filler particle diameters are (a) 0.062mm and (b) 0.056mm.

8.3.3 Results of heat flux effect

The effect of heat flux q″ applied to the macro computational domain on the composition evolution is studied. Figure 51 shows the history of the ratio of UO_2 and UC SPH particles for three different heat fluxes: 0.025W/m^2, 0.05W/m^2 (baseline case) and 0.1w/m^2. The filler particle diameter is 0.062mm for all three cases. The filler particles

follow the distribution in the baseline case. It is indicated that the production rate of both UO_2 and UC increases as the heat flux increases.

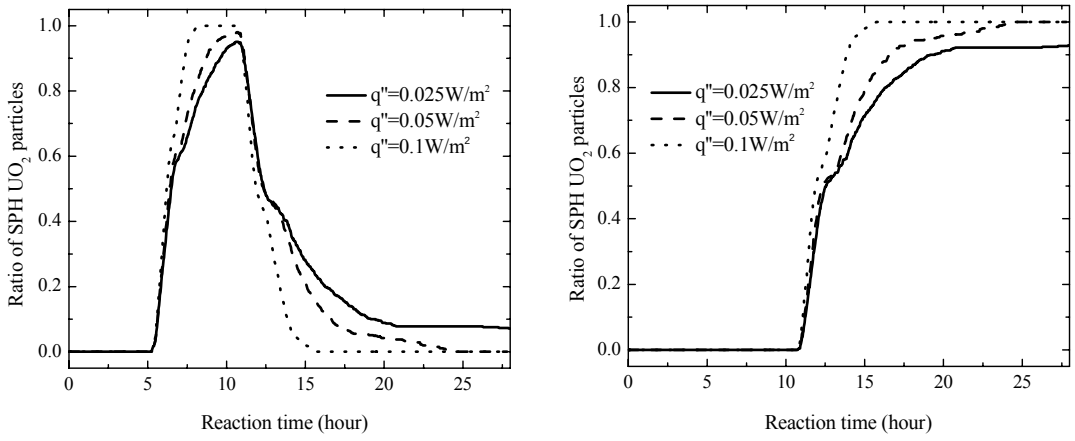

Figure 51 Composition evolution of filler particles with heat fluxes, (a) the ratio of UO_2, (b) the ratio of UC.

8.3.4 Results of filler particle size effect

The effect of filler particle size on the composition evolution is studied. Figure 52 shows the initial distribution of the filler particles with three different diameters: 0.056, 0.062 (baseline case) and 0.069mm. The filler volume ratio is assumed to be 20% for all three cases. Figure 53 shows the history of the ratio of UO_2 and UC SPH particles of three cases. It is indicated that the production rate of UC increases as the filler particle size increases. This might be explained by the heat flux directions. Another possible reason is that total gap area associated with the shrinkage of smaller filler particle size is larger, making the production rate of UC lower.

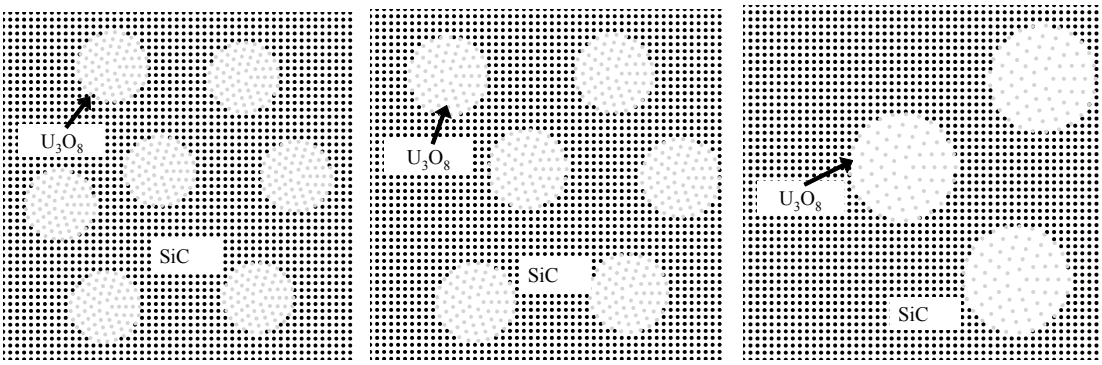

(a) (b) (c)

Figure 52 Initial distribution of filler particles with different diameters: (a) d=0.056mm and (b) d=0.062mm, and (c) d=0.069mm. The black solid circle and gray solid circle represent SiC and U_3O_8, respectively.

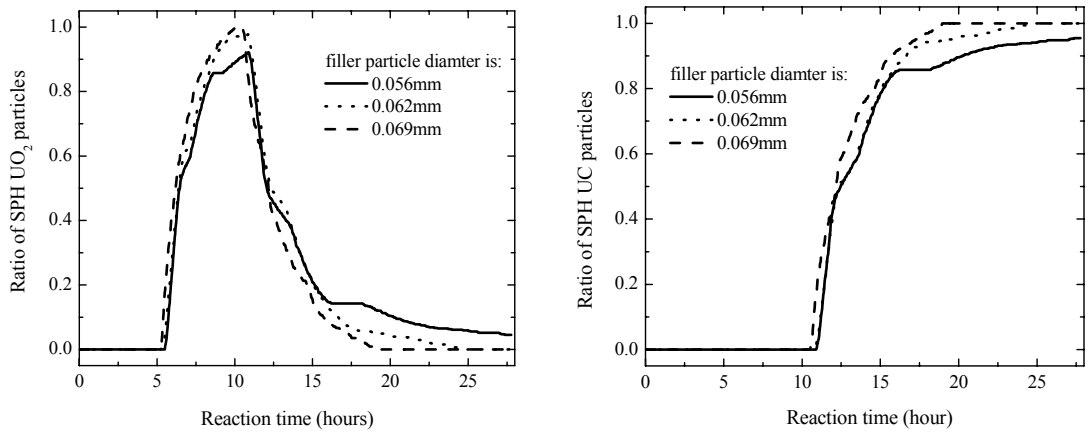

(a) (b)

Figure 53 Composition evolution of filler particles with different sizes: (a) UO_2 and (b) UC.

8.3.5 Results of filler particle volume effect

The effect of filler particle volume on the composition evolution is studied. Figure 54 shows the initial distribution of the filler particles with three different volume ratios: 10%, 15% and 20% (baseline case). The filler particle diameter is 0.062mm for all three cases. Figure 55 shows the history of the ratio of UO_2 and UC SPH particles of three cases. It is indicated that the production rate of both UO_2 and UC increases slightly as the filler particle ratio increases. This might be explained by the heat flux directions. The influence of filler particle volume on the UC production rate is, however, weaker than that of filler particle size when comparing Figure 53(b) and 55 (b). It is interesting to

observe that it takes the same reaction time for all SPH filler particles to convert into UC particles.

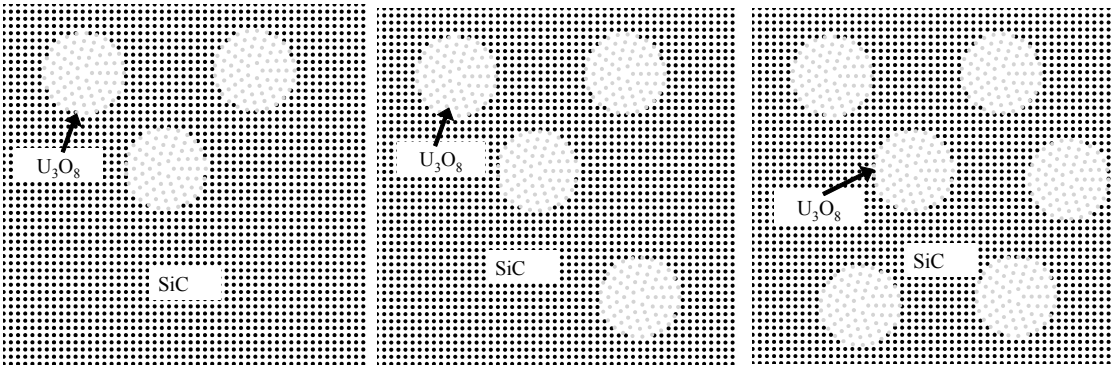

(a) (b) (c)

Figure 54 Initial distribution of filler particles with different volume ratios: (a) f=0.1, (b) f=0.15, and (c) f=0.2. The black solid circle and grey solid circle represent SiC and U_3O_8, respectively.

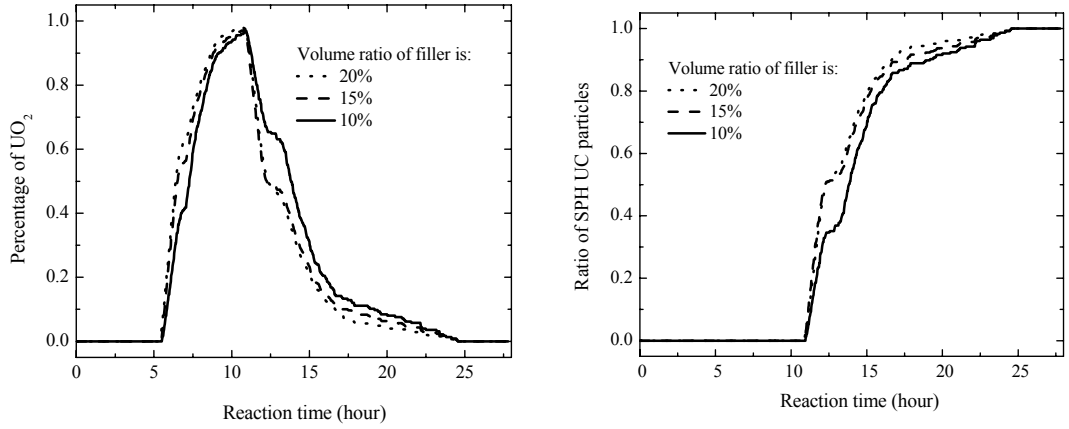

(a) (b)

Figure 55 Composition evolution of filler particles of different volume ratios of filler particles: (a) UO_2, (b) UC.

8.3.6 Uncertainty due to particle distribution

Given at the same particle volume distribution, the material properties will be different if the particle distribution is different. The uncertainty associated with random distribution of filler particles is studied next. It is characterized by comparing the

composition change of filler particles with the same particle size and volume ratio, but different distributions. Five distributions are generated and used to study the uncertainty.

Figure 56 and Figure 57 show the history of the ratio of UO_2 and UC SPH particles of five different random distributions of filler particles. The volume ratio of the filler is 10% and 20% in Figure 56 and Figure 57, respectively. It is indicated that the distribution of the filler particles will influence the reaction and the composition change of filler particles if more significant if the filler volume ratio is 10%. However, this influence becomes quite weak as the volume ratio reaches 20%. The total reaction time for all SPH filler particles to be converted into UC is about same for five distributions when the volume ratio is 20% (Figure 57).

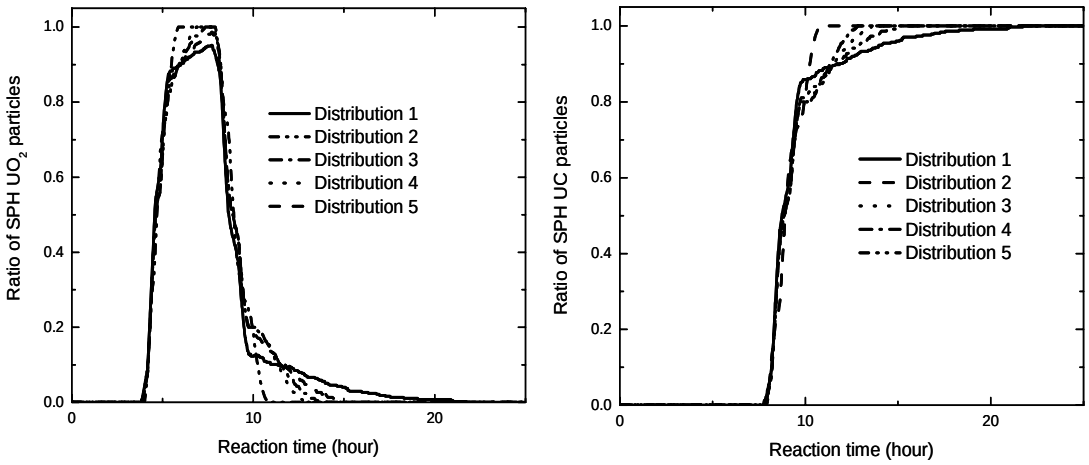

(a) (b)

Figure 56 Composition evolution of filler particles with different distributions, volume ratio of filler particles is 10%: (a) UO_2 and (b) UC.

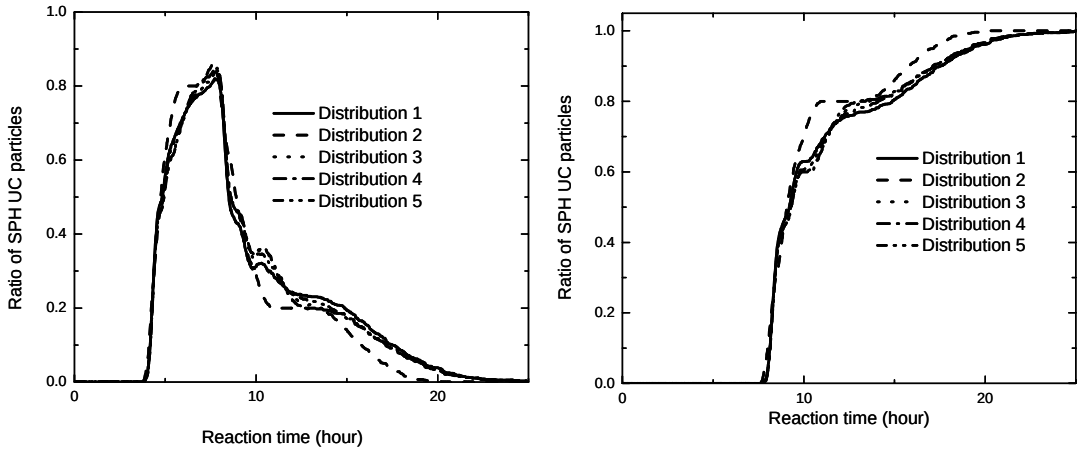

Figure 57 Composition evolution of filler particles with different distributions, volume ratio of filler particles is 20%: (a) UO_2 and (b) UC.

8.4 Conclusions

A mesoscopic model based on the smoothed particle hydrodynamics (SPH) method is developed to describe the synthesis of SiC matrix and uranium oxide particles in a macro-unit. It is the first model, which is capable of considering synthesis of two different components with solid phases and involving generation of volatiles at the particle level. Moreover, it can easily handle the geometry changes and shrinkage phenomena. The current work lays the foundation of the application of SPH technique to the solid-solid reaction, in particular, to the problems involved in the synthesis of two components, mass loss, composition change, uniformity of the product and shrinkage, and bulk motion of filler particles in the SiC matrix.

The effect of the filler particle size and volume on species uniformity and structure are investigated using the particle based mesoscopic model. It is indicated that the production rate of both UO_2 and UC increases as the filler particle size increases. Furthermore, the production rate of both UO_2 and UC increases as the volume ratio of filler particles increases. The motion of filler particles is also investigated. It is indicated that the particles move with a higher speed in the direction with a higher heat flux. In addition, it is concluded that the velocity for the filler particles at a smaller radius is higher. In the future, the mesoscopic model will be integrated with the porous media based global model so that the material processing can be optimized.

Chapter 9

Conclusion and Future Work

9.1 Conclusion of Multiphase Flow with Solidification by Bridgman Crystal Growth

The effects of Prandtl, Grashof, Stefan and Biot numbers on axial temperature profile, interface shape and temperature, and flow fields are investigated. It is found that the influence of melt flow on temperature distribution is strong when the Prandtl number is large. For a material with high Prandtl and Grashof numbers, temperature field and growth interface will be significantly influenced by melt convection, resulting in complicated temperature distribution and curved interface shape.

A system with improved heat zone design has been proposed through reducing the length of primary hot zone for suppressing natural convection. Numerical results show that natural convection is significantly suppressed and temperature perturbation is decreased at the growth interface using the new design. Parametric studies are performed to investigate the effects of geometry size of different zones on crystal growth. Simulation results prove that natural convection is significantly suppressed and temperature perturbation is decreased at the growth interface, when the length of hot zone H_2 is reduced. However the length of transition zone has little effect on melt convection and temperature distribution. Simulation results can provide help to optimize this top portion cooling design.

9.2 Conclusion of Multiphase Flow with Solidification by DSS

In this part, a numerical model is developed to simulate mc-Si ingot growth process by an industrial directional solidification system. The evolution of temperature distribution and interface are presented when constant growth rate is achieved. The energy balance analysis predicts the consumed heater power during solidification process with constant growth rate. It indicates the increase of the consumed heater power mainly due to the increase of radiation heat loss. This agrees with experimental results very well. The effects of thermal conductivity of insulation layer are also studied. It can be concluded that consumed heater power increases because of the increase of heat conduction loss. A key geometry modification of furnace components, where partition part is placed under the heater power, is investigated. It shows that this modification in system geometry can improve energy efficiency as well as crystal quality.

9.3 Conclusion of Multiphase Flow with Chemical Reaction for Synthesis of Uranium-ceramic Nuclear Fuel

A mesoscopic model based on the smoothed particle hydrodynamics (SPH) method is developed to describe the synthesis of SiC matrix and uranium oxide particles in a macro-unit. It is the first model, which is capable of considering synthesis of two different components with solid phases and involving generation of volatiles at the particle level. Moreover, it can easily handle the geometry changes and shrinkage phenomena. The current work lays the foundation of the application of SPH technique to the solid-solid reaction, in particular, to the problems involved in the synthesis of two components, mass loss, composition change, uniformity of the product and shrinkage, and bulk motion of filler particles in the SiC matrix.

The effect of the filler particle size and volume on species uniformity and structure are investigated using the particle based mesoscopic model. It is indicated that the production rate of both UO_2 and UC increases as the filler particle size increases. Furthermore, the production rate of both UO_2 and UC increases as the volume ratio of filler particles increases. The motion of filler particles is also investigated. It is indicated that the particles move with a higher speed in the direction with a higher heat flux. In addition, it is concluded that the velocity for the filler particles at a smaller radius is

higher. In the future, the mesoscopic model will be integrated with the porous media based global model so that the material processing can be optimized.

9.4 Direction of Future Work

As demonstrated in the Introduction part, The objective of this thesis is to utilize the computational approaches to investigate the multiphase flow and its application in the materials processes, especially in the following two areas: directional solidification, and pyrolysis and synthesis.

For the multiphase flow with directional solidification, a system level based on FVM is established. In this model, melt convection, temperature distribution, phase change and solidification interface can be investigated. However, to accurately track the growth interface, meshes adaptation is needed to and it requires iterations at the interfacial boundaries between solid and liquid regions, resulting in huge computational load.

For the multiphase flow with chemical reaction, a particle level model based on SPH method is developed to describe the pyrolysis and synthesis process of uranium-ceramic nuclear fuel. Due to its mesh-free nature, SPH can easily handle the problems with multi phases and components, large deformation, chemical reactions and even solidifications. Consequently, the microstructure evolution of SiC matrix and filler particles, the shrinkage due to density difference, and solid-solid reaction can be studied using SPH scheme. Therefore SPH method shows the great ability to simulate the microstructure evolution and interface morphology between different phases.

When even more complicated phenomena are studied, for example both solidification and chemical reaction are present, an advanced approached may be needed. A multi-scale meso-macroscopic approach might be one of the choices. A mesoscopic model based on SPH method and macroscopic model based on FVM, FEM and FDM can be combined with each other. In the mesoscopic model by SPH method, some fundamental mesoscopic phenomena, such as the microstructure evolution, interface morphology represented by high resolution, particle entrapment in solidification can be studied. In the macroscopic model, the heat transfer, fluid flow, species transport can be

modeled, and the simulation results provided the velocity, temperature and species boundary condition necessary for the mesoscopic model.

Reference

1. M. Cross, T. N. Croft, G. Djambazov, K. Pericleous, *Computational modelling of bubbles, droplets and particles in metals reduction and refining*, Applied Mathematical Modelling, 30 (11) (2006) 1445-1458.
2. C. E. Brennen, *Fundamentals of multiphase flow*, Cambridge University Press, 2005.
3. C. Y. Wang, C. Beckermann, *A multiphase solute diffusion model for dendrite alloy solidification*, Metallurgical Transactions A, 24A (1993) 2787-2802.
4. L. Tan, N. Zabaras, *Multiscale modeling of alloy solidification using a database approach*, Journal of Computational Physics, 227 (1) (2007) 728-754.
5. J. Ni, C. Beckermann, *A Volume-Averaged Two-Phase Model for Solidification Transport Phenomena,*, MEtallurgical Transactions B, 22B (1991) 349-361.
6. C. Y. Wang, C. Beckermann, *Equiaxed Dendritic Solidification with Convection: Part 1. Multi-Scale /-Phase Modeling*, Metallurgical Transactions A, 27A (1996) 2754-2764.
7. N. Provatas, N. Goldenfeld, J. Dantzig, *Adaptive Mesh Refinement Computation of Solidification Microstructures Using Dynamic Data Structures*, Journal of Computational Physics, 148 (1) (1999) 265-290.
8. W. M. Feng, P. Yu, S. Y. Hu, Z. K. Liu, Q. Du, L. Q. Chen, *Spectral implementation of an adaptive moving mesh method for phase-field equations*, Journal of Computational Physics, 220 (1) (2006) 498-510.
9. D. Juric, G. Tryggvason, *A Front-Tracking Method for Dendritic Solidification*, Journal of Computational Physics, 123 (1) (1996) 127-148.
10. N. Al-Rawahi, G. Tryggvason, *Numerical Simulation of Dendritic Solidification with Convection: Two-Dimensional Geometry*, Journal of Computational Physics, 180 (2) (2002) 471-496.
11. N. Al-Rawahi, G. Tryggvason, *Numerical simulation of dendritic solidification with convection: Three-dimensional flow*, Journal of Computational Physics, 194 (2) (2004) 677-696.
12. P. Zhao, J. C. Heinrich, *Front-Tracking Finite Element Method for Dendritic Solidification*, Journal of Computational Physics, 173 (2) (2001) 765-796.
13. A. A. Wheeler, W. J. Boettinger, G. B. McFadden, *Phase-field model for isothermal phase transition in binary alloys*, Physical Review A, 45 (10) (1992) 7424-7439.
14. C. W. Lan, C. C. Liu, C. M. Hsu, *An Adaptive Finite Volume Method for Incompressible Heat Flow Problems in Solidification*, Journal of Computational Physics, 178 (2) (2002) 464-497.
15. Y. T. Kim, N. Goldenfeld, J. Dantzig, *Computation of dendritic microstructures using a level set method*, Physical Review E, 62 (2) (2000) 2471-2474.
16. L. L. Zheng, H. Zhang, *An adaptive level set method for moving boundary problems: applications to droplet spreading and solidification*, Numerical Heat Transfer, Part B, 37 (2000) 437-454.
17. L. Tan, N. Zabaras, *Modeling the growth and interaction of multiple dendrites in solidification using a level set method*, Journal of Computational Physics, 226 (1) (2007) 131-155.

18. L. Tan, N. Zabaras, *A level set simulation of dendritic solidification of multi-component alloys*, Journal of Computational Physics, 221 (1) (2007) 9-40.
19. J. Gnauk, R. Wenke, G. Frommeyer, *Macroscopic modeling of solidification processes by performing the generalized enthalpy method*, Materials Science and Engineering: A, 413-414 (2005) 490-496.
20. S. N. Omeny, A. W. Nuemann, *Thermodynamics aspects of particle engulfment by solidifying melts*, Journal of Applied Physics, 47 (9) (1976) 3956-3962.
21. D. R. Uhlmann, B. Chalmers, K. A. Jackson, *Interaction between particles and a solid-liquid interface*, Journal of Applied Physics, 35 (10) (1964) 2986-2993.
22. J. W. Gao, C. Y. Wang, *Transport Phenomena During Solidification Processing of Functionally Graded Composites by Sedimentation*, Journal of Heat Transfer, Transaciton of ASME, 123 (2001) 368-375.
23. R. J. FELLER, C. BECKERMANN, *Modeling of Solidification of Metal-Matrix Particulate Composites with Convection*, METALLURGICAL AND MATERIALS TRANSACTIONS B, 28B (1997) 1165-1183.
24. S. MUKHERJEE, M. A. R. SHARIF, D. M. STEFANESCU, *Liquid Convection Effects on the Pushing-Engulfment Transition of Insoluble Particles by a Solidifying Interface: Part II. Numerical Calculation of Drag and Lift Forces on a Particle in Parabolic Shear Flow*, METALLURGICAL AND MATERIALS TRANSACTIONS A, 35A (2004) 623-629.
25. J. K. Kim, P. K. Rohatgi, *The effect of the diffusion of solute between the particle and the interface on the particle pushing phenomena* Acta Mater, 46 (4) (1998) 1115-1123.
26. A. W. Rempel, M. G. Worster, *The interaction between a particle and an advancing solidification front*, Journal of Crystal Growth, 205 (3) (1999) 427-440.
27. H. B. Xiong, Y. Ma, L. L. Zheng, *Multiphase flow in directional solidification of metal matrix particulate composites*, Modeling and simulation in materrials and engineering, 14 (2006) 445-463.
28. T. A. M. Haemers, D. G. Rickerby, E. J. Mittemeijer, *Simulation of solidification structures of binary alloys: a multi-particle diffusion-limited aggregation model with surface rearrangement* Modeling and simulation in materrials and engineering, 7 (1999) 233-252.
29. A. DAS, E. J. MITTEMEIJER, *Simulation of Eutectic Solidification Structures of Binary Alloys: a Multiparticle Diffusion Limited Aggregation Model*, Metallurgical & Materials Transactions A, 31A (2000) 2049-2057.
30. M. J. Crochet, F. Dupret, Y. Ryckmans, F. T. Geyling, E. M. Monberg, *Numerical simulation of crystal growth in a vertical bridgman furnace*, Journal of Crystal Growth, 97 (1) (1989) 173-185.
31. F. Dupret, P. Nicodeme, Y. Ryckmans, P. Wouters, M. J. Crochet, *Global modelling of heat transfer in crystal growth furnaces*, International Journal of Heat and Mass Transfer, 33 (9) (1990) 1849-1871.
32. R. Ma, H. Zhang, D. J. Larson, K. C. K. C. Mandal, *Dynamics of melt-crystal interface and thermal stresses in rotational Bridgman crystal growth process*, Journal of Crystal Growth, 266 (1-3) (2004) 216-223.

33. H. Zhang, L. L. Zheng, V. Prasad, D. J. Larson, *Local and global simulations of Bridgman and liquid-encapsulated Czochralski crystal growth*, Journal of Heat Transfer, 120 (1998) 865-873.
34. K. Hashio, M. Tatsumi, H. Kato, K. Kinoshita, *Directional solidification of InxGa1-xAs*, Journal of Crystal Growth, 210 (4) (2000) 471-477.
35. A. Mitric, T. Duffar, V. Corregidor, L. C. Alves, N. P. Barradas, *Growth of GaInSb concentrated alloys under alternating magnetic field*, Journal of Crystal Growth, 310 (7-9) (2008) 1424-1432.
36. C. Stelian, *Numerical modeling of the semiconductor alloys solidification by using a baffle under microgravity and terrestrial conditions*, Journal of Crystal Growth, 310 (7-9) (2008) 1552-1558.
37. Hanjee Lee, A. J. Pearlstein, *Interface shape and thermally-driven convection in vertical Bridgman growth of Gallium Selenide: A semiconductor with aisotropic Solid-phase thermal conductivity*, Journal of Heat Transfer, Transactions of ASME, 123 (2001) 729-740.
38. H. Lee, A. J. Pearlstein, *Simulation of radial dopant segregation in vertical Bridgman growth of GaSe, a semiconductor with anisotropic solid-phase thermal conductivity*, Journal of Crystal Growth, 231 (1-2) (2001) 148-170.
39. N. N. Kolesnikov, E. B. Borisenko, D. N. Borisenko, V. K. Gartman, *Influence of growth conditions on microstructure and properties of GaSe crystals*, Journal of Crystal Growth, 300 (2) (2007) 294-298.
40. L. Lun, A. Yeckel, M. Reed, C. Szeles, P. Daoutidis, J. J. Derby, *On the effects of furnace gradients on interface shape during the growth of cadmium zinc telluride in EDG furnaces*, Journal of Crystal Growth, 290 (1) (2006) 35-43.
41. L. Sylla, T. Duffar, *Numerical simulation of temperature and pressure fields in CdTe growth experiment in the Material Science Laboratory (MSL) onboard the International Space Station in relation to dewetting*, Journal of Crystal Growth, 303 (1) (2007) 187-192.
42. E. Saucedo, P. Rudolph, E. Dieguez, *Modified Bridgman growth of CdTe crystals*, Journal of Crystal Growth, 310 (7-9) (2008) 2067-2071.
43. C.-H. Su, S. L. Lehoczky, B. Raghothamachar, M. Dudley, *Crystal growth and characterization of CdTe grown by vertical gradient freeze*, Materials Science and Engineering: B, 147 (1) (2008) 35-42.
44. Y. Okano, H. Kondo, W. Kishimoto, L. Li, S. Dost, *Experimental and numerical study of the VGF growth of CdTe crystal*, Journal of Crystal Growth, 237-239 (Part 3) (2002) 1716-1719.
45. A. G. Ostrogorsky, *Single-crystal growth by the submerged heater method*, Meas.Sci.Technol, (1) (1990) 463-464.
46. S. Kou, *Transport Phenomena and Materials Processing*, (1996) 561.
47. A. G. Ostrogorsky, G. Muller, *Normal and zone solidification using the submerged heater method*, Journal of Crystal Growth, 137 (1-2) (1994) 64-71.
48. A. Fedyushkin, N. Bourago, V. Polezhaev, E. Zharikov, *The influence of vibration on hydrodynamics and heat-mass transfer during crystal growth*, Journal of Crystal Growth, 275 (1-2) (2005) e1557-e1563.

49. D. Vizman, I. Nicoara, G. Muller, *Effects of temperature asymmetry and tilting in the vertical Bridgman growth of semi-transparent crystals*, Journal of Crystal Growth, 212 (1-2) (2000) 334-339.
50. L. Lun, A. Yeckel, P. Daoutidis, J. J. Derby, *Decreasing lateral segregation in cadmium zinc telluride via ampoule tilting during vertical Bridgman growth*, Journal of Crystal Growth, 291 (2) (2006) 348-357.
51. A. Yeckel, G. Compere, A. Pandy, J. J. Derby, *Three-dimensional imperfections in a model vertical Bridgman growth system for cadmium zinc telluride*, Journal of Crystal Growth, 263 (1-4) (2004) 629-644.
52. Y. C. Liu, B. Roux, C. W. Lan, *Effects of accelerated crucible rotation on segregation and interface morphology for vertical Bridgman crystal growth: Visualization and simulation*, Journal of Crystal Growth, 304 (1) (2007) 236-243.
53. W. C. Yu, Z. B. Chen, W. T. Hsu, B. Roux, T. P. Lyubimova, C. W. Lan, *Effects of angular vibration on the flow, segregation, and interface morphology in vertical Bridgman crystal growth*, International Journal of Heat and Mass Transfer, 50 (1-2) (2007) 58-66.
54. S. Balint, L. Braescu, L. Sylla, S. Epure, T. Duffar, *Dependence of the meniscus shape on the pressure difference in the dewetted Bridgman process*, Journal of Crystal Growth, 310 (7-9) (2008) 1564-1570.
55. A. Mitric, T. Duffar, *Design of vertical Bridgman experiments under alternating magnetic field*, Journal of Crystal Growth, 310 (7-9) (2008) 1511-1517.
56. D. I. Kim, Y. K. Kim, *Characteristics of structural defects in the 240kg silicon ingot grown by directional solidification process*, Solar Energy Materials and Solar Cells, 90 (11) (2006) 1666-1672.
57. J. M. Kim, Y. K. Kim, *Growth and characterization of 240kg multicrystalline silicon ingot grown by directional solidification*, Solar Energy Materials and Solar Cells, 81 (2) (2004) 217-224.
58. K. Arafune, E. Ohishi, H. Sai, Y. Ohshita, M. Yamaguchi, *Directional solidification of polycrystalline silicon ingots by successive relaxation of supercooling method*, Journal of Crystal Growth, 308 (1) (2007) 5-9.
59. R. B. Ganesh, H. Matsuo, T. Kawamura, Y. Kangawa, K. Arafune, Y. Ohshita, M. Yamaguchi, K. Kakimoto, *Estimation of growth rate in unidirectionally solidified multicrystalline silicon by the growth-induced striation method*, Journal of Crystal Growth, 310 (11) (2008) 2697-2701.
60. B. Wu, N. Stoddard, R. Ma, R. Clark, *Bulk multicrystalline silicon growth for photovoltaic (PV) application*, Journal of Crystal Growth, 310 (7-9) (2008) 2178-2184.
61. V. Chandrasekaran, C. L. Wang, G. J. Hildeman, *Minicaster - a research-scale directional solidification furnace*, in *17th NREL Workshop on Crystalline Silicon Solar Cells, & Modules: Materials and Processes*. 2006: Vail, CO.
62. Y. Delannoy, F. Barvinschi, T. Duffar, *3D dynamic mesh numerical model for multi-crystalline silicon furnaces*, Journal of Crystal Growth, 303 (1) (2007) 170-174.
63. L. Liu, S. Nakano, K. Kakimoto, *Carbon concentration and particle precipitation during directional solidification of multicrystalline silicon for solar cells*, Journal of Crystal Growth, 310 (7-9) (2008) 2192-2197.

64. Z. Xi, J. Tang, H. Deng, D. Yang, D. Que, *A model for distribution of oxygen in multicrystalline silicon ingot grown by directional solidification*, Solar Energy Materials and Solar Cells, 91 (18) (2007) 1688-1691.
65. H. Matsuo, R. B. Ganesh, S. Nakano, L. Liu, K. Arafune, Y. Ohshita, M. Yamaguchi, K. Kakimoto, *Analysis of oxygen incorporation in unidirectionally solidified multicrystalline silicon for solar cells*, Journal of Crystal Growth, 310 (7-9) (2008) 2204-2208.
66. C. E. Chang, W. R. Wilcox, *Control of interface shape in the vertical bridgman-stockbarger technique*, Journal of Crystal Growth, 21 (1) (1974) 135-140.
67. Y. C. Liu, B. Roux, C. W. Lan, *Effects of cycle patterns of accelerated crucible rotation technique (ACRT) on the flows, interface, and segregation in vertical Bridgman crystal growth*, International Journal of Heat and Mass Transfer, 50 (25-26) (2007) 5031-5040.
68. H. Miyazawa, L. J. Liu, K. Kakimoto, *Numerical analysis of influence of crucible shape on interface shape in a unidirectional solidification process*, Journal of Crystal Growth, 310 (6) (2008) 1142-1147.
69. A. K. Singh, S. C. Zunjarrao, R. P. Singh, *Processing of uranium oxide and silicon carbide based fuel using polymer infiltration and pyrolysis*, Journal of Nuclear Materials, 378 (3) (2008) 238-243.
70. E. Richter, Gramlich, S., Klein, A., Nebauer, E., Rechenberg, I., Zeimer, U., Weyers, M. , *Direct growth of GaN on (0001) sapphire by low pressure hydride vapour phase epitaxy*, Phys. Status Solidi A, 188 (2001) 439-442.
71. P. Greil, *Polymer derived engineering ceramics*, Advanced Engineering Materials, 6 (2) (2000) 339-348.
72. T. Hinoki, Kohyama, A., *Current status of SiC/SiC composites for nuclear applications*, Annales de Chimie: Science des Materiaux, 30 (6) (2005) 659-671.
73. M. Z. Berbon, D. R. Dietrich, D. B. Marshall, D. Hasselman, *Transverse thermal conductivity of thin C/SiC composites fabricated by slurry infiltration and pyrolysis*, Journal of the American Ceramic Society, 84 (10) (2001) 2229–2234.
74. Z. Alkan, K. Kugeler, R. Kaulbarsch, C. Manter, *Silicon Carbide Encapsulated Fuel Pellets for Light Water Reactors*, Progress in Nuclear Energy, 38 (3-4) (2001) 411 – 414.
75. M. Kotani, T. Inoue, A. Kohyama, Y. Katoh, K. Okamura, *Effect of SiC particle dispersion on microstructure and mechanical properties of polymer-derived SiC/SiC composite*, Materials Science and Engineering A, 357 (1-2) (2003) 376-385.
76. Y. W. Lee, S. C. Lee, H. S. Kim, C. Y. Joung, C. Degueldre, *Study on the mechanical properties and thermal conductivity of silicon carbide-, zirconia- and magnesia aluminate-based simulated inert matrix nuclear fuel materials after cyclic thermal shock*, Journal of Nuclear Materials, 319 (2003) 15-23.
77. B. Xiao, Y. Zhang, *Analysis of melting of alloy powder bed with constant heat flux*, Int. J. Heat Mass Transfer, 50 (11-12) (2007) 2161-2169.
78. Q. He, F. Winter, J. D. Lu, *Analysis of the heat transfer mechanism in high-temperature circulating fluidized beds by a numerical model*, J. Heat Transfer, 124 (2002) 34-39.

79. A. Jagota, P. R. Dawson, *Micromechanical modeling of powder compacts-I: unit problems for sintering and traction induced deformation*, Acta Metall., 36 (1988) 2551-2561.
80. J. I. Martinez-Herrera, J. J. Derby, *Analysis of capillary-driven viscous flows during the sintering of ceramic powders*, J. AIChE, 40 (1994) 1794-1803.
81. W. M. Gao, L. X. Kong, P. D. Hodgson, *Computational simulation of gas flow and heat transfer near an immersed object in fluidized beds*, Advances in Engineering Software, 38 (11-12) (2007) 826-834.
82. L. B. Lucy, *A numerical approach to the testing of the fission hypothesis*, Astronomy Journal, 83 (1997) 1013.
83. R. A. Gingold, J. J. Monaghan, *Smoothed particle hydrodynamics: Theory and application to non-spherical stars*, Monthly Notices of the Royal Astronomical Society, 181 (1977) 375.
84. J. J. Monaghan, A. Kocharyan, *SPH simulation of multi-phase flow*, Computer Physics Communications, 87 (1-2) (1995) 225-235.
85. J. J. Monaghan, *Implicit SPH Drag and Dusty Gas Dynamics*, Journal of Computational Physics, 138 (2) (1997) 801-820.
86. A. Colagrossi, M. Landrini, *Numerical simulation of interfacial flows by smoothed particle hydrodynamics*, Journal of Computational Physics, 191 (2) (2003) 448-475.
87. X. Y. Hu, N. A. Adams, *A multi-phase SPH method for macroscopic and mesoscopic flows*, Journal of Computational Physics, 213 (2) (2006) 844-861.
88. X. Y. Hu, N. A. Adams, *An incompressible multi-phase SPH method*, Journal of Computational Physics, 227 (1) (2007) 264-278.
89. Y. Zhu, P. J. Fox, *Simulation of Pore-Scale Dispersion in Periodic Porous Media Using Smoothed Particle Hydrodynamics*, Journal of Computational Physics, 182 (2) (2002) 622-645.
90. J. P. Morris, Y. Zhu, P. J. Fox, *Parallel simulations of pore-scale flow through porous media*, Computers and Geotechnics, 25 (4) (1999) 227-246.
91. F. Jiang, M. S. A. Oliveira, A. C. M. Sousa, *Mesoscale SPH modeling of fluid flow in isotropic porous media*, Computer Physics Communications, 176 (7) (2007) 471-480.
92. A. M. Tartakovsky, P. Meakin, *Pore scale modeling of immiscible and miscible fluid flows using smoothed particle hydrodynamics*, Advances in Water Resources, 29 (10) (2006) 1464-1478.
93. R. Rook, S. Dost, *The use of smoothed particle hydrodynamics for simulating crystal growth from solution*, International Journal of Engineering Science, 45 (1) (2007) 75-93.
94. A. M. Tartakovsky, P. Meakin, T. D. Scheibe, R. M. Eichler West, *Simulations of reactive transport and precipitation with smoothed particle hydrodynamics*, Journal of Computational Physics, 222 (2) (2007) 654-672.
95. L. L. Zheng, H. Zhang, M. Y. Zhang, P. Kerkar, D. Mahajan, *Modeling methane hydrate formation in marine sediments*, American Association of Petroleum Geologists Bulletin, (2005) 1-16.

96. D. Zhang, N. G. Deen, J. A. M. Kuipers, *Numerical simulation of the dynamic flow behavior in a bubble column: A study of closures for turbulence and interface forces*, Chemical Engineering Science, 61 (23) (2006) 7593-7608.
97. N. A. Patankar, D. D. Joseph, *Modeling and numerical simulation of particulate flows by the Eulerian-Lagrangian approach*, International Journal of Multiphase Flow, 27 (10) (2001) 1659-1684.
98. C. G. Ilea, P. Kosinski, A. C. Hoffmann, *Simulation of a dust lifting process with rough walls*, Chemical Engineering Science, In Press, Corrected Proof.
99. C. G. Ilea, P. Kosinski, A. C. Hoffmann, *Three-dimensional simulation of a dust lifting process with varying parameters*, International Journal of Multiphase Flow, In Press, Corrected Proof.
100. C. Y. Wen, Y. H. Yu, *Mechanics of fluidization*, Chemical Engineering Progess Symposium Series, 62 (1966) 100-111.
101. W. Kurz, D. J. Fisher, *Fundamentals of Solidification*, Published by Trans Tech Publications, 1992.
102. M. Yuan, *Generic Numerical Modeling for Semiconductor and Optical Crystal Growth with and without Faceting in Vertical Bridgman System*, in *Mechanical Engineering Department*. 2005, State University of New York at Stony Brook: Stony Brook.
103. V. G. Smith, W. A. Tiller, J. W. Rutter, *A mathematical analysis of solute redistribution during solidification*, Canadian Journal of Physics, 33 (12) (1955) 723-745.
104. W. A. Tiller, K. A. Jackson, J. W. Rutter, G. Chalmers, *The redistribution of solute atoms during the solidification of metals*, Acta Metallurgica, 1 (4) (1953) 428-437.
105. X. L. Wang, *Modeling & Processing of Ceramic and Polymer Precursor Ceramic Matrix Composite Materials*, in *Mechanical Engineering Department*. 2007, State University of New York at Stony Brook: Stony Brook.
106. H. Zhang, M. K. Moellemi, *A multizone adaptive grid-generation technique for simulation of moving and free-boundary problems* Numer. Heat Transfer B, 27 (1995) 255-276.
107. H. Zhang, M. K. Moallemi, V. Prasad, *A Numerical Algorithm Using Multizone Grid Generation for Multiphase Transport Processes with Moving and free Boundaries*, Numerical Heat Transfer B, 29 (1996) 399-421.
108. H. Zhang, in *Mechanical Engineering Department*. 1993, Polytechnic University: Brooklyn.
109. J. U. Brackbill, J. S. Saltzman, *Adaptive zoning for singular problems in 2 dimensions*, Journal of Computational Physics, 46 (1982) 342-368.
110. S. Brandon, J. J. Derby, *Heat transfer in vertical Bridgman growth of oxides: Effects of conduction, convection, and internal radiation*, Journal of Crystal Growth, 121 (1992) 473-494.
111. C. W. Lan, C. Y. Tu, Y. F. Lee, *, Effects of internal radiation on heat flow and facet formation in Bridgman growth of YAG crystals*, International Journal of Heat and Mass Transfer, 46 (2003) 1629-1640.
112. L. L. Zheng, H. Zhang, D. J. Larson, V. Prasad, *, A model for solidification under the influence of thermoelectric and magnetohydrodynamic effects: Application to*

Peltier demarcation during direcrtional solidification with different gravitational conditions, Journal of Heat Transfer, 120 (1998) 430-440.
113. G. R. Liu, Liu, M. B., *Smoothed particle hydrodynamics, A meshfree particle method*, World Scientific Publishing Co. Pte. Ltd., 2003.
114. L. D. Libersky, A. G. Petschek, T. C. Carney, J. R. Hipp, F. A. Allahdadi, *High strain Lagrangian hydrodynamics*, Journal of Computational Physics, 109 (1993) 67-55.
115. P. W. Randles, L. D. Libersky, *Smoothed Particle Hydrodynamics: Some recent improvements and applications*, Computer Methods in Applied Mechanics and Engineering, 139 (1-4) (1996) 375-408.
116. J. Campbell, R. Vignjevic, L. Libersky, *A contact algorithm for smoothed particle hydrodynamics*, Computer Methods in Applied Mechanics and Engineering, 184 (1) (2000) 49-65.
117. J. P. Morris, P. J. Fox, Y. Zhu, *Modeling Low Reynolds Number Incompressible Flows Using SPH*, Journal of Computational Physics, 136 (1) (1997) 214-226.
118. Y. Ma, L. L. Zheng, D. J. Larson, *Microstructure formation during BiMn/Bi eutectic growth with applied alternating electric fields*, J. Cryst Growth, 262 (1-4) (2004) 620-630.
119. H. Zhang, L. L. Zheng, D. J. Larson, V. Prasas, *Local and Global Simulations of Bridgman and Czochralski Crystal Growth*, J. Heat Transfer, 120 (1998) 865-873.
120. H. Zhang, D. J. Larson, C. L. Wang, T. H. Chen, *Kinetics and heat transfer of CdZnTe Bridgman growth without wall contact*, J. Cryst Growth, 250 (1-2) (2003) 215-222.
121. R. Ma, H. Zhang, D. J. Larson, K. C. K. C. Mandal, *Dynamics of melt-crystal interface and thermal stresses in rotational Bridgman crystal growth process*, J. Cryst Growth, 266 (1-3) (2004) 216-223.
122. Y. Ma, L. L. Zheng, D. J. Larson, *Transient simulation of facet growth during directional solidification*, J. Cryst Growth, 266 (1-3) (2004) 257-263.
123. K. C. Mandal, S.H. Kang, M. Choi, J. Bello, J. Wei, L. Zheng, H. Zhang, G.E. Jellison, M. Groza, A. Burger, *Component Overpressure Growth and Characterization of High Resistivity CdTe Crystals for Radiation Detectors*, J. Electron. Mater., in press (2007).
124. H. Lee, A. J. Pearlstein, *Interface shape and thermally-driven convection in vertical Bridgman growth of Gallium Selenide: A semiconductor with aisotropic Solid-phase thermal conductivity*, J. Heat Transfer, Transactions of ASME, 123 (2001) 729-740.
125. V. M. Glozov, S. N. Chizhevskaya, *Liquid Semiconductors*, Plenum Press, New York, 1969.
126. W. J. HoweLL, M. M. Alger, C. A. Eckert, *Application of the Lcpt Model to Solid-Liquid Equilibria for Binary Compound-Forming Alloys*, Aiche Journal, 39 (9) (1993) 1519-1526.
127. T. Maekawa, Y. Sugiki, S. Matsumoto, S. Adachi, S. Yoda, K. Kinoshita, *Numerical analysis of crystal growth of an InAs-GaAs binary semiconductor by the Travelling Liquidus-Zone method under microgravity conditions*, International Journal of Heat and Mass Transfer, 47 (21) (2004) 4535-4546.

128. N. Shin, H. Taketoshi, *Thermal conductivity of GaSb and InSb in solid and liquid states*, J. Applies Physics, 68 (10) (1990) 5125-5127.
129. R. Bowers, R. W. Ure, J. E. Bauerle, A. J. Cornish, *InAs and InSb as Thermoeletirc Materials*, J. Applies Physics, 30 (6) (1959) 930-934.
130. O. Madulung, *Semiconductors Group IV Elements and III-V Compounds*, Springer-Verlag, Berlin, 1991.
131. C. Marin, A. G. Ostrogorsky, *Bulk growth of quasi-binary quaternary alloys*, J. Crystal Growth, 211 (1-4) (2000) 194-201.
132. E. I. Rogacheva, N. I. Sinelik, I. M. Krivulkin, *Semiconductor Physics, Quantum Electronics and Optoelectronics*, 5 (2002).
133. E. I. Rogacheva, I. M. Krivulkin, Proc. SPIE, 277 (1997) 3182.
134. J. J. Monaghan, H. E. Huppert, M. G. Worster, *Solidification using smoothed particle hydrodynamics*, Journal of Computational Physics, 206 (2) (2005) 684-705.
135. G. R. Liu, M. B. Liu, *Smoothed particle hydrodynamics, A meshfree particle method*, World Scientific Publishing Co. Pte. Ltd., 2003.